3B2v7.51c GML4.3.1 | CSI 08125 | Prod.Type: pp.1–63(col.fig.:NIL) | ED:Mahashankar PAGN: MK SCAN:

Published as

Z. Suo, Reliability of Interconnect Structures, pp. 265-324 in Volume 8: Interfacial and Nanoscale Failure (W. Gerberich, W. Yang, Editors), Comprehensive Structural Integrity (I. Milne, R.O. Ritchie, B. Karihaloo, Editors-in-Chief), Elsevier, Amsterdam, 2003.

8.7

SX0005

Reliability of Interconnect Structures

Z. SUO

Mechanical and Aerospace Engineering Department and Princeton Materials Institute, Princeton University, NJ, USA

8.7.1 INTRODUCTION

SX0010 On January 23, 1959, Robert Noyce wrote in his lab notebook: "…it would be desirable to make multiple devices on a single piece of silicon, in order to be able to make interconnections between devices as part of the manufacturing process, and thus reduce size, weight, etc. as well as cost per active device." With these words, the co-inventor (with Jack Kilby) of the integrated circuit, and the co-founder (with Gordon Moore) of Intel Corporation a decade later, spelled out the Monolithic Idea that would shape the microelectronic revolution (bib99 Reid, 1984). To function, transistors, capacitors, and resistors must connect among themselves and to the external world. Rather than first making these components individually and then connecting them with wires, the microelectronic technology fabricates the interconnect structure, as well as all the components, into a single solid piece, the *chip*.

SX0015 Ever since, the technology has advanced by miniaturization, squeezing more and more transistors on every single chip. By necessity the interconnect structure has *complex architectures, diverse materials*, and *small feature sizes*. Figure 1 shows a transmission electron microscope image of an interconnect structure. The structure is a three-dimensional network of conductor lines embedded in a dielectric matrix, fabricated on the silicon surface that contains the active devices. The conductor lines are on several levels, and linked by vias. The lines have rectangular cross-sections and, on a given level, have a constant thickness but variable widths. A silicon nitride film caps the interconnect structure, serving as a barrier of the environmental molecules. Lithographically defined feature sizes, such as linewidth and via size, are as small as 100 nm. Films as thin as a few nanometers are used.

SX0020 Traditional interconnect structures use aluminum as the conductor, and silica as the dielectric. Tungsten vias link the lines between the levels, and titanium nitride thin layers lie between the aluminum lines and the dielectric. To make faster devices, the conductor must have higher conductivity, and the dielectric must have lower dielectric constant. Copper has been used as the conductor lines in more recent interconnect structures (bib104 Rosenberg *et al.*, 2000). The conductor lines at different levels are linked with copper vias. Liners such as tantalum lie between the conductor and the dielectric to prevent copper diffusion into the dielectric and to promote adhesion. Low-dielectric-constant materials of current use include an organic material known as SiLK (bib88 Martin *et al.*, 2000), and a carbon doped oxide. The former is ductile, and

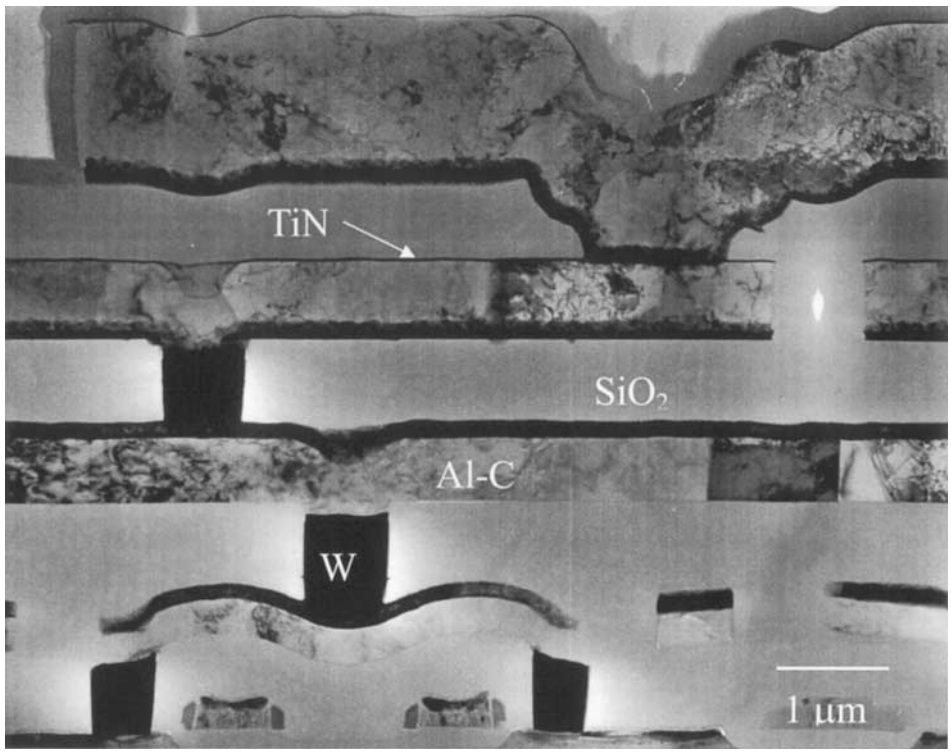

Figure 1 A transmission electron microscope image of a cross-section of an interconnect structure (courtesy of John Mardinly, Intel Corporation).

the latter is brittle. Both are compliant compared to silicon dioxide. To further reduce the dielectric constant, other materials, including porous materials, will be used in future interconnects (bib93 Morgen *et al.*, 1999).

SX0025 The Monolithic Idea solves one problem, but creates another. Making reliable interconnect structures has been a persistent challenge. Stress results from material deposition, thermal expansion mismatch, and electromigration. Material deposition inevitably generates stress; e.g., deposition of refractory metals such as tungsten usually generates stress in the GPa range. Materials in interconnect structures, selected to function as conductors, dielectrics, or barriers, have dissimilar thermal expansion coefficients. On cooling from the fabrication temperature, the structures acquire stresses. To fit into the small space, each conductor line must have a small cross-sectional area. The intense electric current motivates metal atoms to diffuse in the line, generating tension where atoms deplete, and compression where atoms accumulate.

SX0030 The study of interconnect reliability has a long history. Electromigration has been a persistent concern ever since integrated circuits were mass-produced (bib16 Blech and Meieran, 1967). As atoms diffuse, voids grow and sever metal lines. Stress-induced voiding was observed in the 1980s, when the technology brought the linewidth comparable to the line thickness (bib24 Curry *et al.*, 1984). Such an aluminum line, of approximately square cross-section, encapsulated in silica, develops triaxial stresses of magnitude much above the yield strength of aluminum (bib64 Jones and Basehore, 1987). Voids grow to relax the stresses, facilitated by atomic diffusion (bib106 Sauter and Nix, 1992; bib69 Korhonen *et al.*, 1993). Around the same time, thin film fracture mechanics was advanced (bib30 Evans *et al.*, 1988; bib61 Hutchinson and Suo, 1991; bib124 Thouless, 1991), providing tools to quantify toughness of thin films (bib85 Ma *et al.*, 1998; bib23 Cook and Liniger, 1999), and adhesion between thin films (bib25 Dauskardt *et al.*, 1998; bib132 Volinsky *et al.*, 2002). The tools have been incorporated into industrial practice in material selection, process control, and failure analysis.

SX0035 More recently, a new failure mechanism has been identified, in which cracks grow in brittle films under cyclic temperatures, aided by ratcheting deformation in a metal underlayer (bib57 Huang *et al.*, 2000). Stress-induced voiding has been observed in blanket copper films (bib109 Shaw *et al.*, 2001; bib107 Sekiguchi *et al.*, 2001), and in copper vias in the copper/silica interconnect structure (bib47 Hommel *et al.*, 2001; bib96 Ogawa *et al.*, 2002). Low dielectric constant materials have low stiffness; their effects on interconnect reliability are the focus of current studies (bib75 Lee *et al.*, 2002; bib4 Ambrico *et al.*, 2002; bib78 bib79 Liang *et al.*, 2002a, 2002b; bib102 Rim *et al.*, 2002).

SX0040 This chapter is organized according to failure modes: cracking, debonding, ratcheting, voiding, and electromigration. Such perversities are not only nuisances—problems to be tested away by trial-and-error, but also opportunities for fundamental study of the mechanical behavior of diverse materials, in integrated structures, at an unprecedented small size scale. The study of electromigration has led to the discovery that adding a few percent of copper into aluminum interconnects slows aluminum diffusion rate by nearly two orders of magnitude. As of early 2000s, the atomistic origin of this behavior is still not fully understood. The observation of stress-induced voiding, perhaps more than any other single event, has motivated academic researchers to join their industrial colleagues to study atomistic processes of stress generation and relaxation in thin films. The introduction of copper and low-dielectric-constant materials has given a new urgency to study cracking and debonding in small structures. The fundamental study will impact other major technologies, such as MEMS, integrated photonics, and thermal barrier coatings, where small-structure mechanical behavior is important. bib131 Vinci and Baker (2002) have edited a multi-author review on mechanical properties in small dimensions.

SX0045 The present (our context is early 2000s) method to design reliable small structures, if there is one, rests on continuum mechanics, manifest in handbook solutions, commercial finite element codes, and related measurement protocols. Their inadequacy is increasingly evident when the structures become small, because (among other issues) plastic flows become discrete, and failure phenomena become nucleation, rather than growth, controlled. In the rapidly changing economics of tools for the small, the division of labor has yet been settled: what to understand, what to compute, and what to measure. The tension between the relentless trend of miniaturization and the disquieting lack of a method to design for reliability will inspire innovations for years to come.

8.7.2 CRACKING

SX0050 Figure 2 illustrates cracks in a brittle thin film bonded on a silicon substrate. The film is under a state of biaxial tensile stress. Starting from a flaw in the film, a crack runs across the film thickness and often arrests at the interface, leaving the interface and the substrate intact. The crack, however, elongates laterally in the film, uninhibited until it meets a film edge or another crack. The lateral crack length can be many times the film thickness. Such a crack is known as a channel crack. Because the film may have many pre-existing flaws, under a large stress, many channel cracks can form. A cracked film looks like a field of drying mud.

SX0055 A brittle material fractures by breaking atomic bonds along the front of a crack. The atomistic bond-breaking process remains unchanged when this brittle material is integrated in a structure, surrounded by other materials, so long as the feature size is large compared to individual atoms. It is, however, the close proximity of the dissimilar materials that gives rise to the diverse fracture behaviors observed in the interconnect structure. The integration of dissimilar materials introduces stresses. During fracture, even when the crack is confined in the brittle material, the surrounding materials deform, sometimes inelastcially.

SX0060 The pragmatic approach to fracture in the interconnect structure pays little attention to the atomistic bond-breaking process itself, but instead focuses on deformation in the surrounding materials. The division of labor is brilliantly made within the framework of linear elastic fracture mechanics:

(a) The fracture toughness is a property specific to the given brittle material, unaffected by the surrounding materials, and is measured experimentally.

(b) The crack driving force depends on the surrounding materials, and is related to their deformation by calculation.

SX0061 We begin with an outline of the linear elastic fracture mechanics, and its use in the interconnect structure. Energy consideration is taken up next. We then describe a channel crack in a thin film bonded to an elastic substrate. This simple structure leads to a method to measure the fracture toughness. To illustrate the effects of deformation, we examine a channel crack in a brittle film on an inelastic underlayer. The crack velocity is set by creep in the underlayer, as well as by subcritical cracking in the brittle film.

8.7.2.1 Linear Elastic Fracture Mechanics

SX0065 bib74 Lawn (1993) is an established textbook on brittle fracture. Here we outline the fundamentals of immediate importance to the interconnect structure. Figure 3 illustrates a crack in a body subject to a distribution of load that opens the crack. Model the body by a linear elastic solid, the crack faces by two matching surfaces, and the crack front by a curve. Within the theory of linear elasticity, a boundary value problem determines the stress field in the body. Of course, the stress field depends on the boundary conditions: the size and the shape of the crack and the body, as

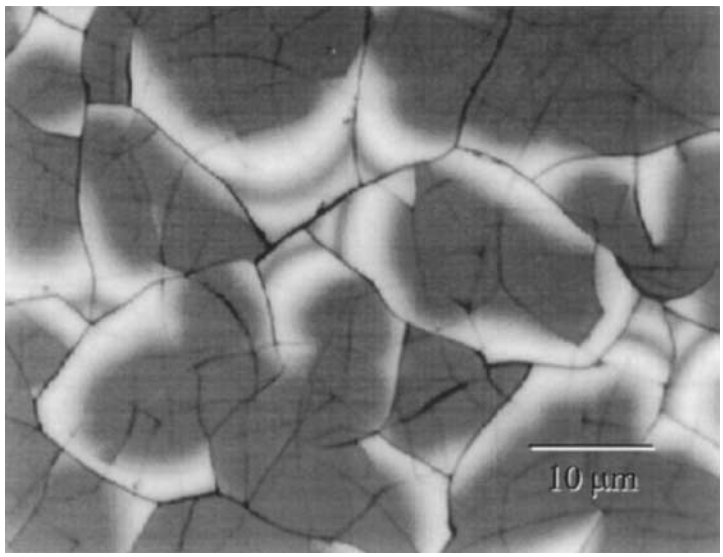

Figure 2 A plan view of a silicon nitride film of $\sim 1\,\mu m$ thickness grown on a silicon substrate. The tensile stress in the film causes channel cracks. The contrast indicates that the film also partially debonds from the substrate (courtesy of Q. Ma, Intel Corporation).

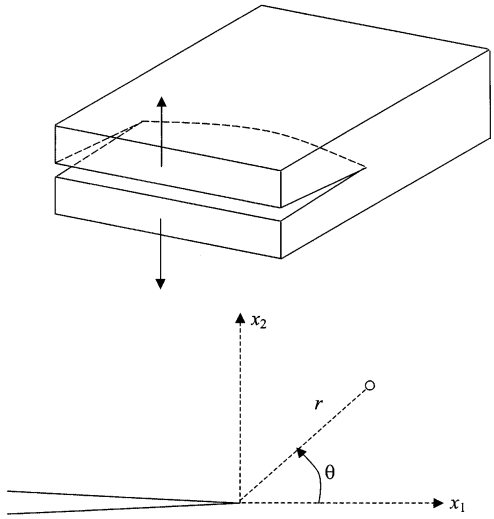

Figure 3 A crack in a body subject to a distribution of load that opens the crack. Also shown is the coordinate system in a plane normal to the crack front.

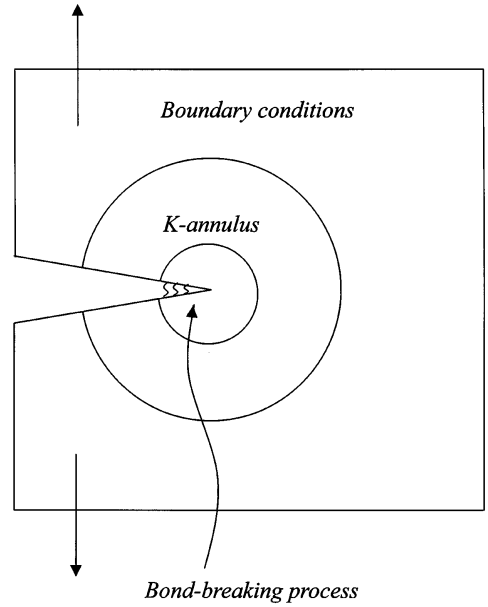

Figure 4 The singular stress field is valid in the *K*-annulus. Inside the inner circle, the atomistic bond-breaking process invalidates the linear elasticity theory. Outside the outer circle, the boundary conditions invalidate the singular stress field.

well as the magnitude and the distribution of the load. By modeling the crack front as a mathematical curve, the linear elasticity theory does not account for the atomistic bond-breaking process.

SX0070 One feature of the stress field, common to all such elasticity boundary value problems, plays a special role in the fracture mechanics. Let (r, θ) be the polar coordinates, centered at a particular point along the crack front, in the plane normal to the crack front. The (x_1, x_2) coordinates are in the same plane. The linear elasticity theory shows that the stress field in the body takes the form

$$\sigma_{ij}(r,\theta) = \frac{K}{\sqrt{2\pi r}}\,\Sigma_{ij}(\theta). \qquad (1)$$

The dependence on r is square-root singular. The stress field scales with K, known as the stress intensity factor. The factor 2π is introduced by convention. The θ-dependent functions, $\Sigma_{ij}(\theta)$, are listed in bib74 Lawn (1993); for example,

$$\Sigma_{22}(\theta) = \cos(\theta/2)[1 + \sin(\theta/2)\sin(3\theta/2)]. \quad (2)$$

The opening stress a distance r directly ahead of the crack front is

$$\sigma_{22}(r,0) = \frac{K}{\sqrt{2\pi r}}. \qquad (3)$$

For a crack in three dimensions, the stress intensity factor K may vary along the front of the crack.

SX0075 The r- and θ-dependence of the singular stress field are independent of the boundary conditions. The boundary conditions, however, do determine the magnitude of the stress intensity factor K. For example, a crack of length $2a$, in an infinite elastic sheet, subject to a tensile stress σ remote from the crack, has the stress intensity factor $K = \sigma\sqrt{\pi a}$. Solutions of the stress intensity factors for many crack configurations are collected in handbooks (e.g., bib122 Tada *et al.*, 1985). Commercial finite element codes are routinely used to calculate K for complex crack configurations. Dimensional considerations dictate that the stress intensity factor should take the form

$$K = \kappa\sigma\sqrt{L}, \qquad (4)$$

where L is a representative length, σ a representative stress, and κ a dimensionless number. The number κ is determined by solving the boundary value problem. It depends on the ratio of the crack length to L, as well as other ratios that characterize the integrated structure. Examples will be given later.

SX0080 As mentioned above, the theory of elasticity predicts that the stress field is square-root singular. Of course, we do not believe that the stress is infinite at the crack front. The physical significance of the singular stress field is understood as follows (Figure 4). Imagine the plane normal to the crack front. The stress field (1) is valid in an annulus, with the inner radius larger than the zone in which the bond-break-

ing process invalidates the linear elasticity theory, and the outer radius smaller than the size of the body and the crack. We call this annulus the *K*-annulus. Neither the bond-breaking processes inside the inner circle, nor the boundary conditions outside the outer circle affect the r- and θ-dependence of the stress field in the *K*-annulus: the stress field (1) is valid in this annulus. For a brittle solid, the bond-breaking processes invalidate the linear elasticity theory within a zone about 1 nm. A representative feature size in interconnect structures is 100 nm. These lengths roughly set the size of the *K*-annulus.

SX0085 So far the model does not account for the atomistic bond-breaking process. Imagine two samples of the same solid, each containing a crack under an opening load. The two samples may have different sizes and shapes. The loads on the two samples may also be different. Regardless of such differences, because the stress field in the *K*-annulus depends on the boundary conditions through the stress intensity factor, the bond-breaking processes in the two samples must be identical if K is the same for the two samples. That is, K is the only messenger between the external boundary conditions and the bond-breaking process.

SX0090 The central idea of the linear elastic fracture mechanics has been so summarized: *the same K, the same crack-tip process.* Within the fracture mechanics, the simplest way to account for the bond-breaking process is to stipulate that the crack extends when the stress intensity factor K in a body containing a crack reaches a critical value, K_c, known as the fracture toughness.

SX0091 Once the stress intensity factor is calculated for a given crack configuration, in the form of (4), the condition for the crack to grow is

$$\kappa\sigma\sqrt{L} = K_c. \tag{5}$$

SX0092 For a given material, the fracture toughness is determined experimentally. Start with a specimen of the material, introduce a crack into the sample, load the sample until the crack extends, and record the critical load. Independently solve the elasticity boundary value problem, and obtain the stress intensity factor in the form (4). The experimentally measured critical load then gives the fracture toughness. The fracture toughness is a material property, which is independent of the sample geometry and load. The stress intensity factor is a loading parameter, which does depend on the sample geometry and the load.

8.7.2.2 On Applying Fracture Mechanics to the Interconnect Structure

SX0095 bib82 Liu *et al.* (2000) have discussed the use of fracture mechanics to formulate design rules for the interconnect structure. For example, assume that the representative stress is set by the thermal mismatch between two materials. The length L can be set to be a feature size, such as film thickness or via diameter. To compute κ, one needs to place a crack in the structure, and know its location, orientation, and size. Such information is never available for a complex structure. A pragmatic approach is to place cracks in the structure hypothetically. For the interconnect structure, the fabrication process controls the structure to the feature size, so that the crack size should not exceed the feature size. Ideally, one wishes to find the worst crack that gives the largest stress intensity factor. In practice, one does calculations for a few representative cracks. Because such an approach is time consuming, broad conclusions drawn from idealized structures are particularly valuable.

SX0100 To make the above discussion concrete, consider the following example (bib83 Lu *et al.*, 1991). Figure 5 sketches the configuration. A cylinder of radius R is embedded in an infinite matrix. For simplicity, we assume that the cylinder and the matrix are both elastic, having similar Young's modulus E and Poisson's ratio v. Set the representative stress by

$$\sigma = E\Delta\alpha\Delta T/(1-v), \tag{6}$$

where $\Delta\alpha$ is the difference in the coefficients of thermal expansion of the two materials, and ΔT the temperature change. This stress, as shown by the elasticity solution, corresponds to the magnitude of the longitudinal stress or twice that of the transverse stress in the cylinder. When the cylinder is under compression, the matrix is under a tensile hoop stress, which decays far away from the interface. We place a crack in the matrix, and ask if this crack will grow. It is sensible to place the crack near the interface and in the radial direction, where the stress is tensile and has a large magnitude. The choice of the crack length requires some thought. When the crack length approaches zero, the stress intensity factor vanishes. When the crack length approaches infinity, the stress intensity factor also vanishes, because of the decaying stress field. Figure 5 sketches the trend of the stress intensity factor as a function of the crack length. This elasticity boundary value problem has been solved analytically, giving the stress intensity factor:

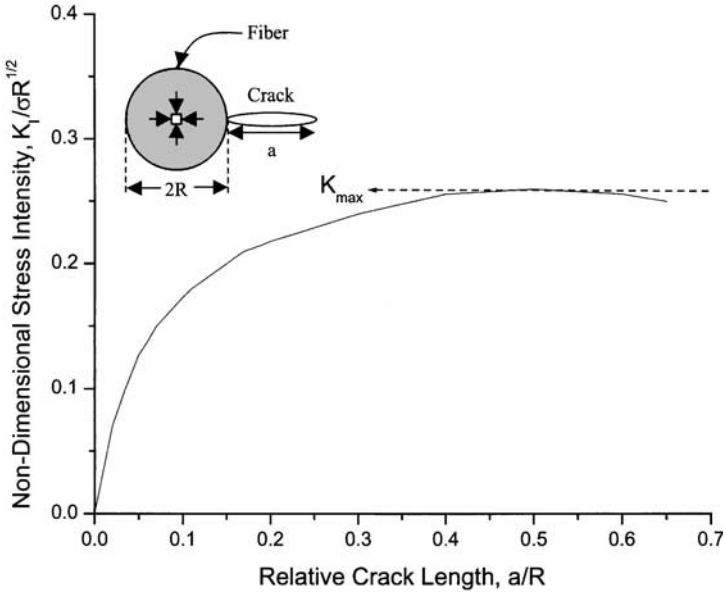

Figure 5 A cylinder is embedded in a matrix. The cylinder is under compression. The tensile hoop stress in the matrix causes cracking. The stress intensity factor is plotted as a function of the crack length.

$$\frac{K}{\sigma\sqrt{R}} = \left(\frac{\pi}{8}\right)^{1/2}\left(\frac{a}{R}\right)\left(1+\frac{a}{R}\right)^{-3/2}. \qquad (7)$$

SX0105 If we can estimate the largest flaw size possible due to a certain fabrication process, we can set the crack size to this flaw size, and then calculate the stress intensity factor. If we know nothing about the flaw, we may proceed as follows. The stress intensity factor (7) attains a maximum, $K_{max} = 0.24\sigma\sqrt{R}$, at $a/R = 0.5$. No matrix flaw can grow provided this maximum stress intensity factor is below the fracture toughness, namely,

$$0.24\,\frac{E\Delta\alpha\Delta T}{1-\nu}\sqrt{R} < K_c. \qquad (8)$$

SX0106 This condition invokes well-defined quantities, and does not rely on any knowledge of the flaw. Everything else being equal, a cylinder with a smaller radius is less likely to cause matrix cracking. Assuming $\sigma = 1$ GPa and $K_c = 1$ MPa $m^{1/2}$, condition (8) gives the critical radius $R_c = 17\,\mu m$.

8.7.2.3 Energy Release Rate

SX0110 Additional insight is gained by analyzing the elastic energy change associated with crack extension. Once again, consider the crack, area A, in an elastic body, subject to a distribution of load that opens the crack. Let F represent the magnitude of the load, and Δ the displacement, such that when Δ changes by $d\Delta$, the load does work $F\,d\Delta$ to the body. Let U be the elastic energy stored in the body. When the displacement varies, but the crack area remains fixed, the work done by the load equals the change in the elastic energy of the body, namely, $dU = F\,d\Delta$ when $dA = 0$. The elastic energy U is represented by the area under the load–displacement curve (Figure 6(a)).

Imagine two copies of the body, identical in SX0115 all respect except for a small difference in the crack areas. The copy with the larger crack is more compliant and, at the same displacement, stores lower elastic energy (Figure 6(b)). Regard the elastic energy stored in the body as a function of the displacement and the crack area, $U(\Delta, A)$. Define energy release rate, G, as the reduction of the elastic energy associated with the crack increasing per unit area, when the external load does no work, namely,

$$G = -\frac{\partial U(\Delta, A)}{\partial A}. \qquad (9)$$

The partial derivative signifies that the displacement Δ is held fixed when the crack area A varies. For a given crack configuration, one can solve the elasticity boundary value problem, compute the elastic energy stored in the body, $U(\Delta, A)$, and then obtain the energy release rate G.

The above definition is still sloppy. In SX0120 general, the energy release rate varies along the crack front. Denote the curved coordinate along the crack front by s, and the energy

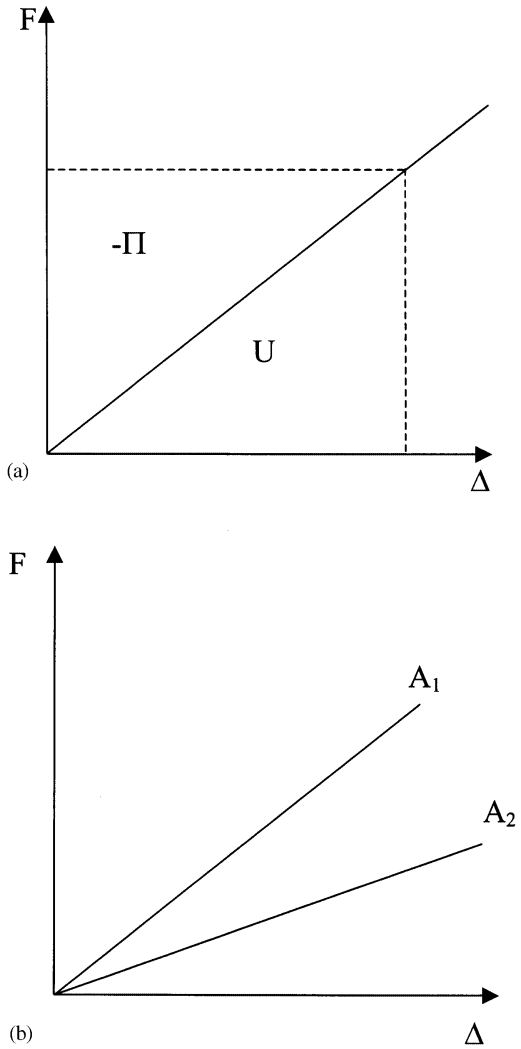

Figure 6 (a) When the crack is stationary in an elastic body, the load is linear in the displacement. The area under the curve represents the elastic energy stored in the body. (b) For the two copies of the elastic body, each containing a stationary crack, the body with a larger crack area (A_2) has a larger compliance.

release rate is a function $G(s)$. Imagine a body subject to a fixed displacement Δ. The elastic energy stored in the body is a function of the crack shape, as well as the crack area. Let the crack advance by a small length δa, which can vary along the crack front. Associated with the change in the crack, the elastic energy stored in the body varies by δU. Define the energy release rate such that

$$\delta U = -\int G(s)\,\delta a\,\mathrm{d}s. \tag{10}$$

The integral extends along the entire crack front. In what follows, we will mostly overlook this detail, and assume that the energy release rate is uniform along the crack front.

When both the displacement and the crack area vary, the elastic energy varies according to SX0121

$$\mathrm{d}U = F\,\mathrm{d}\Delta - G\,\mathrm{d}A. \tag{11}$$

The elastic energy is a function of the displacement and the crack area, $U(\Delta, A)$. The load F and the energy release rate G are the differential coefficients. Just as F is the force conjugate to the displacement Δ, the energy release rate G is the force conjugate to the crack area A. Such a force is known as a configurational force.

Define the potential energy as $\Pi = U - F\Delta$. SX0125 Write Equation (11) in a different form:

$$\mathrm{d}\Pi = -\Delta\,\mathrm{d}F - G\,\mathrm{d}A. \tag{12}$$

Now the potential energy is a function of the load and the crack area, $\Pi(F,A)$. The displacement Δ and the energy release rate G are the differential coefficients. Equation (12) suggests an equivalent definition of the energy release rate:

$$G = -\frac{\partial \Pi(F,A)}{\partial A}. \tag{13}$$

The partial derivative signifies that the load F is held fixed when the crack area A varies. When the body is linearly elastic, $U = F\Delta/2$ and $\Pi = -U$, so that (13) becomes

$$G = +\frac{\partial U(F,A)}{\partial A}. \tag{14}$$

The partial derivative signifies that the load F is held fixed when the crack area A varies. The sign difference in Equations (9) and (14) reflects a simple physical fact. When the crack area is larger, the body is more compliant, so that the body stores less elastic energy at a fixed displacement, but stores more elastic energy at a fixed load.

It has been shown that the energy release rate relates to the stress intensity factor as SX0130

$$G = \frac{K^2}{\bar{E}}, \tag{15}$$

where $\bar{E} = E$ under the plane stress condition, and $\bar{E} = E/(1-\nu^2)$ under the plane strain conditions. Here E is Young's modulus, and ν Poisson's ratio. Fracture mechanics has been formulated either in terms of the stress intensity factor, or the energy release rate. The two formulations are equivalent. Both contribute to the understanding of the fracture mechanics. The simplest fracture condition is that the crack advances when the energy

release rate attains a critical value, Γ, known as the fracture energy. Obviously, the fracture energy relates to the fracture toughness as $\Gamma = K_c^2/\bar{E}$.

8.7.2.4 Channel Cracks in a Thin Film Bonded to a Substrate

SX0135 In an interconnect structure, often a crack runs in one material, but the neighboring material remains intact and exerts a constraint on the crack. Figure 7 illustrates two structures for comparison. In Figure 7(a), a crack of length a, in a freestanding sheet of thickness h, is subject to a tensile stress σ remote from the crack. Assume that the displacement at the load point is fixed, so that the load does no work when the crack extends. When the crack is introduced, the stress near the crack faces is partially relieved. The volume in which the stress relaxes scales as a^2h, so that relative to the uncracked, stressed sheet, the elastic energy in the cracked sheet changes by $\Delta U \sim -a^2h\sigma^2/E$. Consequently, $G \sim a\sigma^2/E$, namely, the energy release rate for a crack in a freestanding sheet increases with the crack length.

SX0140 Figure 7(b) illustrates a thin elastic film bonded to an elastic substrate. When the crack length a is much larger than the film thickness h, the stress field in the crack wake becomes invariant as the crack extends. The volume in which the stress relaxes scales as ah^2, so that the introduction of the crack changes the elastic energy by $\Delta U \sim -ah^2\sigma^2/E_f$. The energy release rate is

$$G = Z\frac{\sigma^2 h}{\bar{E}_f}. \tag{16}$$

The dimensionless number Z depends on the elastic constants of the film and the substrate. The number must be determined by solving the boundary value problem. When the thin film and the substrate have similar elastic constants, $Z = 2.0$. bib11 Beuth (1992) calculated the Z values for a thin film on an infinite substrate with dissimilar elastic constants. When the substrate is stiffer than the film, Z is between 1 and 2. When the substrate is much more compliant than the film, Z can be very large.

SX0145 For the channel crack, the energy release rate scales with the film thickness, and is independent of the crack length when the crack length exceeds several times the film thickness (bib3 Ambrico and Begley, 2002). Take $Z = 2$, $\sigma = 10^9$ Pa, $\bar{E}_f = 10^{11}$ Pa, and $\Gamma = 10\,\mathrm{J\,m^{-2}}$. Equating the energy release rate G in (16) to the fracture energy Γ, we find a critical film thickness $h_c = 0.5\,\mu\mathrm{m}$. Channel cracks can propagate in films thicker than h_c, but not in films thinner than h_c.

SX0150 bib138 Ye *et al.* (1992) have shown that the channel crack energy release rate increases if the crack can dip into the substrate, or the film and substrate can debond. bib4 Ambrico *et al.* (2002) have studied channel cracks multilayers with lateral patterning, with particular reference to interconnects consisting of copper and low-k dielectrics. Using the extended finite element method (XFEM), bib58 Huang *et al.* (2003) have studied the effects of substrate thickness and channel spacing, with particular attention to compliant substrates.

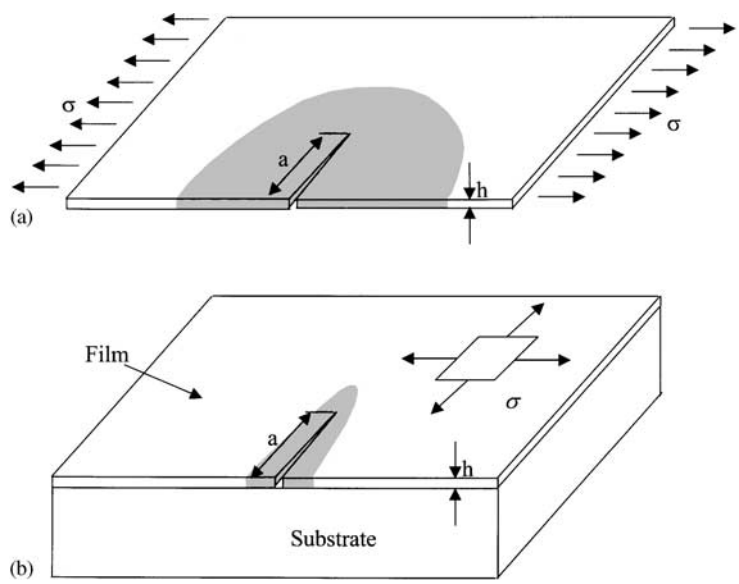

Figure 7 (a) A crack in a freestanding sheet and (b) a channel crack in a thin film bonded to a substrate.

8.7.2.5 Measuring Thin Film Toughness

SX0155 For a brittle solid, toughness is independent of the sample size, so that one may expect to extrapolate toughness measured using bulk samples to thin films. However, thin films used in the interconnect structure are processed under very different conditions from bulk materials, or are unavailable in bulk form at all. Consequently, it is necessary to develop techniques to measure thin film toughness. Such a technique is attractive if it gives reliable results, and is compatible with the interconnect fabrication process. bib85 Ma *et al*. (1998) have developed such a technique, on the basis of channel cracks in a thin film bonded to a silicon substrate. The test procedure consists of two steps (Figure 8): (a) generating pre-cracks, and (b) propagating the cracks using controlled stress. A convenient way of generating pre-cracks is by scratching the surface using a sharp object. A gentle scratch usually generates multiple cracks on the two sides of the scratch. Care must be taken to generate cracks just in the film, but not in the substrate. Use a bending fixture to load the sample, and a digital camera to record the crack growth events. After a crack propagates some distance away from the scratch, the crack grows at a steady velocity.

SX0160 By recording crack growth at slightly different bending loads, one can measure the crack velocity as a function of the stress. The steady velocity is very sensitive to the applied stress. Consequently, the critical stress is accurately measured by controlling the velocity within a certain range that is convenient for the experiment. The critical stress then determines the fracture energy according to the mechanics result (16). The technique has been used to measure the fracture energy of silica ($\Gamma = 16.5\,\mathrm{J\,m^{-2}}$) and silicon nitride ($\Gamma = 8.7\,\mathrm{J\,m^{-2}}$) (bib85 Ma *et al*., 1998), as well as a carbon doped oxide ($\Gamma = 1.5\,\mathrm{J\,m^{-2}}$) (Jun He, private communication).

SX0165 After deposition, the film has a residual stress, σ_R. The residual stress can be measured by the wafer curvature method (bib95 Nix, 1989). When the structure is bent by a moment M (per unit thickness), the film stress becomes

$$\sigma = \sigma_R + \frac{6\bar{E}_f M}{\bar{E}_s H_s^2}, \tag{17}$$

where H_s is the thickness of the substrate, and $\bar{E}_f$ and $\bar{E}_s$ are the plane-strain modulus of the film and the substrate. The bending moment also causes a tensile stress in the substrate, $\sigma_s = 6M/H_s^2$. To measure the toughness of the film, one has to propagate the channel crack in the film without fracturing the substrate. This, in turn, requires that the substrate should have very small flaw size, and that the scratch should not produce flaws in the substrate. When properly cut, the silicon substrate can sustain tensile stresses well over 1 GPa. Inspecting (16) and (17), one concludes that the technique is inapplicable when the film has a very large fracture energy, large residual compressive

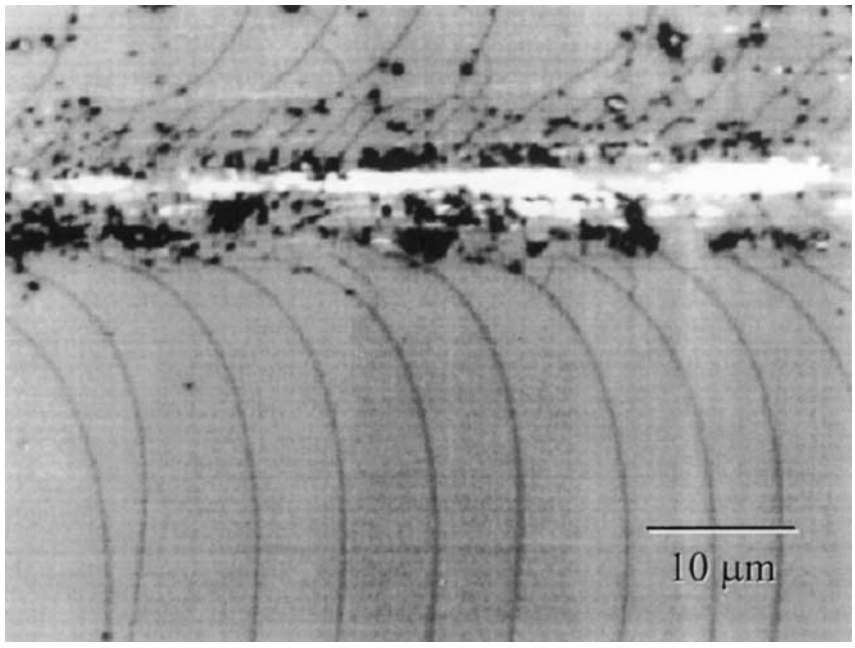

Figure 8 A micrograph of cracked film surface. Initial cracks are introduced by a scratch. When a bending load is applied, the cracks propagate in the direction normal to the bending stress.

stress, small thickness, or low modulus. In the experiment of bib85 Ma *et al.* (1998), a thin metal layer is deposited on the silicon substrate, and the brittle film is deposited on the metal. The metal layer serves as a barrier preventing the crack from entering the substrate. The metal layer, upon yielding, also increases the energy release rate for a given bending moment (Section 8.7.2.6).

SX0170 One may also greatly amplify the energy release rate for a given stress by using the structure in Figure 9. The cavity underneath the brittle film may be made by MEMS fabrication method. When the crack grows, the stress in the film is relaxed, and the energy release rate,

$$G = \frac{\sigma^2 L}{\bar{E}_f}, \tag{18}$$

now scales with the length of the cavity, rather than the film thickness.

8.7.2.6 The Effect of Underlayer on Channel Crack

SX0175 When a brittle film is bonded to a plastically deformable substrate, the constraint of the substrate on the crack in the film is partially lost. In the limiting case, when the yield strength of the substrate is much below the stress in the film, the film is equivalent to a freestanding sheet. Consequently, the plastic deformation in the substrate encourages the channel cracks in the film. This effect has been studied by bib54 Hu and Evans (1989) by using a shear lag model, by bib12 Beuth and Klingbeil (1996) for a brittle film on a semi-infinite elastic–plastic substrate, and by bib3 Ambrico and Begley (2002) for a brittle film on a ductile underlayer. In this section, using a shear lag model, we (bib118 Suo and He, 2002) examine the structure depicted in Figure 10, consisting of an overlayer, an underlayer, and a substrate. The crack cuts across the overlayer, with the crack root arresting at the interface between the overlayer and the underlayer. The overlayer is taken to be elastic, and the substrate is rigid. The property of the underlayer will be varied to study its effect on the channel crack.

SX0180 The overlayer may consist of multiple brittle films. The stress in the overlayer is a function of the position through the thickness, $\sigma(z)$. Define the membrane force in the overlayer by

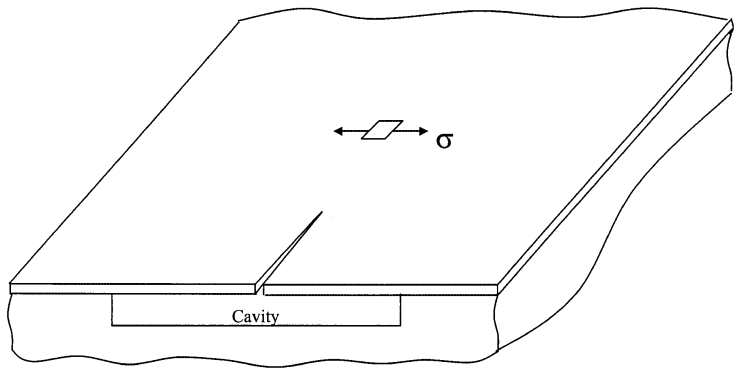

Figure 9 When the film is above a wide cavity, the crack driving force increases greatly.

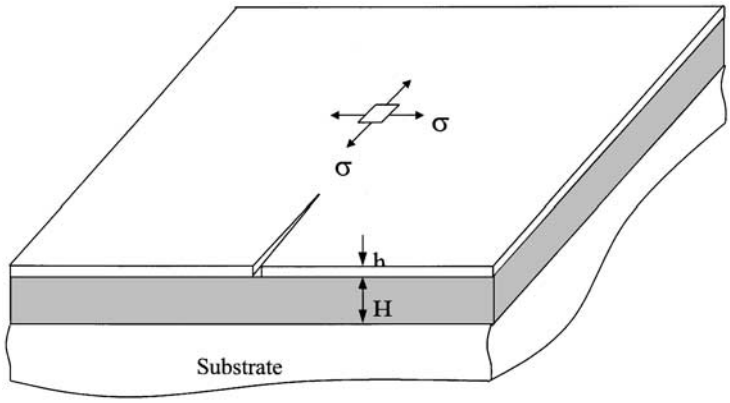

Figure 10 A structure consists of an elastic overlayer, an elastic–plastic underlayer, and a rigid substrate.

$$N = \int \sigma(z)\,\mathrm{d}z. \tag{19}$$

The integral extends over the thickness of the overlayer. Similarly, define the membrane stiffness by

$$B = \int \bar{E}(z)\,\mathrm{d}z, \tag{20}$$

where $\bar{E}(z)$ is the plane strain modulus of the material at z.

SX0190 We now consider the wake of the crack in the overlayer on a ductile underlayer. When the overlayer is uncracked, subject to a membrane force N_∞, uniform in the plane of the layer, the displacement field in the overlayer is set to be zero. Relative to this reference state, the overlayer deforms when a crack is introduced. Let $u(x)$ be the displacement field averaged across the thickness of the overlayer. On the interface, the overlayer and the underlayer interact with each other through the shear stress field $\tau(x)$. We model the underlayer as a time-independent elastic plastic material, with a nonlinear relation between the shear stress τ and the displacement u.

SX0191 When a crack cuts across the thickness of the overlayer at $x=0$, the membrane force in the overlayer, $N(x)$, varies with the position, having the boundary conditions $N(0)=0$ and $N(\infty)=N_\infty$. Hooke's law relates the membrane force to the displacement gradient:

$$N(x) = N_\infty + B\frac{\mathrm{d}u}{\mathrm{d}x}. \tag{21}$$

The force balance of an element of the overlayer requires that

$$\frac{\mathrm{d}N}{\mathrm{d}x} = \tau. \tag{22}$$

Inserting (21) into (22), we obtain the ordinary differential equation for $u(x)$:

$$B\frac{\mathrm{d}^2u}{\mathrm{d}x^2} = \tau(u). \tag{23}$$

SX0195 Multiplying (23) by $\mathrm{d}u/\mathrm{d}x$, and integrating from $x=0$ to $x=\infty$, we obtain that

$$\frac{N_\infty^2}{2B} = \int_0^{u_0} \tau(u)\,\mathrm{d}u. \tag{24}$$

In reaching the above equation, we have used the following boundary conditions: $u=u_0$ and $\mathrm{d}u/\mathrm{d}x=-N_\infty/B$ at $x=0$, and $u=0$ and $\mathrm{d}u/\mathrm{d}x=0$ at $x=\infty$. When the underlayer property $\tau(u)$ is known, (24) provides the relation between the crack opening displacement u_0 and the membrane force N_∞ in the uncracked overlayer.

For a multi-material overlayer, the energy release rate depends on the position, $G(z)$. The integral SX0200

$$f = \int G\,\mathrm{d}z \tag{25}$$

gives the elastic energy change associated with the crack advancing per unit length in the overlayer. The quantity f has the unit of force, and is the driving force for the channel crack.

The channel driving force is given by the complementary energy integral (bib12 Beuth and Klingbeil, 1996): SX0205

$$f = 2\int_0^{N_\infty} u_0\,\mathrm{d}N_\infty. \tag{26}$$

Once the u_0–N_∞ relation is obtained from (24), the driving force for the channel crack is calculated from (26).

We next list solutions for idealized material law, $\tau(u)$. We assume that the underlayer has the uniform property, and the shear stress is constant across the thickness of the underlayer. Consequently, the shear strain γ is also constant across the thickness of the underlayer. The shear strain relates to the overlayer displacement as $\gamma(x)=u(x)/H$, where H is the thickness of the underlayer. SX0210

Elastic underlayer. The underlayer is linear elastic with shear modulus μ, so that $\tau=\mu u/H$. Integrating (24), we obtain the u_0–N_∞ relation SX0215

$$u_0 = N_\infty\sqrt{\frac{H}{\mu B}}. \tag{27}$$

Integrating (26) gives the driving force for the crack in the overlayer:

$$f = N_\infty^2\sqrt{\frac{H}{\mu B}}. \tag{28}$$

This result reproduces that obtained by bib141 Xia and Hutchinson (2000). As expected, the crack driving force is quadratic in the membrane force. At a given membrane force, the crack driving force is large when the underlayer is thick and compliant. This result is applicable to, for example, a nitride passivation film on a complaint dielectric layer. As the microelectronic industry implements low-dielectric-constant materials, with accompanying low

stiffness, the likelihood of cracking in the brittle passivation film will increase.

SX0220 *Rigid, perfect plastic underlayer.* Neglect elasticity of the film, and assume that the underlayer deforms plastically at a constant stress $\tau = \tau_Y$. Integrating (24), we obtain the u_0–N_∞ relation

$$u_0 = \frac{N_\infty^2}{2B\tau_Y}. \tag{29}$$

Inserting into (26) gives driving force for the crack in the overlayer:

$$f = \frac{N_\infty^3}{3B\tau_Y}. \tag{30}$$

This reproduces the result of bib54 Hu and Evans (1989). The crack driving force is cubic in the membrane force, inversely proportional to the underlayer yield strength, and independent of the underlayer thickness.

SX0225 *Elastic, perfectly plastic underlayer.* The film now has the shear modulus μ, the yield strength τ_Y, and the yield strain $\gamma_Y = \tau_Y/\mu$. When $u_0 < \gamma_Y H$, the film is elastic, and (27) provides the u_0–N_∞ relation. When $u_0 > \gamma_Y H$, a segment of the film near the crack deforms plastically, and the film fare from the crack is still elastic. Using (27), we write the yield condition in terms of the membrane force:

$$\frac{N_\infty}{\sqrt{\tau_Y \gamma_Y HB}} = 1. \tag{31}$$

Integrating (24), we obtain the opening displacement of the crack wake

$$\frac{u_0}{\gamma_Y H} = \frac{1}{2} + \frac{1}{2}\left(\frac{N_\infty}{\sqrt{\tau_Y \gamma_Y HB}}\right)^2. \tag{32}$$

This is the u_0–N_∞ relation when $N_\infty/\sqrt{\tau_Y \gamma_Y HB} > 1$; for smaller N_∞, the film is elastic, and the u_0–N_∞ relation is given by (27). Inserting the whole u_0–N_∞ relation into (26), we find the driving force for the crack in the overlayer:

$$f = \frac{N_\infty^3}{3B\tau_Y}\left[1 - \left(\frac{N_\infty}{\sqrt{\tau_Y \gamma_Y HB}}\right)^{-3} + 3\left(\frac{N_\infty}{\sqrt{\tau_Y \gamma_Y HB}}\right)^{-2}\right] \tag{33}$$

When $N_\infty/\sqrt{\tau_Y \gamma_Y HB} = 1$, the underlayer is elastic, and (33) recovers (28). When $N_\infty/\sqrt{\tau_Y \gamma_Y HB} \gg 1$, the two terms in the bracket is negligible, and (33) recovers the result for the rigid perfect plastic case (30).

SX0230 *Power-law plastic underlayer.* Now we assume that the film deforms according to the power law

$$\frac{\tau}{\tau_Y} = \left(\frac{u}{H\gamma_Y}\right)^n, \tag{34}$$

where τ_Y is an arbitrarily selected reference stress, and γ_Y and n are parameters used to fit experiment data. Following the same procedure as before, we obtain the u_0–N_∞ relation

$$\frac{u_0}{\gamma_Y H} = \left[\frac{(n+1)N_\infty^2}{2\tau_Y \gamma_Y HB}\right]^{1/(n+1)}, \tag{35}$$

and the crack driving force

$$f = \frac{2\gamma_Y H}{n+3}\left[\frac{(n+1)^{n+2} N_\infty^{n+3}}{2BH\tau_Y \gamma_Y}\right]^{1/(n+1)}. \tag{36}$$

This equation recovers the linear elastic case Equation (28) when $n = 1$, and the rigid perfect plastic case Equation (30) when $n = 0$.

Figure 11 plots the normalized channel driving force, $f/(H\gamma_Y\sqrt{\tau_Y \gamma_Y HB})$, as a function of the normalized membrane force, $N_\infty/\sqrt{\tau_Y \gamma_Y HB}$. As expected, for the same membrane force, the more deformable the underlayer, the larger the channel driving force. SX0235

8.7.2.7 Crack Kinetics: Subcritical Cracking and Substrate Creep

As mentioned above, the crack extends in the thin film at some finite velocity. The magnitude of the velocity is sensitive to the stress, but in general is much below the speed of the elastic waves in the solids. Consequently, the observed crack velocity should not be an inertia effect. If the brittle solid does not creep, the time dependence originates from either the bond-breaking process, or the time-dependent deformation in the surrounding materials. SX0240

Slow crack growth has been extensively studied in bulk brittle materials, where the bond-breaking process is assisted by environmental molecules, such as water molecules (bib74 Lawn, 1993). The time dependence results from the transport of the environmental molecules to the crack front, and the reaction at the crack front. The crack velocity can be measured experimentally as a function of the energy release rate. bib85 Ma *et al.* (1998) and bib23 Cook and Liniger (1999) have provided data for several thin films. The measured V–G curve is sometimes fit to a variety of empirical relations. One such a relation, suggested by the consideration of microscopic mechanisms, is SX0245

$$V = V_0 \sinh\left[\beta\left(\frac{G}{G_{th}} - 1\right)\right], \tag{37}$$

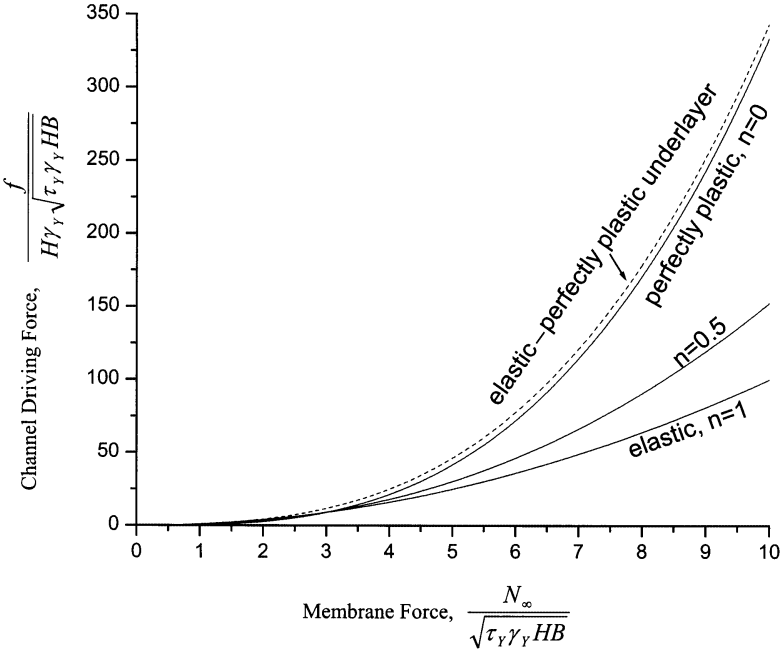

Figure 11 The driving force for channel crack as a function of the membrane force. Several underlayer behaviors are compared: elastic, perfectly plastic, elastic–plastic, elastic–perfectly-plastic, and power law.

where V_0, G_{th} and β are parameters to fit experimental data.

SX0250 I owe Dr. Jun He, of Intel Corporation, for the following idea. The V–G curve is specific to the brittle material and the environment, but is independent of the surrounding materials, if they do not prevent the environmental molecules from reaching the crack front. The V–G curve for a given material can be measured using a simple structure, such as a film on a silicon substrate. When the brittle material is in a more complex structure, the same V–G still applies. Because the crack velocity is readily measurable, the measured crack velocity, together with the known V–G curve, determines the energy release rate. The method is accurate because the crack velocity sensitively depends on the energy release rate. As we have seen in Figure 11, the energy release rate is affected by the deformation behavior of the surrounding materials. Direct measurements of G provide a means to study the deformation behavior of the surrounding materials.

SX0255 The crack velocity is also affected if the surrounding materials creep. As an example, consider the structure illustrated in Figure 10 again, now assume that the underlayer is viscous (bib78 Liang *et al.*, 2002a). Initially, the film is in a uniform biaxial tensile stress state σ. When the underlayer creeps, the stress field in the film *relaxes* in the crack wake, but *intensifies* around the crack tip. When the crack tip moves slowly, the crack wake has a long time to relax, and the stress intensity around the crack tip increases. When the crack tip moves rapidly, the crack wake has a short time to relax, and the stress intensity around the crack tip decreases. Consequently, the crack can attain a steady velocity, given by

$$V = 0.6\frac{Hh\sigma^2}{\eta G}. \tag{38}$$

SX0256 As expected, the larger the steady velocity, the smaller the energy release rate. If the film is susceptible to subcritical crack growth, one can separately determine the V–G curve of the material, e.g., using the film on an elastic substrate. Once the crack velocity V is measured for the film on the viscous underlayer, one can read the energy release rate G form the V–G curve. The measured V and G, together with Equation (38), provide a means to determine the viscosity of the underlayer.

8.7.3 DEBONDING AND MIXED MODE CRACK

SX0260 The interconnect structure consists of many dissimilar materials. Debonding has been a primary concern. Figure 12 is a micrograph of a thin film debonding from a substrate. Within the linear elastic fracture mechanics, we model the debond process as a crack extending on the interface between two elastic materials. Impurities, of minute amount by volume fraction,

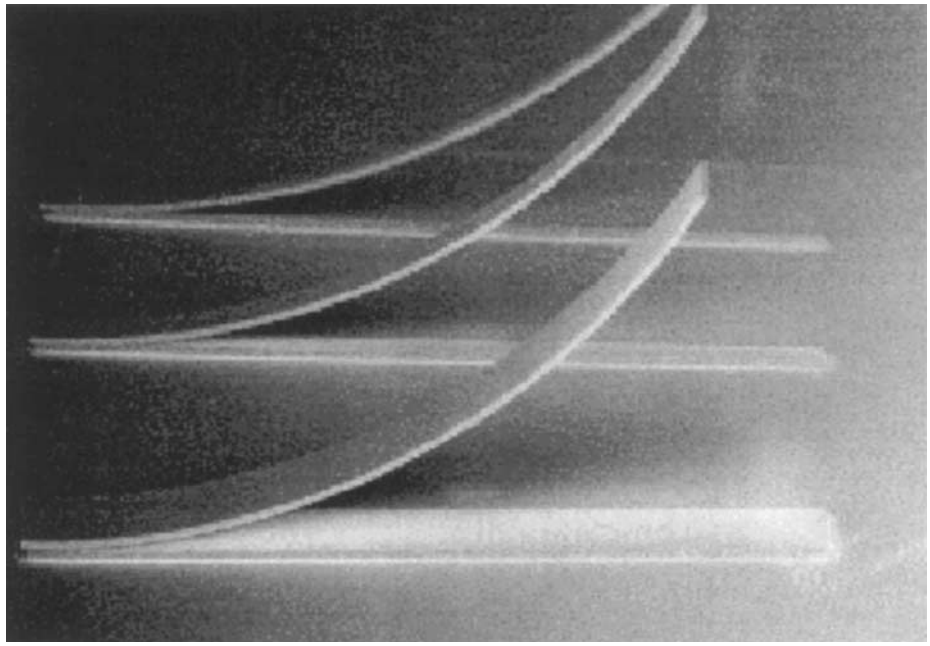

Figure 12 Debond from an edge of the film, driven by residual tensile stress in the film. When the debond front approaches the other edge of the film, the debond driving force decreases, so that the debond arrests before it reaches the film edge (courtesy of Q. Ma, Intel Corporation).

may accumulate on the interface to a large coverage, significantly changing the interfacial fracture energy. Adhesion sensitively depends on processing conditions, and on materials deliberately added to the interface. Measurements of the interfacial fracture energy provides tools for process control and material selection to promote adhesion in interconnect structures.

SX0265 It is instructive to compare a crack running on a bimaterial interface to a crack running in a homogenous, isotropic material. A crack in a homogenous, isotropic material extends along such a path that the crack tip is always under the tensile condition. Consequently, the crack tip often follows a curved path, and the fracture property of a given material is prescribed by a single quantity, the mode I fracture toughness. By contrast, the crack confined on a bimaterial interface often propagates under the combined tensile and shear conditions. The fracture energy depends on the relative proportion of the tensile and shear loads.

SX0270 This section will begin with a discussion of a stationary, planar crack in a homogenous, isotropic material, subject to the mixed mode conditions. The crack grows to seek a mode I path. We then outline the interfacial fracture mechanics, the methods to measure the fracture energy as a function of the mode angle, and the applications to interconnect structures. We finally examine the effect of plastic deformation on debonding.

8.7.3.1 Mixed Mode Crack in a Homogeneous Material

SX0275 First examine a stationary, planar crack in a homogenous, isotropic material. The body is subject to a distribution of load that can both open and shear the crack. Let (r,θ) be the polar coordinates centered at a given point on the crack front (Figure 13). We will consider the situation that the shear load is in the plane (r,θ). The stress field near the crack front has the form

$$\sigma_{ij}(r,\theta) = \frac{K_{\mathrm{I}}}{\sqrt{2\pi r}}\Sigma_{ij}^{\mathrm{I}}(\theta) + \frac{K_{\mathrm{II}}}{\sqrt{2\pi r}}\Sigma_{ij}^{\mathrm{II}}(\theta). \qquad (39)$$

The θ-dependent functions, $\Sigma_{ij}^{\mathrm{I}}(\theta)$ and $\Sigma_{ij}^{\mathrm{II}}(\theta)$, can be found in bib74 Lawn (1993). The mode I field is symmetric with the crack plane, with $\Sigma_{22}^{\mathrm{I}}(0) = 1$ and $\Sigma_{12}^{\mathrm{I}}(0) = 0$. The mode II field is antisymmetric with the crack plane, with $\Sigma_{22}^{\mathrm{II}}(0) = 0$ and $\Sigma_{12}^{\mathrm{II}}(0) = 1$. In particular, the stresses on the plane $\theta = 0$ a distance r ahead the crack front are

$$\sigma_{22}(r,0) = \frac{K_{\mathrm{I}}}{\sqrt{2\pi r}}, \qquad \sigma_{12}(r,0) = \frac{K_{\mathrm{II}}}{\sqrt{2\pi r}}. \qquad (40)$$

The stress intensity factors, K_{I} and K_{II}, scale the amplitudes of opening and shearing loads,

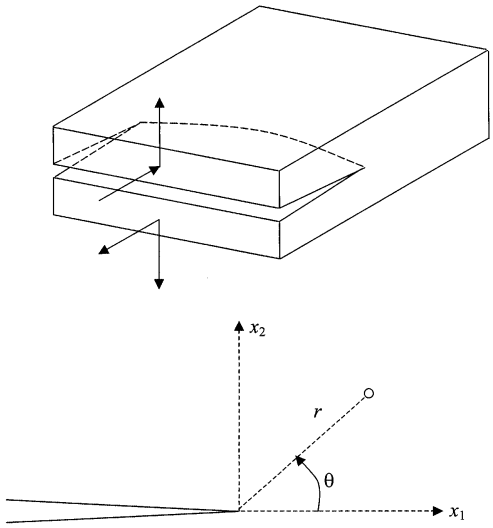

Figure 13 A crack in a body subject to both the opening and shearing loads.

respectively. We will be interested in situations where the crack front is under tension, rather than compression, namely, $K_I \geq 0$.

SX0280 Once a crack configuration is prescribed, the stress intensity factors K_I and K_{II} are determined by solving the elasticity boundary value problem. For example, for a crack of length $2a$ in an infinite sheet, subject to remote tensile stress σ and shear stress τ, the two stress intensity factors are $K_I = \sigma\sqrt{\pi a}$ and $K_{II} = \tau\sqrt{\pi a}$. Solutions for many crack configurations have been collected in handbooks (e.g., bib122 Tada *et al.*, 1985). Finite element methods have been used routinely to determine the stress intensity factors under the mixed mode conditions (bib77 Li *et al.*, 1985).

SX0285 Again, the stress field (39) is valid in an annulus, with the inner radius larger than the zone of the bond-breaking process, and the outer radius smaller than a length representative of the external boundary conditions. The mixed mode conditions are characterized by two loading parameters, K_I and K_{II}. The two "messengers" transmit the boundary conditions to the crack tip process. The relative amount of mode II to mode I is specified by the mode angle ψ, defined by

$$\tan\psi = K_{II}/K_I. \tag{41}$$

With $K_I \geq 0$, the mode angle ranges between $-\pi/2 \leq \psi \leq \pi/2$. A pure mode I crack corresponds to $\psi = 0$ and pure mode II crack to either $\psi = +\pi/2$ or $\psi = -\pi/2$.

SX0290 The energy release rate G is still defined as the elastic energy reduction as the crack extends unit area, while the load does no additional work. The energy release rate relates to the two stress intensity factors by

$$G = \frac{1}{\bar{E}}(K_I^2 + K_{II}^2). \tag{42}$$

Instead of using K_I and K_{II} to represent the external loads, we use G to represent the amplitude of the loads, and ψ to represent the mode of the loads.

Under the mixed mode conditions, upon SX0295 growing, the planar crack often kinks at an angle from its original plane. The kink angle depends on the relative amount of mode II to mode I load. bib29 Erdogan and Sih (1963) showed that the experimentally measured kink angles in a plexiglass are well predicted by the criterion that the crack kinks to the plane with the maximum hoop stress. For the stationary crack, the hoop stress near the crack tip is

$$\sigma_{\theta\theta}(r,\theta) = \frac{K_I}{\sqrt{2\pi r}}\cos^3\left(\frac{\theta}{2}\right) - \frac{K_{II}}{\sqrt{2\pi r}}3\cos^2\left(\frac{\theta}{2}\right)\sin\left(\frac{\theta}{2}\right). \tag{43}$$

The hoop stress maximizes at an angle θ^*, given by

$$\tan\left(\frac{\theta^*}{2}\right) = -\frac{2\tan\psi}{1+\sqrt{1+8\tan^2\psi}}. \tag{44}$$

When $K_{II} > 0$, $\psi > 0$ and the crack kinks down (i.e., $\theta^* < 0$). The converse is true when $K_{II} < 0$. When the plane crack is pure mode I, this criterion predicts that the crack extends straight ahead. When the plane crack is pure mode II, this criterion predicts that the crack kinks at an angle $\theta^* = 70.5^\circ$.

The moving crack tip seeks a trajectory that SX0300 is locally mode I; any nonzero K_{II} will cause the crack to deflect. To illustrate this point, consider two examples. It is well known that a crack in a double-cantilever beam is unstable: the crack tends to curve one way or the other (Figure 14). By symmetry, the crack on the mid-plane of the sample is pure mode I. This mode I path, however, is unstable. A crack, lying slightly off the mid-plane, has a mode II component that tends to deflect the crack further away from the mid-plane.

As a second example, Figure 15 illustrates a SX0305 thin film spalling from an adherent substrate (bib125 Thouless *et al.*, 1987). The film is well bonded to the substrate, and is under a residual tensile stress. It is sometimes observed that a crack starts from the edge of the film, dives into the substrate, and then grows parallel to the interface. In the crack wake, the residual stress in the film is partially relieved, and the film and a thin layer of the substrate material underneath form a composite plate, bending up. This

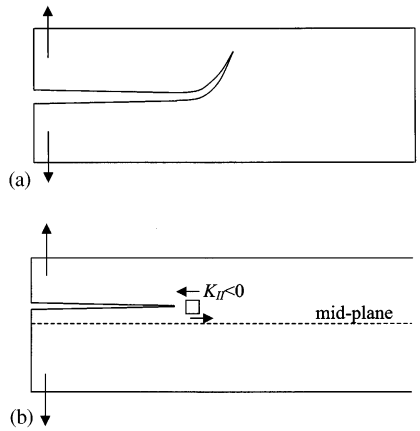

Figure 14 (a) A crack in a double-cantilever beam tends to curve away from the mid-plane. (b) A crack slightly away from the mid-plane has a mode II component in the direction that drives the crack further away from the mid-plane.

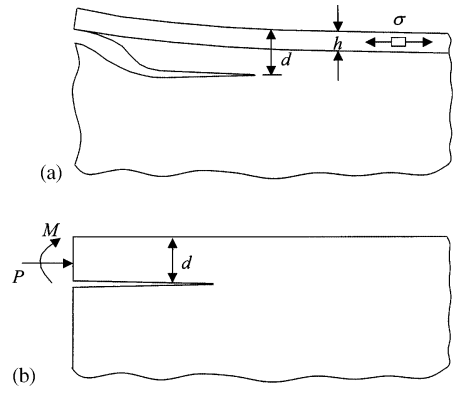

Figure 15 (a) Schematic of a thin film spalling from an adherent substrate, driven by the tensile stress in the film. The crack runs along a path parallel to the interface. (b) The effective axial force and bending moment caused by the residual stress.

observation is peculiar in that, were the crack to run on the film–substrate interface, the residual stress in the film would be fully relieved in the crack wake. Such a global energy consideration has no physical basis: it is the local process of bond breaking that selects the crack path. The experimental observation has been interpreted that the crack tip moves along a mode I trajectory. To see how this works, consider a special case that the thin film and the substrate have similar elastic modulus. Let h be the film thickness, and d be the depth of the crack parallel to the interface. When the crack is long compared to d, the effect of the residual stress on the crack is well described by the equivalent axial force and bending moment:

$$P = \sigma h, \quad M = \tfrac{1}{2}\sigma h(d-h). \tag{45}$$

The stress intensity factors have been calculated, given by

$$K_{\mathrm{I}} = \frac{1}{\sqrt{2}}(Pd^{-1/2}\cos\omega + 2\sqrt{3}Md^{-3/2}\sin\omega), \tag{46a}$$

$$K_{\mathrm{II}} = \frac{1}{\sqrt{2}}(Pd^{-1/2}\sin\omega - 2\sqrt{3}Md^{-3/2}\cos\omega), \tag{46b}$$

with $\omega \approx 52^\circ$. Suppose that the crack selects the depth d^* by the condition that $K_{\mathrm{II}} = 0$, and we obtain that $d^* = 3.8\,h$. One can further confirm that the mode I path is stable in that, if a parallel crack at a depth d different from d^*, then K_{II} is nonzero and is in the direction that tends to deflect the crack back toward the depth d^*.

SX0310 Curved crack paths can be simulated using numerical methods. For a given crack configuration, one solves the elasticity boundary value problem, and computes the stress intensity factors K_{I} and K_{II}. One then advances the crack by a small length in the direction, say, set by the criterion of maximum hoop stress (Equation (44)). The path so selected should be essentially a mode I path. For a single crack tip, the precise length for each increment is unimportant, so long as it is much smaller than the representative size of the sample. To simulate simultaneous growth of multiple cracks, however, one has to know how much to advance each crack. An ingredient of time dependence has to be introduced into the model. For example, if the solid is susceptible to subcritical cracking (Section 8.7.2.7), the V–G relation provides the needed information. Once the energy release rate is calculated for every crack tip in a given configuration, one advances each crack according to the kinetic law for a small time step. Similarly, one can simulate the growth of a crack in three dimensions with a curved front by advancing each point on the crack front according to the kinetic law and its local energy release rate. Because the crack extends under the mode I conditions, the V–G curve can be obtained experimentally using a specimen containing a single straight mode I crack.

SX0315 The regular finite element method meshes the geometry of the crack and uses a fine mesh near the crack tip. When the crack grows, remeshing is required. To circumvent these difficulties, XFEM has been advanced (bib92 Moes *et al.*, 1999). For the nodes around the crack tip, one adds enriching functions derived from the singular crack-tip stress field. For nodes on the crack faces, one adds the Heaviside function to represent the displacement

jump. Consequently, the mesh can be coarse near the crack tip, and the elements need not conform to the crack geometry. As the cracks grow, one updates the nodes to be enriched. No remeshing is necessary. Figure 16 shows the simulated mud-crack pattern in tensile film bonded to a substrate (bib79 Liang *et al.*, 2002b).

8.7.3.2 Interfacial Fracture Mechanics

SX0320 AU:1 Now consider a crack on the interface between two elastic materials. Williams (1959) discovered that the singular stress field at the interface crack tip is not square-root singular. The stresses on the interface a distance r ahead of the crack tip take the form

$$\sigma_{22} + i\sigma_{12} = \frac{Kr^{i\varepsilon}}{\sqrt{2\pi r}}. \tag{47}$$

The notation of complex numbers is used: $i = \sqrt{-1}$ and $r^{i\varepsilon} = e^{i\varepsilon \ln r} = \cos(\varepsilon \ln r) + i \sin(\varepsilon \ln r)$. The bimaterial constant ε is defined by

$$\varepsilon = \frac{1}{2\pi} \ln \left[\frac{(3 - 4\nu_1)/\mu_1 + 1/\mu_2}{(3 - 4\nu_2)/\mu_2 + 1/\mu_1} \right], \tag{48}$$

where ν is Poisson's ratio, μ the shear modulus, and the subscripts 1 and 2 refer to the two materials. The constant is bounded, $|\varepsilon| < (1/2\pi) \ln 3 \approx 0.175$.

SX0325 The stress intensity factor K is complex valued, and has the dimension

$$K = [\text{stress}]\,[\text{length}]^{1/2 - i\varepsilon}. \tag{49}$$

The amplitude of the stress intensity factor has the familiar dimension, $|K| = [\text{stress}][\text{length}]^{1/2}$. Indeed, $|K|$ relates to the energy release rate as

$$G = \frac{1}{2}\left(\frac{1}{\bar{E}_1} + \frac{1}{\bar{E}_2}\right) \frac{|K|^2}{\cosh^2(\pi\varepsilon)}. \tag{50}$$

For a given crack configuration, the stress intensity factor K is determined by solving the elasticity boundary value problem. Finite element method and other numerical methods have been developed to determine the stress intensity factor (Matos *et al.*, 1990). bib61 AU:2 Hutchinson and Suo (1991) have compiled solutions for layered materials.

SX0330 Following bib101 Rice (1988), we define the mode angle ψ by

$$K = |K| l^{-i\varepsilon} \exp(i\psi), \tag{51}$$

where l is an arbitrary length. To see the consequence of this definition, combine (47) and (51), yielding

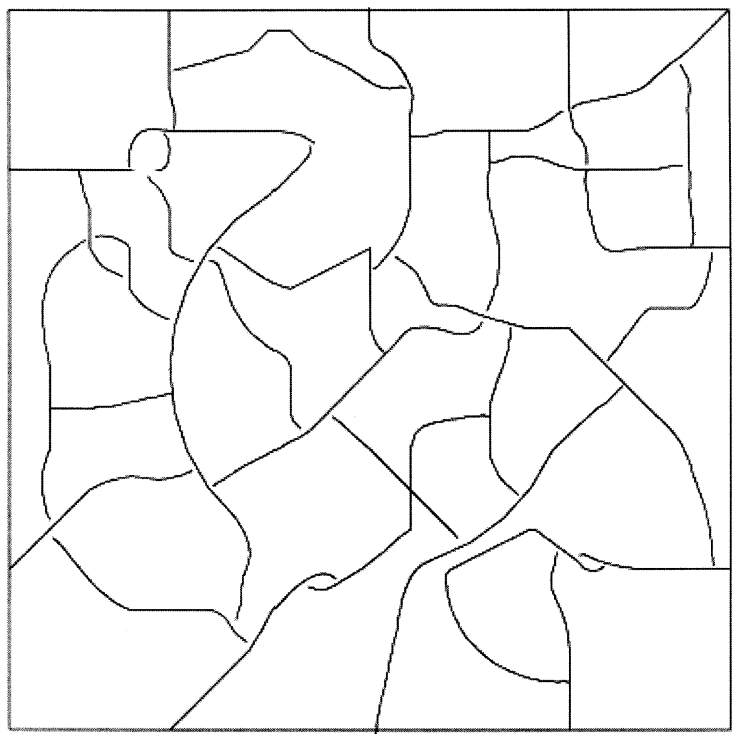

Figure 16 Mud-crack pattern simulated by using the XFEM.

$$\sigma_{22} + \mathrm{i}\,\sigma_{12} = \frac{|K|}{\sqrt{2\pi r}} \mathrm{e}^{\mathrm{i}[\psi + \varepsilon \ln(r/l)]}. \quad (52)$$

The ratio of the shear stress to the tensile stress is

$$\sigma_{12}/\sigma_{22} = \tan[\psi + \varepsilon \ln(r/L)]. \quad (53)$$

SX0331 When $\varepsilon = 0$, as for a crack in a homogenous material, the ratio σ_{12}/σ_{22} is independent of the distance r in the K-annulus, and the mode angle ψ characterizes the relative portion of shear to tension. When $\varepsilon \neq 0$, the ratio σ_{12}/σ_{22} varies with the distance r, and equals $\tan\psi$ at $r = l$. The variation is not rapid, because ε is small and because a logarithm is a slowly varying function. Thus, $\tan\psi$ approximates the ratio σ_{12}/σ_{22} so long as r is not far from l. For a brittle interface, a natural choice is $l = 1$ nm, representative of the bond-breaking zone size. With this choice, the mode angle ψ represents the relative portion of shear to tension at the size scale of bond-breaking zone.

SX0340 In a homogeneous material, crack faces come into contact under compression. By contrast, interface crack faces may come into AU:3 contact even when the remote load has a tensile component. When the contact zone is large, one has to take into account the forces on the crack faces in solving the boundary value problem. In many situations, however, the contact zone is small compared to the overall dimension. Consequently, the K-annulus exists, with the inner radius enclosing the contact zone, as well as the bond-breaking process zone. bib101 Rice (1988) has examined the condition for small-scale contact.

SX0345 Williams's elastic solution shows that the displacement jump at a distance r behind the crack tip is

$$\delta_2 + \mathrm{i}\delta_1 = \left(\frac{1}{\bar{E}_1} + \frac{1}{\bar{E}_2}\right) \frac{K r^{\mathrm{i}\varepsilon}}{2(1 + 2\mathrm{i}\varepsilon)\cosh(\pi\varepsilon)} \sqrt{\frac{2r}{\pi}}. \quad (54)$$

The jump in the displacement component normal to the crack faces is

$$\delta_2 = \delta \cos[\psi + \varepsilon \ln(l/r) - \tan^{-1}(2\varepsilon)], \quad (55)$$

where $\delta = (\delta_1^2 + \delta_2^2)^{1/2}$ is the magnitude of the displacement jump. If the crack is required to be open within $l < r < 100\,l$, the mode angle must be restricted within

$$\begin{aligned} -\pi/2 + 2\varepsilon < \psi < \pi/2 + 2.6\varepsilon, &\quad \text{for } \varepsilon > 0 \\ -\pi/2 - 2.6\varepsilon < \psi < \pi/2 + 2\varepsilon, &\quad \text{for } \varepsilon < 0 \end{aligned} \quad (57)$$

The number 100 is arbitrary, but the condition in (57) is insensitive to this number. When $\varepsilon = 0$, the above condition simply says that the contact does not occur when the crack is under tension, which is known for homogeneous materials.

As an example, consider a crack, length $2a$, SX0350 on the interface between two semi-infinite materials, subject to remote tensile stress σ and shear stress τ. Write $\sigma + \mathrm{i}\tau = T\mathrm{e}^{\mathrm{i}\omega}$, so that T is the magnitude, and ω the direction, of the remote load. This elasticity boundary value problem has been solved analytically, giving the stress intensity factor (bib101 Rice, 1988)

$$K = (1 + 2\mathrm{i}\varepsilon)\sqrt{\pi a}(2a)^{-\mathrm{i}\varepsilon} T \mathrm{e}^{\mathrm{i}\omega}. \quad (58)$$

The energy release rate is obtained by inserting (58) into (50). A comparison of (51) and (58) gives the mode angle:

$$\psi = \omega + \tan^{-1}(2\varepsilon) + \varepsilon \ln(l/2a). \quad (59)$$

When $\varepsilon = 0$, the mode angle ψ equals the angle ω of the remote load. The two angles are different when $\varepsilon \neq 0$. Consider representative values, $\varepsilon = -0.05$, $l = 1$ nm, and $2a = 1$ mm. Under remote tension, $\omega = 0$, one finds that $\psi = 34^\circ$, indicating a significant shear component near the crack tip, at the size scale of bond-breaking zone.

As a second example, consider the debond- SX0355 ing of a thin film from a substrate. A film, thickness h, is under a tensile inplane stress σ and initially bonded to the substrate. The film may debond from the root of a channel crack, or from the edge of the film. When the debond length exceeds several times the film thickness, the debonding process attains a steady state, in which the energy release rate is independent of the debond length. Under the plane-strain conditions, an elementary consideration gives the energy release rate

$$G = \frac{\sigma^2 h}{2\bar{E}_\mathrm{f}}. \quad (60)$$

The debond crack is under the mixed mode conditions. The mode angle must be determined by solving the elasticity boundary value problem. When the film and the substrate have similar elastic constants, the stress intensity factors are given by (46), setting $P = \sigma h$ and $M = 0$. The mode angle is $\psi \approx 52^\circ$. Next, examine the effect of the modulus mismatch on the mode angle. The complex stress intensity factor is given in the form

$$K = |K| h^{-\mathrm{i}\varepsilon} \mathrm{e}^{\mathrm{i}\omega}. \quad (61)$$

The magnitude $|K|$ relates to the energy release rate (60) through the general relation (50). The angle ω depends on elastic mismatch between

the film and the substrate, ranging between 40° to 60° if the mismatch is not excessive, as tabulated in bib120 Suo and Hutchinson (1990). A comparison of (61) and (51) gives the mode angle

$$\psi = \omega + \varepsilon \ln (l/h). \tag{62}$$

For representative values, $\varepsilon = -0.05$, $l = 1$ nm, and $h = 1$ μm, the additional angle is $\varepsilon \ln (l/h) = 20°$.

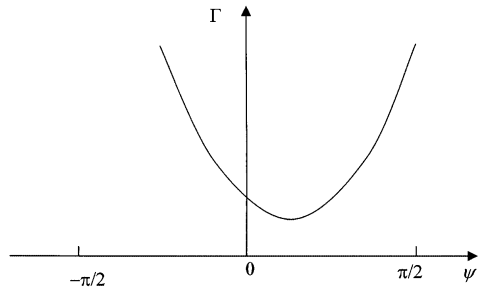

Figure 17 A schematic of $\Gamma(\psi)$.

8.7.3.3 Measuring Interfacial Fracture Energy

SX0360 When a debond crack extends on a bimaterial interface, mixed mode conditions usually prevail. The fracture energy is a function of the mode angle, $\Gamma(\psi)$. The crack extends when the energy release rate reaches the fracture energy: $G = \Gamma(\psi)$. Due to elastic mismatch in the two materials, one should specify the length l in defining the mode angle ψ. The curve $\Gamma(\psi)$ has been measured for a few interface (e.g., bib19 Cao and Evans, 1989; bib133 Wang and Suo, 1990; bib80 Liechti and Chai, 1991). Figure 17 sketches the trend of the $\Gamma(\psi)$ curve. The fracture energy tends to increase as mode angle approaches $\pm\pi/2$. The energy cost for debond varies with the relative proportion of opening and shearing modes, because, e.g., a large amount of shear may promote more inelastic deformation in the constituent materials, or promote near-tip sliding against roughness if the interface is not perfectly flat. The curve $\Gamma(\psi)$ need not be symmetric with respect to $\psi = 0$, because the two materials on either side of the interface are dissimilar, breaking the symmetry between $\psi < 0$ and $\psi > 0$.

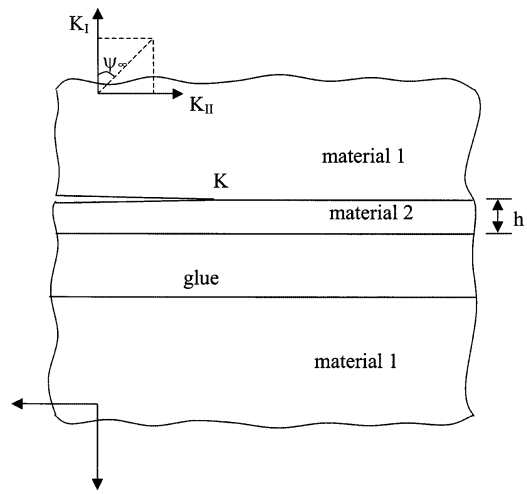

Figure 18 A thin layer of material 2 is sandwiched between two substrates of material 1, using a glue layer. A crack is on one of the interfaces. Near the crack tip, the stress field for the interfacial crack prevails. Far away from the crack, the stress field for a crack in the homogeneous material prevails.

SX0365 Many test configurations for measuring interfacial fracture energy exist. (See reviews by bib61 Hutchinson and Suo (1991), bib31 Evans and Hutchinson (1995), and bib132 Volinsky *et al.* (2002).) For example, the process of a tensile film debonding from a substrate is a means to determine the interfacial fracture energy. To ensure that the crack is in the steady state, one should introduce an initial debond crack of length several times the film thickness (bib139 Yu *et al.*, 2001). The energy release rate (60) depends on both the film stress and the film thickness. One may change the film stress by varying the temperature, or by applying a mechanical load such as pulling the substrate. One may change the film thickness during deposition. The combination of the stress and the thickness that cause the debond crack to grow gives the fracture energy according to (60). It is often more convenient to deposit a layer of a different material to increase the energy release rate. For example, Cr has been used as an overlayer for its high residual stress (bib8 Bagchi *et al.*, 1994). Thick epoxy overlayers have also been used (bib108 Shaffer *et al.*, 1996). When an overlayer is used, one should obtain a different energy release rate expression, and introduce an initial debond crack of length several times of the combined thickness of the film and the overlayer.

SX0370 A class of test methods has been particularly versatile for thin film structures (Figure 18). Suppose one needs to measure the interfacial fracture energy of a thin film of material 1, and a substrate of material 2. One can sandwich the thin film between two substrates of material 1. One may use a layer of adhesive, such as epoxy, to glue the bare substrate to the one covered with the film. The substrates are much thicker than the film and the adhesive, so that the whole specimen is easy to load. The interfacial fracture energy can be measured if

the crack runs on the desired interface. There are several advantages of methods of this kind. First, the methods are applicable for thin films of any thickness, and can even measure the interfacial energy between two thin films, when they are both sandwiched. Second, because the film is still bonded to one substrate in the crack wake, the residual stress in the film is unrelieved, and therefore does not contribute to the energy release rate. Third, the experimental data are relatively easy to interpret, as explained below.

SX0375 Let us return to Figure 18. Because the substrates are much thicker than the films, the stress field in the substrate, far away from the films, is unaffected by the presence of the films, and is the same as that around a crack in a homogeneous body, given in the form (39). The load on the substrate can be represented by the two stress intensity factors K_I and K_{II} for a crack in a homogenous body. Near the crack tip, the stress field is that of an interfacial crack (47), characterized by the complex stress intensity factor K. The energy release rate is related to both the far field and the near-tip field, namely,

$$G = \frac{1}{\bar{E}_1}(K_I^2 + K_{II}^2) = \frac{1}{2}\left(\frac{1}{\bar{E}_1} + \frac{1}{\bar{E}_2}\right)\frac{|K|^2}{\cosh^2(\pi\varepsilon)}. \qquad (63)$$

The energy release rate can be calculated from the homogeneous specimen, neglecting the thin films.

SX0380 The mode angle, however, has to be determined by solving the boundary value problem that includes the thin films. Let ψ_∞ be the mode angle of the remote load, namely, $\tan\psi_\infty = K_{II}/K_I$. The local mode angle ψ is defined by (51) using an arbitrary length l. The local mode angle relates to the remote mode angle as

$$\psi = \psi_\infty + \omega + \varepsilon \ln(l/h), \qquad (64)$$

where h is the thickness of one of the films, and ω is an angle that depends on the elastic properties of the films and the substrates, as well as the ratios between various films. bib119 Suo and Hutchinson (1989) solved the case of a single film between two substrates, and found that ω is less than 10° provided the elastic mismatch is not too large. It is rather cumbersome to keep track of the local mode angle, especially when several films are sandwiched, and when some of them deform plastically. A common practice has been to specify the mode angle for the sandwich specimens by the remote value ψ_∞.

SX0385 As an example, Figure 19 illustrates a four-point bend specimen. The method was introduced by bib20 Charalambides *et al.* (1989) and bib19 Cao and Evans (1989) to determine interfacial fracture energy, and developed by bib25 Dauskardt *et al.* (1998) for thin film structures relevant for interconnects. The experimental procedure is as follows. Use two silicon wafers to sandwich films of interest. Notch the top wafer to within a few μm of the sandwiched films with a diamond wafering blade. Place the sample in a four-point bend fixture. Record load as a function of displacement, and observe the crack propagation in an optical microscope. At a certain load, a crack initiates from the notch root, approaches the interface, and then bifurcates into two cracks to propagate on the interface. When the interface cracks are long compared to the substrate thickness, the load–displacement curve exhibits a plateau—that is, the crack reaches a steady state, in which the energy release rate is independent of the crack length.

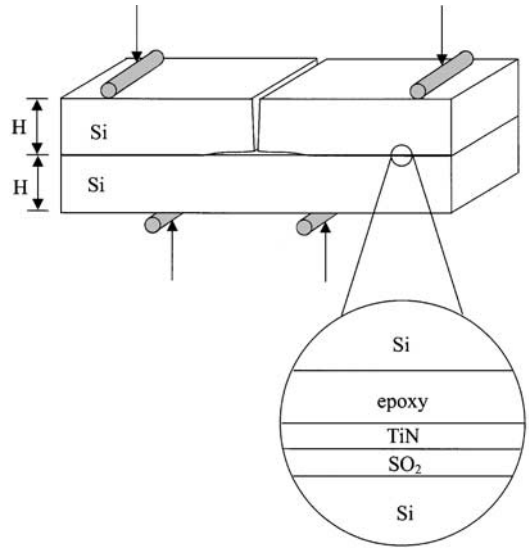

Figure 19 Four-point bend configuration. Thin films of interest are sandwiched between two silicon substrates. On bending, crack runs on one of the interfaces.

SX0390 At the steady state, both the energy release rate and the mode angle are obtained analytically. As shown in Figure 20, the four-point bend configuration is the superposition of two other configurations, one being pure mode I, and the other being pure mode II. The energy release rates for the two configurations can be obtained from elementary considerations. Consequently, the energy release rate for the four-point bend specimen is

$$G = \frac{21}{4}\frac{M^2}{\bar{E}H^3}, \qquad (65)$$

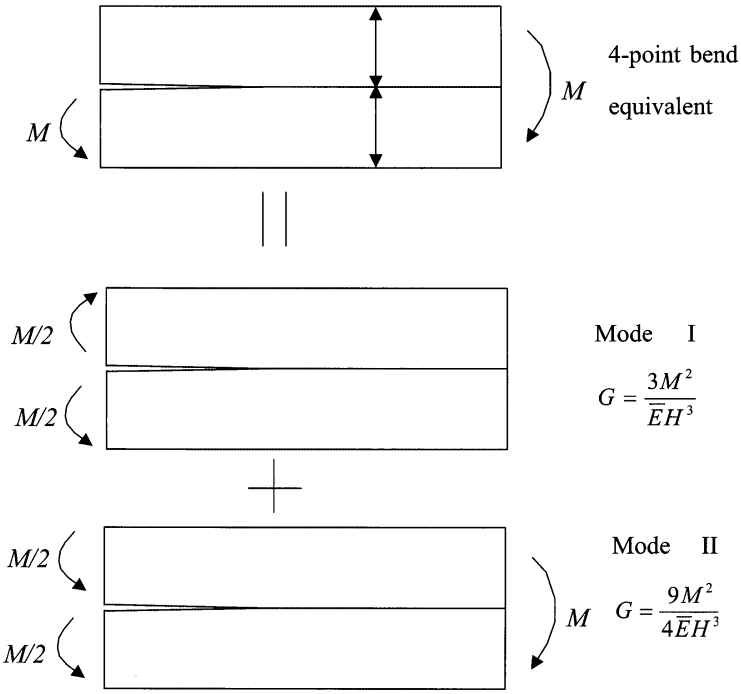

Figure 20 The four-bend configuration is the superposition of two other configurations, one being pure mode I, and the other being pure mode II.

where M is the moment per substrate unit width, H the thickness of each substrate, and $\bar{E}$ the plane-strain modulus of the substrates. The mode angle for the four-point bend specimen is

$$\psi_\infty = \tan^{-1}(\sqrt{3/2}) \approx 41^\circ. \tag{66}$$

Once the plateau load is measured experimentally, (65) is used to calculate the fracture energy Γ for the mode angle 41°.

SX0395 Also commonly used is the double-cantilever beam specimen (bib97 Oh *et al.*, 1987; bib67 Kook and Dauskardt, 2002). The energy release rate for the double-cantilever beam specimen of a homogenous material is found in handbooks, given by

$$G = 12\frac{(Pa)^2}{H^3\bar{E}}\left(1 + 0.677\frac{H}{a}\right)^2, \tag{67}$$

where a is the crack length, H the thickness of each beam, P the force per beam width, and $\bar{E}$ the plane-strain elastic modulus. The specimen is under the mode I condition, $\psi_\infty = 0^\circ$. As discussed before, a crack in a homogenous double-cantilever beam specimen tends to curve away from the mid-plane (Figure 14). By contrast, when films are sandwiched between the two beams, creating a weak interface, the crack will propagate along the interface. In the experiment of bib97 Oh *et al.* (1987), 750 nm copper films were evaporated onto two glass substrates (of size 75 mm × 25 mm × 2 mm). To confine crack propagation to one glass–copper interface, a layer of 10–20 nm chromium was evaporated onto one substrate prior to depositing the copper film. The chromium layer promoted adhesion. The copper films from the two substrates were then pressure diffusion bonded. To load the sample, aluminum arms were attached by epoxy to the ends of the specimen. The thin specimen led to high enough specimen compliance that the crack was easily arrested, permitting multiple testing of one specimen. The experimentally measured load to cause the crack to propagate rapidly gave the interfacial fracture energy according to (68). The crack on the glass–copper interface displayed subcritical growth rates spanning from $\sim 10^{-8}$ to $10^{-3}\,\mathrm{m\,s^{-1}}$, in the range of the energy release rates from ~ 0.5 to $2.0\,\mathrm{J\,m^{-2}}$.

The measurements of interfacial fracture SX0400 energy provide a tool for process control (Dr. Q. Ma, Intel Corporation, private communication). Many factors during the interconnect AU:4 fabrication process can affect adhesion. Because debonding usually occurs after a interconnect structure is fabricated, when stresses arise from, e.g., thermal expansion mismatch. After a debond is identified, one has to modify the processing conditions, fabricate the interconnect structure again, and examine if the

new structure has the debond. The iteration is time consuming. Alternatively, without fabricating the whole interconnect structure, one can measure the interfacial fracture energy for the interface at question under various fabrication conditions, and then select the condition that gives an adequate interfacial fracture energy.

SX0405 The measurements of interfacial fracture energy also provide a tool to select materials to promote adhesion. When copper was introduced into the interconnect structure in late 1990s, new barrier layers were required to prevent copper diffusion into dielectrics, and to provide adhesion of copper to the dielectrics. The sandwiched four-point bend specimens were used to measure the interfacial fracture energy of the thin film structures with Ta and TaN as barrier layers (bib72 Lane *et al.*, 2000), and thereby to study the effects of interfacial chemistry, copper layer thickness, and dielectric type on adhesion. Subsequently, numerous materials of low dielectric constant have been developed to compete to be a replacement for silica in the interconnect structure. To compare these materials, a commonly accepted method is desired to measure the interfacial fracture energy. bib102 Rim *et al.* (2002) have evaluated adhesion of a carbon-doped oxide in thin film structures.

SX0410 Interfacial cracks are often susceptible to subcritical growth under static or cyclic load. Environment strongly affects the growth rate. While the implications of subcritical debond growth for long-term reliability of the interconnect structure have not been fully understood, the fracture specimens discussed above have been used to study subcritical debond growth (bib67 Kook and Dauskardt, 2002; bib112 Snodgrass *et al.*, 2002).

8.7.3.4 Effects of Plasticity

SX0415 The above discussions are confined in the linear elastic fracture mechanics (LEFM). One of the main requirements of the LEFM is that the inelastic zone around the crack tip must be much smaller than the feature size, in our case, the film thickness. The inelastic deformation within the small zone is accounted for by the fracture energy. In computing the energy release rate, the structure is taken to be elastic. When the inelastic zone is large compared to the film thickness, however, we must consider the inelastic deformation more explicitly. The following examples illustrate roles played by plasticity.

SX0420 As a first example, consider two films, one brittle and the other ductile, sandwiched between two silicon wafers (Figure 21). The crack extends on the interface between one wafer and the brittle film by a bond-breaking process. So long as the brittle film thickness is large compared to the atomic spacing, the bond-breaking process is unaffected by the presence of the ductile film. Consequently, the fracture energy Γ is well defined for the interface between the wafer and the brittle film. As the crack extends, a material particle in the ductile layer deforms plastically, and then unloads elastically. This hysteresis can be accounted for by the continuum theory of plasticity. In the silicon wafers, far away from the films, the stress state is the same as that for a crack in a homogeneous elastic material, with the energy release rate G representing the amplitude of the external load. An elastic–plastic boundary value problem relates the external load G to the bond-breaking energy Γ and the plastic deformation properties (bib121 Suo *et al.*, 1993; bib72 Lane *et al.*, 2000). The hysteresis costs energy. The energy release rate

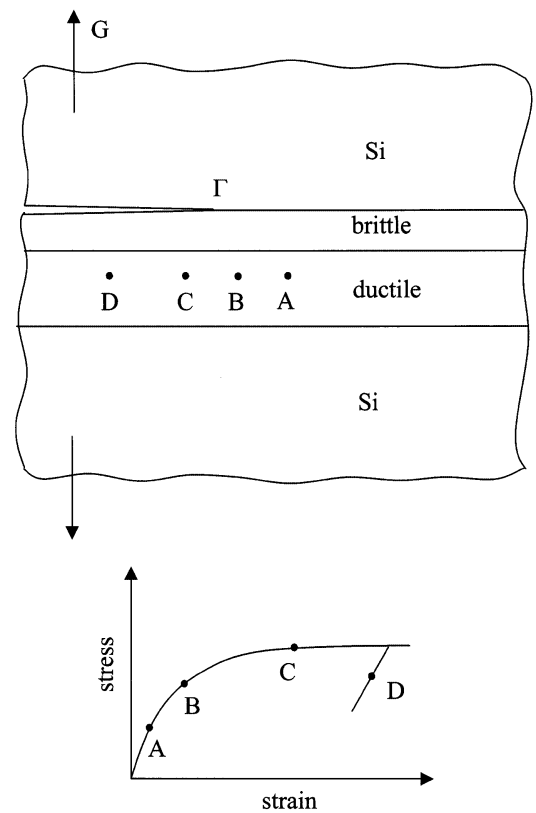

Figure 21 A brittle film and a ductile film are sandwiched between two silicon wafers. The crack runs on the interface between one silicon wafer and the brittle film. As the crack tip passes by, a material particle in the ductile layer undergoes a history of deformation: elastic (A), yielding (B), plastic straining (C), and elastic unloading (D).

to maintain steady-state crack growth, G_{ss}, exceeds the interfacial fracture energy Γ. The ratio G_{ss}/Γ depends on the thicknesses of the two films, and on the yield strength of the ductile layer. When the ductile layer is absent, $G_{ss}/\Gamma = 1$, so that Γ can be determined experimentally by the external load. By gradually increasing the ductile layer thickness, the effect of plastic deformation on G_{ss} can be both measured and calculated. One may study deformation properties of the ductile layer this way.

SX0425 A second example involves a crack on a metal–ceramic interface (Figure 22). The metal deforms plastically, which may be described by the continuum plasticity theory (bib60 Hutchinson and Evans, 2000), or by dislocation dynamics (bib94 Needleman and Van der Giessen, 2001). Two classes of failure modes are envisioned. The crack may extend by decohesion (Figure 22(a)). The bond-breaking process may be characterized by a traction-displacement law. The crack tip is no longer a structureless point, but spreads out into a cohesive zone. The deformation hysteresis in the metal costs energy, as discussed above.

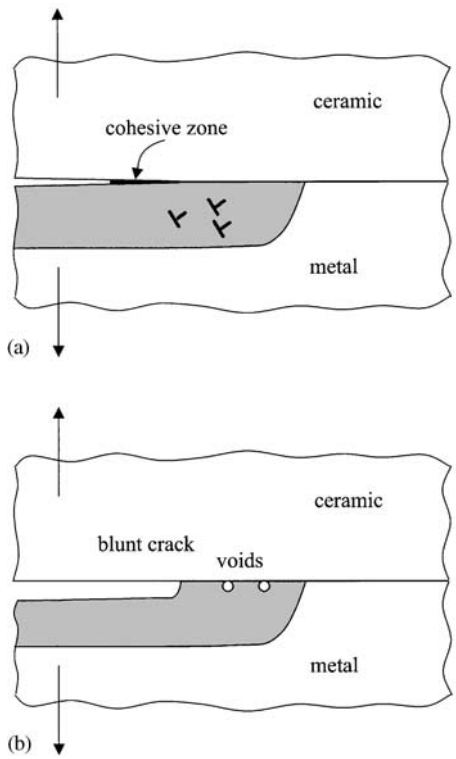

Figure 22 A crack on a metal–ceramic interface. The plastic deformation may be described by continuum plasticity theory or by discrete dislocation dynamics. (a) Crack grows by a bond-breaking process. (b) Crack tip blunts, and voids open ahead of the crack tip.

Alternatively, the crack may extend by linking voids (Figure 22(b)). As the load increases and the crack tip blunts, the peak stress remains constant (a few times the yield strength), but the strain keeps increasing (bib111 Shih *et al.*, 1991). Voids open ahead of the crack tip, and link together to extend the crack. The behavior is similar to ductile fracture of bulk metals.

As a third example, consider a thin metal SX0430 film sandwiched between two elastic substrates (Figure 23). A debond crack preexists on one of the interfaces. The substrates are loaded to open the crack. Let h be the film thickness, and r_p be the plastic zone size upon crack propagation. When $h \gg r_p$, the substrates place no additional constraint on fracture, and the behavior is the same as described in Figure 22. When $h < r_p$, however, the substrates constrain the plastic flow in the film. As the load increases and the crack tip blunts, the level of the peak stress in the metal increases, and the location of the peak stress is several times the film thickness ahead of the crack tip (bib130 Varias *et al.*, 1991). The high stress activates flaws ahead of the crack tip into new debond areas, which link back to the main crack (bib100 Reimanis *et al.*, 1991). When the film thickness is very small, the dislocations emitted from the crack tip pile up at the substrate–film interfaces (Figure 24). As the load increases and the crack tip blunts, more dislocations pile up and the stress at the crack tip can increase up to the theoretical strength (bib49 Hsia *et al.*, 1994; bib86 Mao and Evans,

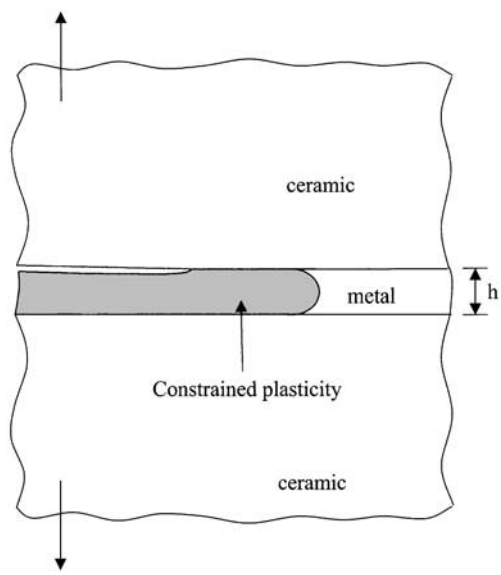

Figure 23 A thin metal film is sandwiched between two ceramic plates. The plastic deformation in the metal is constrained, leading to high triaxial stresses several film thicknesses ahead of the crack tip.

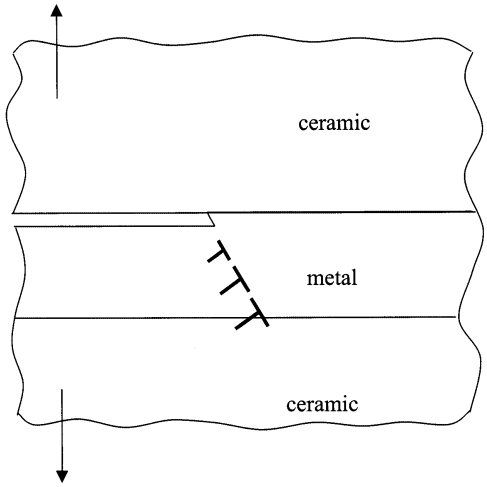

Figure 24 A very thin metal film is sandwiched between two ceramic plates. Dislocations emitted from the crack tip pile up at the interface. As the applied load increases, the stress at the blunted crack tip can be very high, leading to cleavage.

1997). Even FCC metals can fracture by cleavage this way.

8.7.4 RATCHETING

8.7.4.1 Temperature Cycling as a Qualification Test

SX0435 Temperature cycling has long been used as a test to qualify devices (bib113 Suhir, 2002). After being cycled between two temperatures, say –55°C to 125°C for 1,000 times, a device is tested for its functions, and then sectioned and examined in microscopes for failure modes (e.g., distortion and cracking). If a failure mode is found, one makes a new device by modifying either processing parameters, or geometries, or materials. The new device is temperature cycled again, followed by the microscopy examination. The iterations do not guarantee quick convergence, as the modifications made to avert one failure mode may cause another. These make-and-break iterations are extremely time consuming, and are a bottleneck for innovation. Consequently, it is urgent to understand various failure modes caused by temperature cycling.

SX0440 Figures 25(a) and (b) are a photo of a flip-chip package and a schematic of its cross-section. An organic substrate is bonded to a silicon die on the face that contains transistors. The solder bumps connect the interconnects on the die to the printed circuits on the substrate. Layers of polymers (epoxy underfill and polyimide) lie between the substrate and the die. Figure 25(c) illustrates part of the interconnect structure, with an aluminum film on silica. The feature size in the interconnect structure is much smaller than the overall package. Before the die is bonded to the substrate, a silicon nitride (SiN) film is deposited over the interconnect structure, covering both the metal and the dielectric, serving as a barrier to environmental molecules.

Observed failure modes in such a package SX0445
caused by temperature cycling include

- die–polymer or polymer–substrate debonding (bib137 Yan and Agarwal, 1998; bib39 Gurumurthy *et al.*, 1998),
- solder bump detachment (bib73 Lau *et al.*, 1998),
- silicon die cracking (bib40 Han, 2001; bib91 Michaelides and Sitaraman, 1999),
- SiN film cracking (bib57 bib56 Huang *et al.*, 2000, 2002; bib28 Edwards *et al.*, 1987; bib2 Alpern *et al.*, 1994; bib36 Gee *et al.*, 1995), and
- metal film crawling (bib55 Huang *et al.*, 2001; bib2 Alpern *et al.*, 1994; bib62 Isagawa *et al.*, 1980; bib123 Thomas, 1985).

The last two failure modes in the above list SX0450
occur in the interconnect structure, and provide the focus of the following discussion. Figure 26 shows the micrographs taken after temperature cycles. Figure 26(a) is a plan view of the die surface near a corner of a test structure. The structure has many aluminum pads. Cracks develop in the SiN film over some of the aluminum pads. Figure 26(b) shows a patterned aluminum pad on silica, with a SiN film covering both aluminum and silica. Cracks form in SiN over aluminum, but not in SiN over silica. Figure 26(c) shows a cross-section of a crack in the SiN passivation film. Notice that the crack opens substantially. Figure 26(d) is a cross-section of two aluminum pads, which shift and break the SiN film. The main experimental observations are summarized as follows:

- Cracking occurs in the SiN film at the die corners.
- The aluminum pads crawl toward the die center. The displacement reduces for pads away from the die corners.
- Cracking occurs after temperature cycles, and becomes more extensive as the number of cycles increases.
- Cracking occurs in the SiN film over the metal films, but not in the SiN film over silica.
- Cracking is more likely when the metal films are wide and the SiN film is thin.

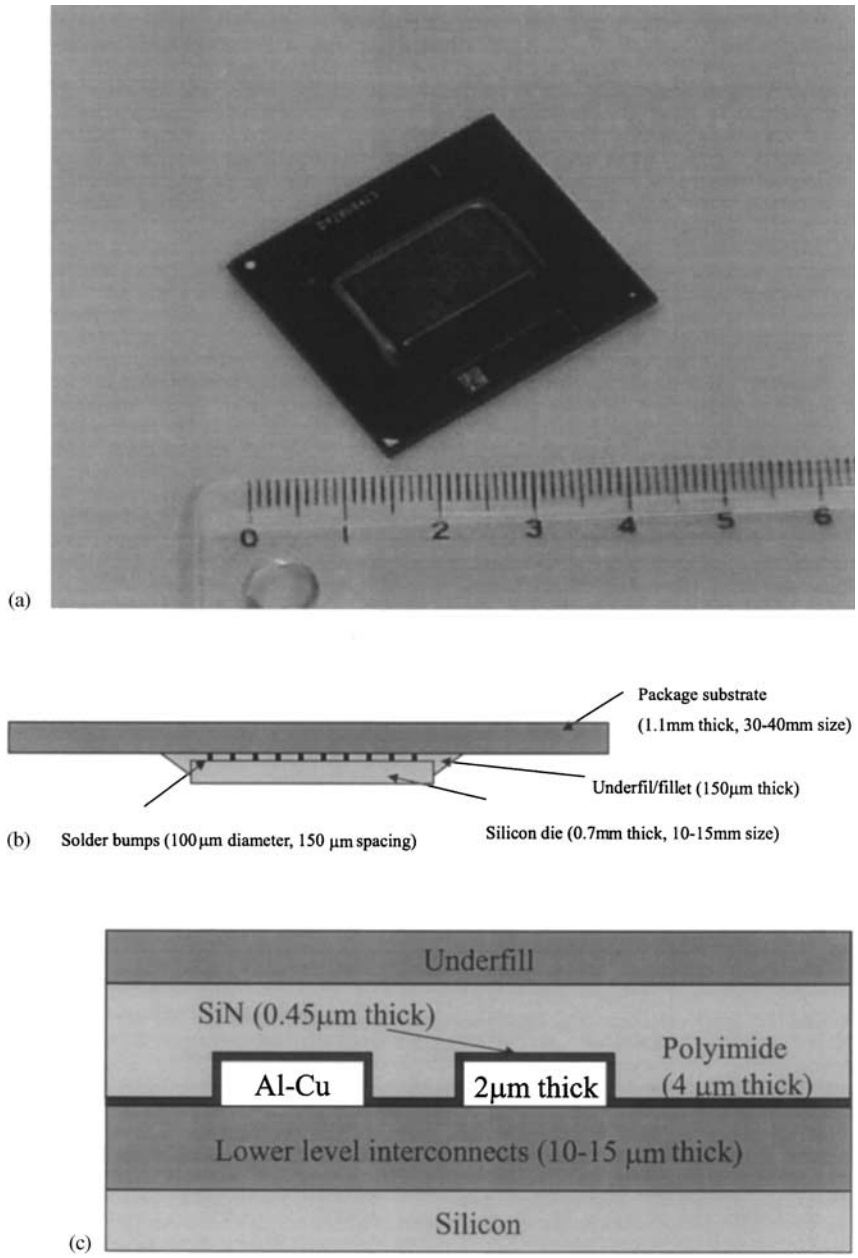

Figure 25 (a) A photo of a flip-chip package. (b) A schematic of cross-section of the package. (c) Magnified view of the interconnect structure.

SX0455 Because the organic substrate has a larger thermal expansion coefficient than the silicon die, upon cooling from the curing temperature, a shear stress develops on the silicon die. The shear stress concentrates at the die corners, and decreases away from the corners. As illustrated in Figure 27, the entire range of cyclic temperature is below the epoxy curing temperature, so that the shear stress at the die corners point toward the die center during cycling. It is not surprising that failures occur at the die corners, and that aluminum pads crawl toward the die center.

Two questions, however, are inexplicable SX0460 from these simple considerations. Why should crawling and cracking occur at all? The shear stress on the die is transmitted through the polymers, and is limited by the yield strength of the polymers, say 100 MPa. The yield strength of the metal film exceeds 100 MPa (bib95 Nix, 1989). The fracture strength of the SiN thin film is on the order 1 GPa (bib85 Ma *et al.*, 1998). Why should cracks occur after many

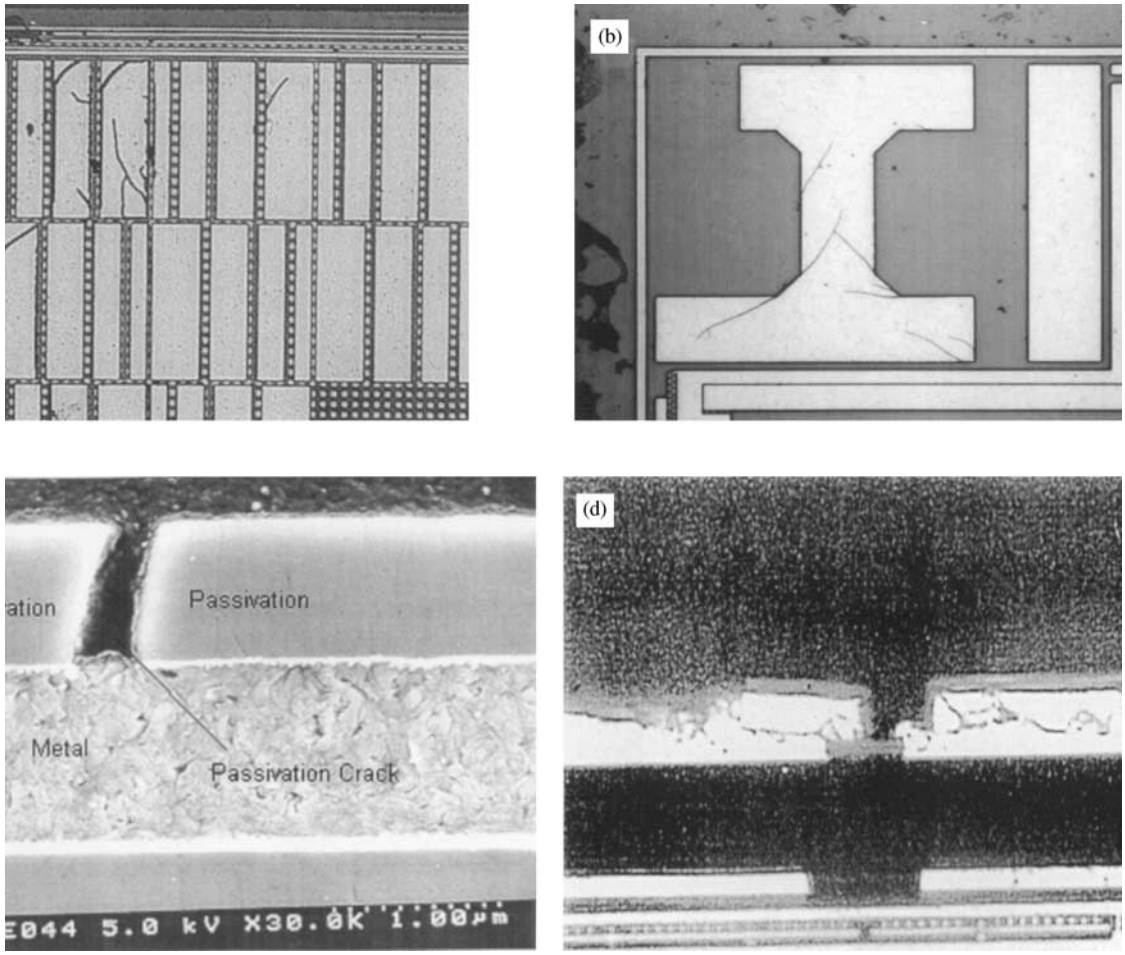

Figure 26 (a) The plan view of the surface of a die, near a die corner (source bib57 Huang *et al.*, 2000). (b) Patterned aluminum pads. Cracks form in SiN over aluminum, but not in SiN over silica (source bib56 Huang *et al.*, 2002). (c) A cross-section shows a crack in SiN (courtesy of Dr. J. B. Han). (d) A cross-section shows shifted aluminum pads (source bib55 Huang *et al.*, 2001).

temperature cycles? Unlike ductile materials, SiN does not have an intrinsic fatigue mechanism.

8.7.4.2 Ratcheting toward a Steady State

SX0465 bib57 Huang *et al.* (2000) have recently discovered a mechanism that answers these questions. As mentioned before, the silicon die and the packaging substrate have different thermal expansion coefficients, inducing shear stresses, τ_0, at the die corners upon curing (Figure 28). When the temperature cycles in a range below the curing temperature, the direction of the shear stress τ_0 is biased toward the die center. For simplicity, τ_0 is taken to be constant, set by the yield strength of the polymer, independent of position and temperature. The shear stress τ_0 is partly sustained by a membrane stress σ in the passivation film, and

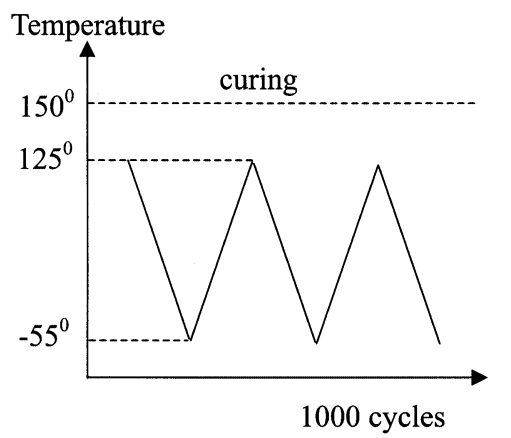

Figure 27 Temperature as a function of time. The cyclic temperature range is below the curing temperature of epoxy.

partly transmitted to the metal film underneath as a shear stress in the metal, τ_m. The metal film also has a large thermal expansion mismatch with silicon and silica beneath, so that the metal film plastically yields in every temperature cycle. Because the temperature change by itself causes the metal to yield, even a very small shear stress in the metal, τ_m, will cause the metal to deform in shear plastically. The in-plane plastic strain in the metal film is constrained by the elastic substrate. Consequently, the amount of plastic shear strain per cycle in the metal is small, as will become evident later when we look at the model closely. The increment of the shear strain is in the same direction as the shear stress on the passivation film, τ_0, pointing toward the center of the die. Incrementally, the shear stress in the metal film, τ_m, relaxes, and the membrane stress σ in the overlaying SiN film builds up. It is this evolving stress state that cracks the SiN film after some cycles.

Figure 29 illustrates the evolution of the stress field as the temperature cycles. In the first temperature cycle, the shear stress τ_0 from the organic substrate is transmitted into the metal film underneath the SiN film, so that the stress in the SiN film is low, comparable to τ_0 (Figure 29(a)). As the temperature cycles, the shear stress in the metal pad decreases, and the stress in SiN accumulates. After many cycles, a steady state is reached, in which the metal no longer has any shear stress (Figure 29(b)). The shear stress τ_0 from the organic substrate is SX0470

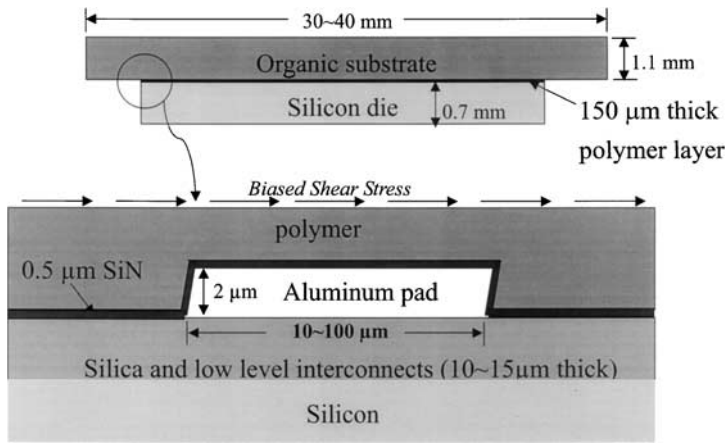

Figure 28 At a corner of the die, the organic substrate applies a shear stress on the surface of the die. The shear stress points to the die center. The thermal expansion misfit between aluminum and silicon causes the aluminum pad to yield repeatedly during temperature cycles. Directed by the biased shear stress, the aluminum pad shears by a small amount each temperature cycle. After many cycles, the accumulated shear significantly distorts the SiN film, leading to cracking.

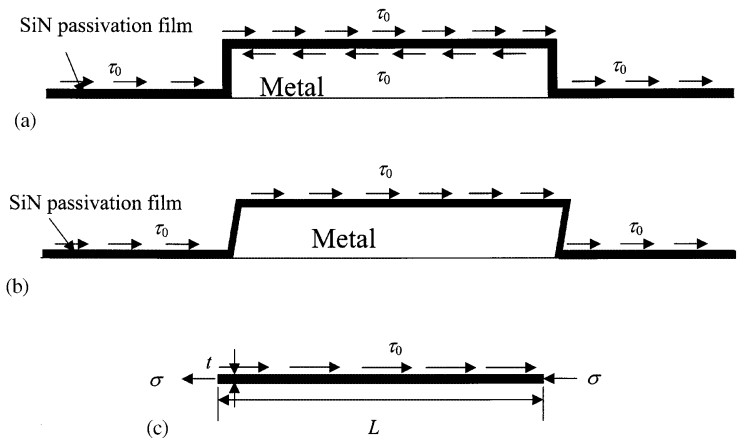

Figure 29 The evolving stress state in the SiN film and the aluminum pad. (a) Before temperature cycling, the shear stress due to the organic substrate is transmitted to the aluminum pad, and the structure does not distort much. (b) After many temperature cycles, the shear stress in aluminum vanishes, and the structure distorts greatly. (c) The shear stress from the organic substrate is balanced by the membrane stress in SiN.

now all sustained by the membrane stress in the SiN film. Figure 29(c) shows the free-body diagram of the SiN film. Denote by σ_A the magnitude of the membrane stress in SiN at the two ends, tensile on the left and compressive on the right. As discussed above, the film has the traction τ_0 on the top face from the organic substrate, but no traction on the bottom face from the metal pad. Force balance requires that

$$\sigma_A = \frac{\tau_0 L}{2t}, \tag{68}$$

where t is the thickness of the SiN film and L the length of the aluminum pad. Although the shear stress τ_0 is small, the length ratio L/t is typically very large. Consequently, the stress in the SiN film can build to a high level to cause cracking. The magnitude of the stress in the SiN film increases with the shear stress at the die corner and the width of the aluminum pad, but is inversely proportional to the SiN film thickness. These are consistent with the experimental observations. In the steady state, the membrane stress in SiN varies linearly with the position, given by

$$\sigma(x) = -2\sigma_A x/L, \tag{69}$$

where x is the distance from the center of the aluminum pad.

SX0475 Finite element calculation of a plane-strain model has confirmed the main features of the model (bib57 Huang *et al.*, 2000). As the temperature cycles, the shear stress in the metal reduces, and the membrane stress in the SiN film increases. In the steady state, the shear stress in the metal vanishes, the in-plane stress in the metal cycles with the temperature, and the membrane stress in the SiN film attains the distribution (69).

SX0480 The deformation in the same direction, guided by a bias and facilitated by a cyclic load (temperature change in this case), is known as ratcheting deformation (bib17 Bree, 1967; bib63 Jansson and Leckie, 1992; bib115 Suresh, 1998). In addition to the example discussed here, several other examples of ratcheting deformation in thin film structures have been discovered (bib43 He *et al.*, 2000; bib10 Begley and Evans, 2001; bib65 Karlsson and Evans, 2001).

SX0485 To avert SiN cracking, an industrial practice is to change the shape and the size of the metal pad. For example, slots are made in the metal pads, so that the SiN film is in contact with the silica in the slots (Figure 30). To aid design, we would like to do calculations over thousands of temperature cycles, for three-dimensional structures, and for many geometrical designs.

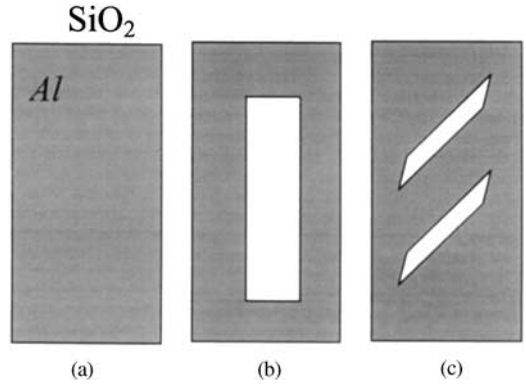

Figure 30 (a) An aluminum pad on silica surface. (b) and (c) The aluminum pads are slotted. In each case, a SiN film covers both aluminum and silica.

However, because of the nonlinear material behavior, each temperature rise or drop has to be divided into many small steps in the finite element calculation. A crude division would lead to numerical ratcheting, i.e., the apparent ratcheting deformation due to accumulated numerical errors for structures that should not suffer ratcheting at all. Consequently, direct finite element calculation would require too much time to be practical.

SX0490 In the steady state, the shear stress in the metal pad vanishes, and the SiN film is in a state of plane-stress elastic deformation. At the edges of the metal pad, the displacement of the SiN film is constrained by the silica, and is set to be zero. The shear stress from the organic substrate is distributed over the face of the SiN film, acting like a body force. Such a linear elastic plane-stress problem can be solved rapidly by the finite element method for any pad geometry. As an illustration, Figure 31(a) shows the normalized maximum principal stress distribution at the steady state by applying the uniform shear stress τ_0 in the direction of -45° from the x-axis. The membrane stresses in the passivation film scale with $\tau_0 L/h_p$, where L is the width of the metal film. The maximum principal tensile stress is very high near the left edge and the left upper corner, where cracking always happens. Figure 31(b) shows a slotted structure, where the membrane stress in the passivation film is greatly reduced.

SX0495 The steady state is a robust concept: it does not depend on the detailed mechanical property of the metal, and the stress field is easy to calculate. The steady state is applicable even if the metal creeps, or the passivation film and the metal debond. Once the stress field in the steady state is calculated, one can ascertain if the SiN film is safe from cracking. If SiN can

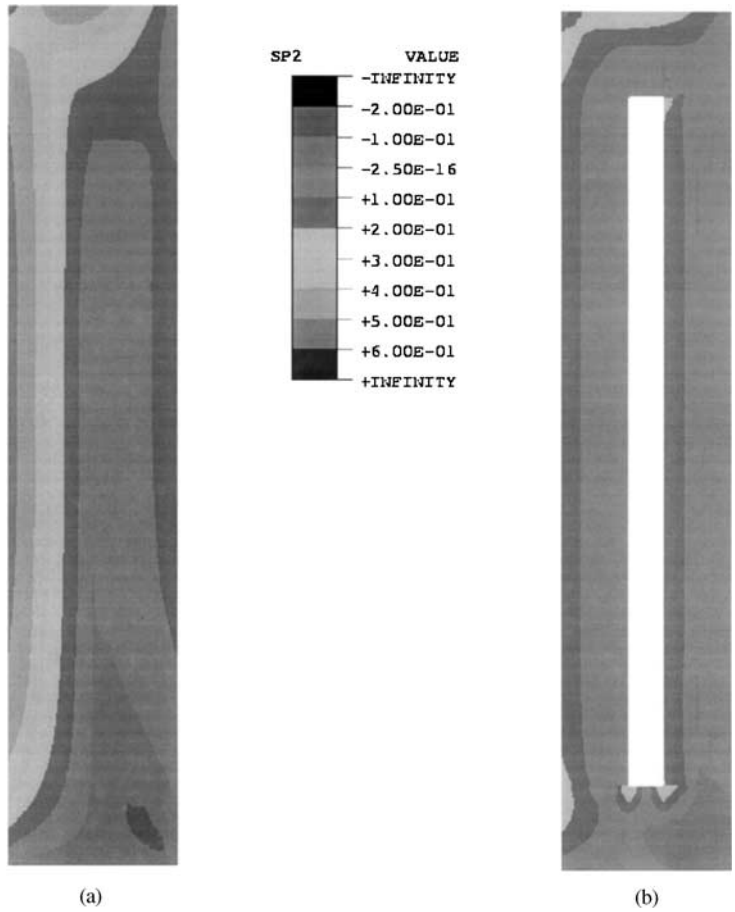

Figure 31 The normalized maximum principal stress distribution, $(\sigma_{\max} h_p)/(\tau_0 L)$. The length L is taken to be the width of the metal film. (a) A rectangular aluminum pad and (b) a slotted aluminum pad (source bib57 Huang *et al*., 2002).

sustain the stress in the steady state, then the design is immortal: it can sustain any number of temperature cycles without cracking.

SX0500 This steady state approach leaves two issues unresolved: the condition under which the metal film undergoes ratcheting deformation, and the number of cycles needed to approach the steady state. We study these issues in the following sections. To gain insight, we examine idealized structures and material behaviors.

8.7.4.3 Shakedown vs Cyclic Plastic Deformation

SX0505 First consider a blanket metal film bonded to a substrate. The film has thermal expansion coefficient α_m, Young's modulus E_m, and Poisson's ratio ν_m. We model the film as a nonhardening solid, assuming that the yield strength Y is independent of temperature, and is the same under tension and compression. Subject to a temperature change, the film is under biaxial stress σ. The substrate, being much thicker than the film, has negligible stress, so that only its thermal expansion coefficient α_s enters the consideration. The film and the substrate are well bonded, matching the net strain at all time.

When the temperature changes by dT, the SX0510 film and the substrate acquire thermal strains $\alpha_m dT$ and $\alpha_s dT$, respectively. This mismatch is compensated in different ways, depending on whether the film is elastic or plastic. If the film is elastic, $|\sigma| < Y$, the mismatch in the thermal strains is compensated by the change in the elastic strain in the film. The latter gives rise to the change in the film stress:

$$d\sigma = -\frac{E_m(\alpha_m - \alpha_s)}{1 - \nu_m} dT. \tag{70}$$

If the film yields, however, the stress in the film is fixed at the yield strength, either in tension $\sigma = +Y$ or in compression $\sigma = -Y$, so that the elastic strain in the film no longer changes with the temperature. Consequently, the mismatch in the thermal strains is compensated by the

plastic strain in the film:

$$d\varepsilon^p = -(\alpha_m - \alpha_s)\, dT. \tag{71}$$

SX0515 Figure 32 plots the change in the film stress σ and the plastic strain ε^p when the temperature cycles between T_L and T_H. Let us start at the preset high temperature T_H, with the initial film stress σ_0 anywhere between $-Y$ and $+Y$.

(1) As the temperature drops, the film is elastic, and the film stress changes toward tension according to Equation (70). The plastic strain does not change.

(2) At some temperature T_A, the film yields in tension, and the film stress is fixed at the yield strength, $\sigma = +Y$. As the temperature drops, the plastic strain increases according to (71).

(3) On reaching the preset low temperature T_L, the temperature starts to rise. The film is elastic, and the film stress changes toward compression. The plastic strain does not change.

(4) At some temperature T_B, the film yields in compression, and the film stress is fixed at the yield strength, $\sigma = -Y$. The plastic strain decreases as the temperature rises.

(5) On reaching T_H, the temperature starts to drop again. The film is elastic, and the film stress changes toward tension. The plastic strain does not change. Afterwards, the stress and strain state of the film cycles with the temperature.

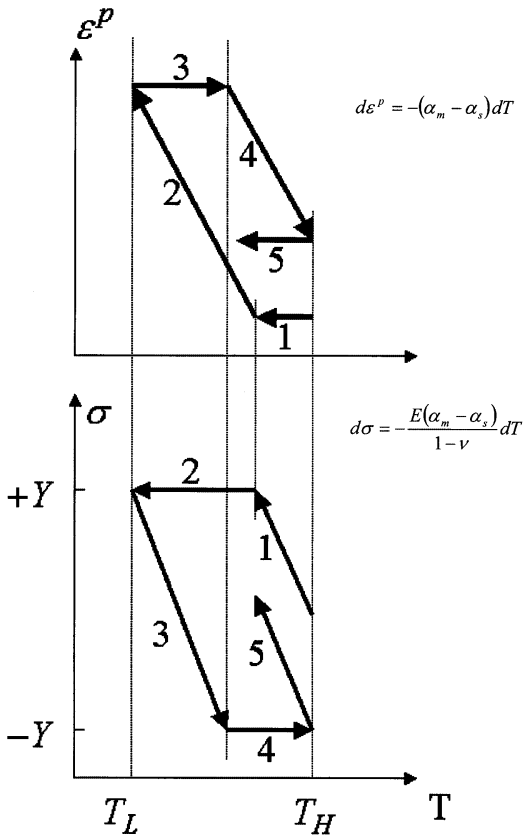

Figure 32 Plastic strain and stress change with the temperature during a thermal cycle of blanket aluminum film on a silicon substrate.

Inspecting Figure 32, we distinguish three SX0520 behaviors. Imagine that T_L is fixed, and T_H is allowed to change. If $T_L > T_A$, the film will be elastic during temperature cycling. If $T_H < T_B$, the film will undergo plastic deformation in the first cycle, but will be elastic in all subsequent cycles. This behavior is referred to as *shakedown*. The film reaches the shakedown condition if

$$\frac{E_m(\alpha_m - \alpha_s)(T_H - T_L)}{(1-\nu_m)Y} < 2. \tag{72}$$

If the inequality (72) is reversed, the film will undergo *cyclic plastic deformation*. During the fabrication of the interconnect structure, the metal film inevitably yields as the temperature drops from the processing temperature. Consequently, plastic yield during the first cycle should not be of any concern, and the elastic and shakedown behaviors are practically indistinguishable. However, as we will see below, the difference between shakedown and cyclic plasticity has a significant consequence. The demarcation (72) between the two regimes, shakedown and cyclic plasticity, is unaffected by the initial film stress.

8.7.4.4 Ratcheting Strain Rate

In the above, the plastic strain cycles because SX0525 the film has to match the net in-plane strain to the substrate. By contrast, the shear strain in the film is not constrained by the substrate, so that it may accumulate under certain conditions. bib55 Huang *et al.* (2001) have calculated the strain rate due to ratcheting. Figure 33(a) illustrates a blanket metal film bonded on a semi-infinite elastic substrate. A shear stress τ_m acts on the surface of the metal film. For the time being, this shear stress is taken to be spatially uniform, and remains constant as the temperature cycles. The stress field in the structure is very simple. The semi-infinite substrate is subject to the same shear stress τ_m, but no other stress components. Let the coordinates in the plane of the film be x_1 and x_2, the coordinate normal to the plane be x_3, and the coordinate x_1 coincide with the direction of the shear stress τ_m. As shown in Figure 33(b), the film is in a uniform stress

state of a combination of a biaxial stress and a shear stress:

$$\sigma_{11} = \sigma_{22} = \sigma_m, \quad \sigma_{13} = \tau_m, \quad \sigma_{23} = \sigma_{12} = 0. \tag{73}$$

The biaxial stress σ_m changes with the temperature. Obviously, the uniform stress states in the substrate and in the film satisfy the equilibrium conditions.

SX0530 To model plastic deformation in the metal film, we adopt the J_2 flow theory (bib44 Hill, 1950). The deviatoric stress tensor, $s_{ij} = \sigma_{ij} - \sigma_{kk}\delta_{ij}/3$, has the components

$$s_{11} = s_{22} = \sigma_m/3, \qquad s_{33} = -2\sigma_m/3, \qquad s_{13} = \tau_m,$$
$$s_{23} = s_{12} = 0. \tag{74}$$

The Mises yield condition, $3s_{ij}\,s_{ij}/2 = Y^2$, is specialized to

$$\sigma_m^2 + 3\tau_m^2 = Y^2. \tag{75}$$

The yield condition is an ellipse on the σ_m–τ_m plane (Figure 33(c)). The metal film is elastic when the stress state is inside the ellipse, and yields when the stress state is on the ellipse. The stress state outside the ellipse is unreachable. When the film yields, for a given τ_m, the biaxial stress can only be at one of the two levels:

$$\sigma_m = \pm\sqrt{Y^2 - 3\tau_m^2}. \tag{76}$$

These two states, tensile and compressive, are indicated in Figure 33(c).

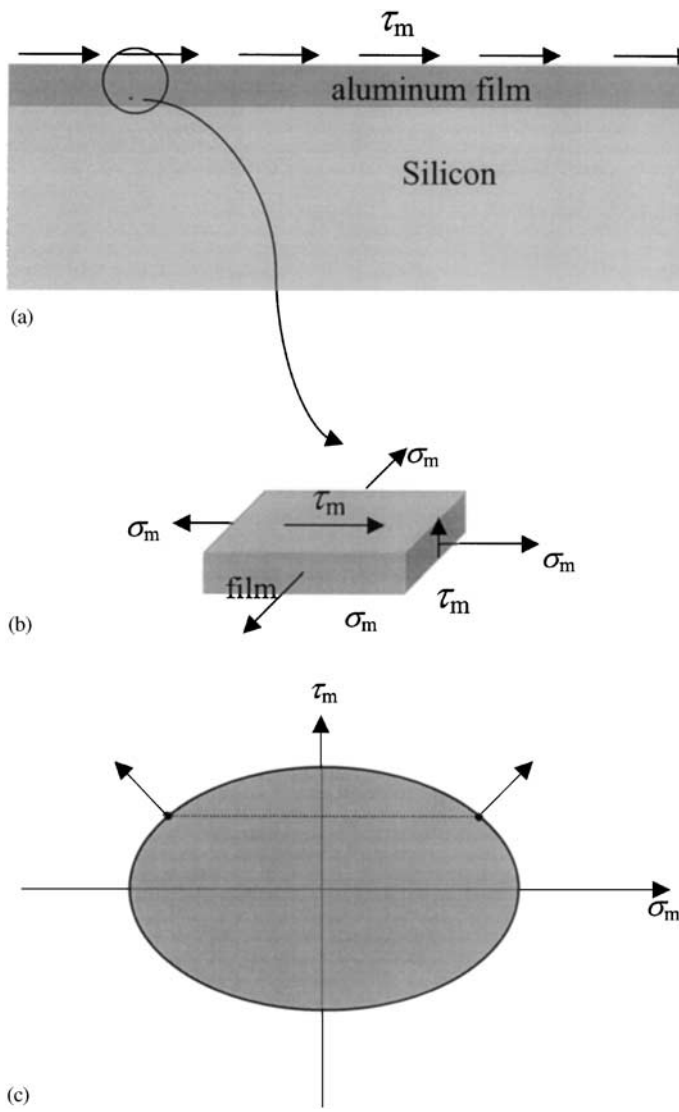

Figure 33 (a) A blanket aluminum film on a silicon substrate. (b) The stress state in the aluminum film consists of biaxial in-plane stresses and a shear stress. (c) The yield condition on the σ_m–τ_m plane.

SX0535 Figure 34 shows a coordinate plane spanned by the normalized shear stress, τ_m/Y, and the normalized temperature range, $E(\alpha_f - \alpha_s)(T_H - T_L)/[(1-\nu)Y]$. The plane is divided into three regimes: plastic collapse, shakedown, and crawling. If $\tau_m/Y \geq 1/\sqrt{3}$, the film plastically deforms under the shear stress alone without the aid of the temperature change, and is in the plastic collapse regime. If $\tau_m/Y < 1/\sqrt{3}$ and the temperature range is small enough, the film may plastically deform during the first temperature cycle, but cycles elastically afterwards. The film is in the shakedown regime. This shakedown condition is represented in Figure 34 by a shaded region below a quarter of an ellipse:

$$\frac{E(\alpha_f - \alpha_s)(T_H - T_L)}{(1-\nu)Y} = 2\sqrt{1 - 3\left(\frac{\tau_m}{Y}\right)^2}. \quad (77)$$

SX0536 The J_2 flow theory dictates that the plastic strain increment tensor be in the same direction as the deviatoric stress tensor, namely, $d\varepsilon_{ij} = s_{ij}^p d\lambda$, where $d\lambda$ is a scalar. Consequently, from Equation (74) we obtain that

$$\frac{d\varepsilon^p}{\sigma_m/3} = \frac{d\gamma^p}{2\tau_m}, \quad (78)$$

where $\gamma^p = 2\varepsilon_{13}^p$ is the plastic shear strain in the film. Equation (78) is the key to the understanding of metal film crawling. Its geometric interpretation is well known: the increment of the plastic strain tensor points in the direction normal to the yield surface (Figure 33(c)). During plastic deformation, $d\varepsilon^p$ has the same sign as the biaxial stress σ_m, and $d\gamma^p$ has the same sign as the shear stress τ_m. When film yields in compression ($\sigma_m < 0$), the plastic in-plane strain decreases, $d\varepsilon^p < 0$. When film yields in tension ($\sigma_m > 0$), the plastic in-plane strain increases, $d\varepsilon^p > 0$. Because the film is bonded to the substrate, for a given temperature increment, $d\varepsilon^p$ is always finite. Consequently, in each cycle, γ^p increases by a finite amount in the direction of τ_m, both when the film is in tension *and* in compression.

SX0545 When the film yields, the plastic in-plane strain changes according to Equation (71). A substitution into (78) gives the increment of the plastic shear strain:

$$d\gamma^p = -\frac{6\tau_m}{\sigma_m}(\alpha_m - \alpha_s)\, dT. \quad (79)$$

When the film plastically deforms in tension, $\sigma_m = +\sqrt{Y^2 - 3\tau_m^2}$ and $dT < 0$. When the film plastically deforms in compression, $\sigma_m = -\sqrt{Y^2 - 3\tau_m^2}$ and $dT > 0$. In either case, the plastic shear strain increment is in the direction of τ_m, namely, $d\gamma^p > 0$, giving rise to crawling.

SX0550 In Figure 34, above the shakedown regime, if $\tau_m = 0$, the temperature change causes cyclic in-plane strain but no shear strain. However, this cyclic state is unstable. Any shear stress τ_m, however small, will cause the film to crawl. In the crawling regime, the in-plane strain cycles

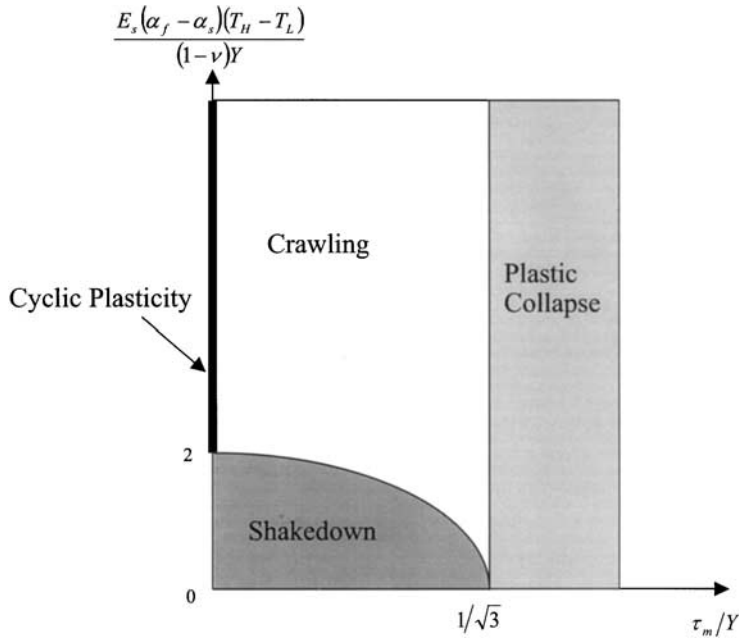

Figure 34 Various regimes on the plane spanned by the normalized shear stress in metal and the normalized temperature range.

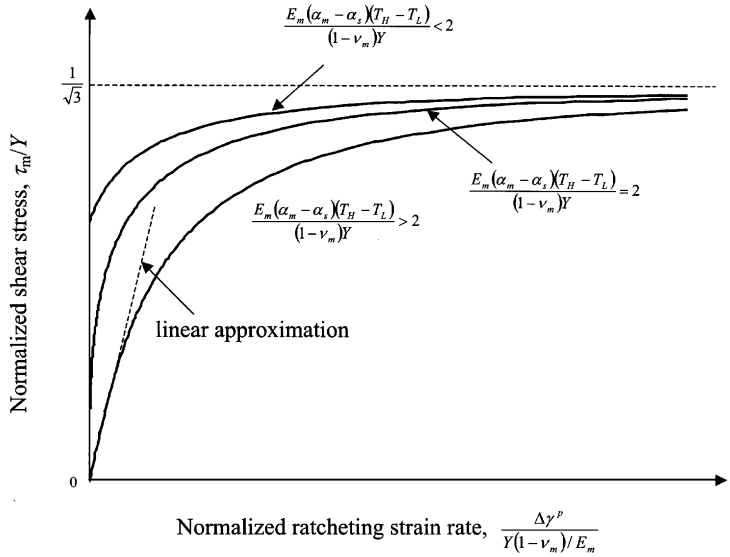

Figure 35 Shear stress as a function of the ratcheting strain rate.

plastically, but the shear strain increases by a fixed amount each cycle, given by

$$\Delta\gamma^{\mathrm{p}} = \frac{12(1-\nu_{\mathrm{m}})\tau_{\mathrm{m}}}{E_{\mathrm{m}}}\left[\frac{E_{\mathrm{m}}(\alpha_{\mathrm{m}}-\alpha_{\mathrm{s}})(T_{\mathrm{H}}-T_{\mathrm{L}})}{(1-\nu_{\mathrm{m}})\sqrt{Y^2-3\tau_{\mathrm{m}}^2}}-2\right]. \tag{80}$$

SX0555 Figure 35 plots the ratcheting strain per cycle, $\Delta\gamma^{\mathrm{p}}$, as a function of the shear stress, τ_{m}. We make an analogy between the strain *per temperature cycle* (i.e., the ratcheting rate) and the strain *per unit time* (i.e., the strain rate). Figure 35 is thus analogous to the relation between strain rate and stress in viscous flow. In general, we write the ratcheting rate law as $\partial\gamma^{\mathrm{p}}/\partial N = f(\tau_{\mathrm{m}})$. The shear stress should be bounded as $\tau_{\mathrm{m}}/Y < 1/\sqrt{3}$; otherwise, the film has unlimited plastic shear strain even without the temperature change. As $\tau_{\mathrm{m}}/Y \to 1/\sqrt{3}$, the ratcheting rate becomes large for any given temperature ranges. Depending on the temperature range, we distinguish several behaviors as follows.

SX0560 When $E_{\mathrm{m}}(\alpha_{\mathrm{m}}-\alpha_{\mathrm{s}})(T_{\mathrm{H}}-T_{\mathrm{L}})/[(1-\nu_{\mathrm{m}})Y] > 2$, the temperature change by itself can cause the metal film to deform plastically in every cycle. When the shear stress is zero, the metal film undergoes cyclic in-plane plastic deformation, and has no shear strain. When the shear stress is small, the ratcheting rate is linearly proportional to the shear stress:

$$\frac{\partial\gamma^{\mathrm{p}}}{\partial N} = \frac{\tau_{\mathrm{m}}}{\eta_{\mathrm{R}}}. \tag{81}$$

We call η_{R} the ratcheting viscosity. A comparison between Equations (80) and (81) gives

$$\eta_{\mathrm{R}} = \frac{E_{\mathrm{m}}}{12(1-\nu_{\mathrm{m}})}\left[\frac{E(\alpha_{\mathrm{m}}-\alpha_{\mathrm{s}})(T_{\mathrm{H}}-T_{\mathrm{L}})}{(1-\nu_{\mathrm{m}})Y}-2\right]^{-1}. \tag{82}$$

The linear ratcheting is analogous to the Newtonian viscous flow. The ratcheting viscosity has the dimension of elastic modulus, and increases when the temperature range decreases. We will mainly use the linear ratcheting approximation (82) in the subsequent development.

When $E_{\mathrm{m}}(\alpha_{\mathrm{m}}-\alpha_{\mathrm{s}})(T_{\mathrm{H}}-T_{\mathrm{L}})/[(1-\nu_{\mathrm{m}})Y] < 2$, SX0565 the metal film yields only when the shear stress exceeds a critical value, namely, when the quantity in the bracket in Equation (80) is positive. As seen in Figure 35, this behavior is analogous to the Bingham viscous flow.

When $E_{\mathrm{m}}(\alpha_{\mathrm{m}}-\alpha_{\mathrm{s}})(T_{\mathrm{H}}-T_{\mathrm{L}})/[(1-\nu_{\mathrm{m}})Y] = 2$, SX0570 for small shear stress, Equation (80) gives rise to a power-law behavior, $\partial\gamma^{\mathrm{p}}/\partial N \sim \tau_{\mathrm{m}}^3$.

8.7.4.5 The Transient Process to Approach the Steady State

bib56 Huang *et al.* (2002) have developed a SX0575 one-dimensional model of ratcheting of the thin film structures. As shown in Figure 36, a metal film is in a thick elastic substrate, and the passivation thin film is on the metal film and the substrate. A constant shear stress, τ_0, due to the packaging substrate, is applied on the passivation film. The metal film is of thickness H and length L. The passivation film is of thickness h. Cycle the structure between T_{H} and T_{L}. The shear stress in the metal film is τ_{m}, and the normal stress in the passivation film is

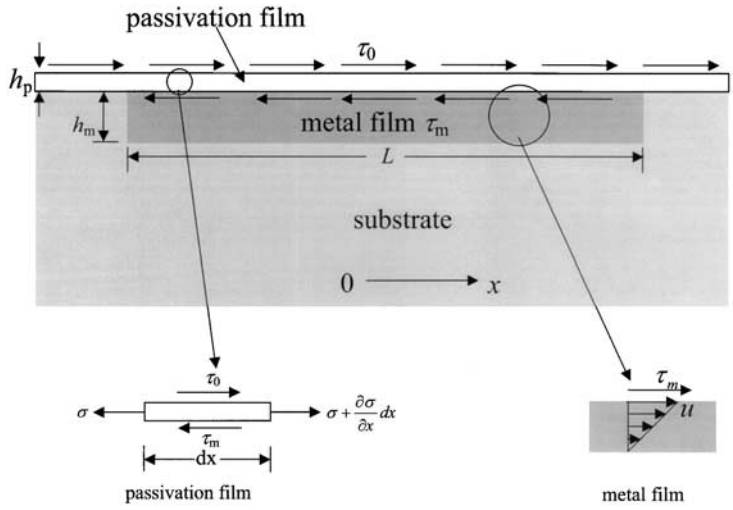

Figure 36 Illustration of one-dimensional structure of passivation film on the metal film and substrate. The insets show the different elements and the stress states of the passivation film, and the stress and flow in the metal film.

σ. Now both τ_m and σ are allowed to vary with the number of cycles, N, and the position, x. We expect τ_m to vary slowly with N and x, so that we will use the ratcheting rate law obtained in the last section.

SX0580 First look at the elastic passivation film. As shown in the inset in Figure 36, the passivation film is subjected to a membrane stress $\sigma(N, x)$, a constant shear stress τ_0 on the top surface, and a variable shear stress $\tau_m(N, x)$ on the bottom surface. The force balance of the differential element requires that

$$\frac{\partial\sigma}{\partial x}=\frac{\tau_m-\tau_0}{h}. \tag{83}$$

Let $u(N, x)$ be the displacement of the passivation film in the x-direction. Elasticity of the passivation film requires that

$$\sigma=E_p\frac{\partial u}{\partial x}, \tag{84}$$

where E_p is Young's modulus of the passivation film.

SX0585 Next look at the ratcheting metal film. The shear strain relates to the displacement as $\gamma^p = u/H$. We assume that the temperature range is large, $E_m(\alpha_m-\alpha_s)(T_H-T_L)/[(1-\nu_m)Y]>2$. Consequently, we adopt the shear stress and plastic shear strain increment relation (13) as

$$\tau_m=\eta_R\frac{\partial u}{H\partial N}. \tag{85}$$

The ratcheting viscosity η_R is defined by Equation (82).

SX0590 Substituting Equations (84) and (85) into Equation (83) gives the governing equation:

$$\frac{\partial u}{\partial N}=D_R\frac{\partial^2 u}{\partial x^2}+\frac{H\tau_0}{\eta_R}. \tag{86}$$

We introduce the ratcheting diffusivity as

$$D_R=E_p hH/\eta_R. \tag{87}$$

Equation (86) is a diffusion equation with a source term.

SX0595 We assume no separation between the metal film and the substrate, so that the displacement of the metal film at the two edges is the same as the displacement of the substrate. As the substrate is semi-infinite and elastic, its displacement is negligible compared to the accumulated displacement in the passivation film. Consequently, the boundary conditions for the displacement of the passivation film are

$$u=0 \quad \text{at} \quad x=\pm L/2 \quad \text{for all } N. \tag{88}$$

SX0600 Because the temperature range is large enough to cause the metal to yield in every cycle, so long as there exists a shear stress τ_m in the metal, the metal will ratchet. After many temperature cycles, the structure will reach the steady state, in which the shear stress in the metal film vanishes, $\tau_m=0$, but the cycling temperature still causes the metal film to yield cyclically. The steady state can be obtained by setting $\partial u/\partial N=0$ and satisfying the boundary conditions (88). In the steady state, τ_0 is fully sustained by the membrane stress in the passivation film, giving rise to a linear membrane stress distribution (69).

SX0605 Analogous to any diffusion problem, the characteristic number of cycles to reach the

steady state can be estimated by $N_C = L^2/D_R$, or

$$N_C = \left(\frac{L^2}{hH}\right)\frac{E_m}{12E_p(1-\nu_m)} \times \left[\frac{E_m(\alpha_m-\alpha_f)(T_H-T_L)}{(1-\nu_m)Y} - 2\right]^{-1}. \quad (89)$$

The number N_C can be large mainly because the ratio $L^2/(hH)$ is large. If one replaces the metal film with a plastically deformable polymer, the ratio of elastic modulus of the polymer and the passivation is small, which would significantly reduce N_C. Note that N_C is independent of τ_0.

SX0610 In the above, the metal film is taken to be a nonhardening material in this model. This corresponds to a safe engineering design, as the hardening metal film can reduce the ratcheting effects (bib55 Huang *et al.*, 2001). The model can also be easily extended to consider the nonlinearity of the ratcheting viscosity by using the finite difference method. The stress concentration at the edges needs to be treated better, as the maximum tensile stress in the passivation film is at the corner. Fracture conditions also need to be considered more carefully. Several useful rules for design are evident. First, one should aim to avoid metal film ratcheting altogether. Under cyclic temperature, the metal film cycles elastically if the temperature range is small and the yield strength of the metal is large, according to (77). Second, if one cannot avoid ratcheting, one may aim to design the metal film geometry such that the passivation film can sustain the steady state, in which the stress distribution in the passivation film can be calculated by solving a linear elastic plane-stress problem. Third, if the characteristic number N_C is much larger than the number of cycles required by the qualification test, one may design according to the transient stress state, solving the stress field as a function of the number of cycles. The present model allows one to evaluate these options in design.

8.7.4.6 Ratcheting-induced Crack Growth

SX0615 Consider the structure illustrated in Figure 10 again. In the present context, a brittle film lies on a metal underlayer, which in turn lies on a rigid substrate. Cycle the structure between temperatures T_L and T_H. Within the temperature and time of the experiment, the metal does not creep, but can have time-independent plastic deformation. For simplicity, assume that the tensile stress in the uncracked blanket film, σ, is constant as the temperature changes. This happens in practice when the elastic film and the substrate have a similar coefficient of thermal expansion, and σ is due to the deposition process or an applied load. As temperature cycles, the metal layer undergoes ratcheting plastic deformation. The stress field in the film relaxes in the crack wake, and intensifies around the crack tip. By the ratcheting-creep analogy, we rewrite the scaling law for the crack velocity (38) as the scaling law for crack growth per cycle (bib78 Liang *et al.*, 2002a):

$$\frac{da}{dN} = 0.6\frac{Hh\sigma^2}{\eta_R\Gamma}, \quad (90)$$

where η_R is given by (82), and Γ is the fracture energy of the brittle film.

8.7.5 STRESS-INDUCED VOIDING

SX0620 This section begins with a description of stress-induced voiding (SIV), followed by an analysis of its main features: saturated void volume, resistance change, stress generation, void initiation, void growth, and stress relaxation. We then give an analytical model of nonhydrostatic stress state in an elastic–plastic interconnect line encapsulated in a dielectric. An observation of SIV in blanket copper films is discussed. We finally consider the effects of low-k dielectrics and barriers. bib98 Okabayashi (1993) and bib114 Sullivan (1996) have provided two reviews on SIV. This section will focus on physical descriptions of the phenomenon, leaving the design implications to the next section, after we have studied electromigration.

8.7.5.1 Stress-Induced Voiding in Encapsulated Metal Line

SX0625 Early aluminum lines had the width much larger than the thickness. They behaved like blanket films. When narrow aluminum lines were introduced, voids were observed on wafers held in ovens, or even on wafers left on shelves at room temperature (bib24 Curry *et al.*, 1984; bib140 Yue *et al.*, 1985; bib128 Turner and Wendel, 1985). The voids may be crack-like or rounded, grow with time, and sever the interconnects (Figure 37).

SX0630 A basic understanding soon followed (bib64 Jones and Basehore, 1987; bib45 Hinode *et al.*, 1990; bib38 Greenebaum *et al.*, 1991; bib68 Korhonen *et al.*, 1991; bib106 Sauter and Nix, 1992). Aluminum has a larger thermal expansion coefficient than silica. Encapsulated in silica at a high temperature, on cooling, a narrow aluminum line is in a tensile, triaxial

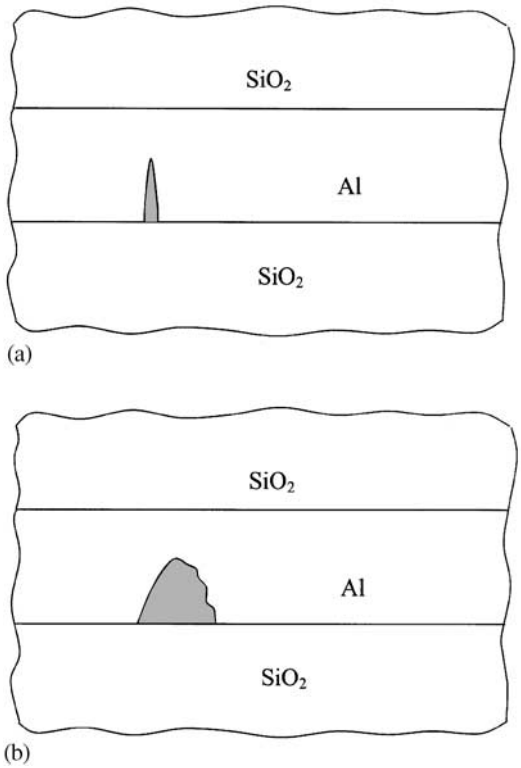

Figure 37 Voids grow in aluminum lines encapsulated in silica after some storage time. (a) Crack-like void and (b) rounded void.

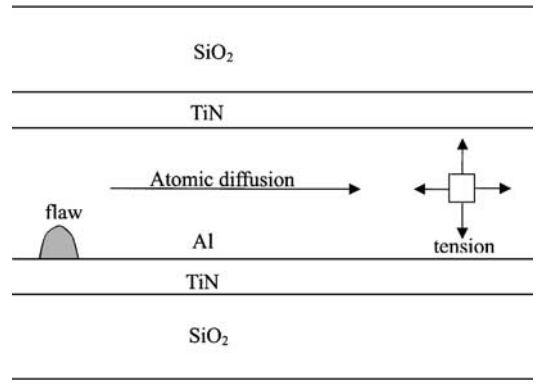

Figure 38 An encapsulated aluminum line is under triaxial tension. The stress vanishes at a flaw. The stress gradient motivates aluminum atoms to diffuse in the line, and simultaneously grow the void and relax the stress.

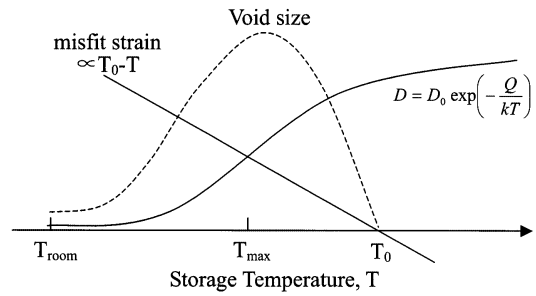

Figure 39 As the temperature drops from the stress-free temperature T_0, the misfit strain increases, but the atomic diffusivity decreases. For a given time duration, the void size maximizes at an intermediate temperature $T_{\max}$.

stress state. The magnitude of the stress in aluminum readily exceeds the yield strength of aluminum. Indeed, even a liquid with zero yield strength, so encapsulated, would be under hydrostatic tension. Over a long time, a small piece of a crystal is like a liquid in that they both creep under shear. An encapsulated metal line under uniform hydrostatic tension is in a state of equilibrium: atoms have no motivation to diffuse from one place to another. However, this equilibrium state is metastable. A flaw may act like a void nucleus. If the stress near the flaw is low or vanishes, the nonuniform stress field motivates aluminum atoms to diffuse away from the flaw, simultaneously growing the void and relaxing the tensile stress (Figure 38). The metal line approaches a stable equilibrium state consisting of voids and unstressed metal.

SX0635 An accelerated testing method has also been developed, known as the high-temperature storage (HTS) test. The aluminum line is stress-free at a temperature T_0, which is close to the silica deposition temperature. Samples are kept in an oven at some temperature T below T_0. The thermal expansion mismatch volume scales with the temperature drop, $T_0 - T$. It is this mismatch volume that feeds to the void. The atomic diffusivity depends on the temperature as $D = D_0 \exp(-Q/kT)$, where k is Boltzmann's constant, Q the activation energy, and D_0 the frequency factor. As the temperature drops, the mismatch volume increases, but the diffusivity decreases (Figure 39). Consequently, voids grow fastest at a particular temperature $T_{\max}$. During the storage test, the electrical resistance of a line is measured as a function of time. The line fails if its resistance increases by, say 20%. The time to fail half of the lines, i.e., the median-time-to-failure (MTF), is fit to a semi-empirical relation (bib90 McPherson and Dunn, 1987):

$$\mathrm{MTF} = \frac{C}{(T_0 - T)^N} \exp\left(\frac{Q}{kT}\right), \qquad (91)$$

where C and N are fitting parameters, along with T_0 and Q. This relation captures the above physical considerations. The failure time approaches infinity when the test is carried either

at the stress-free temperature T_0, or at absolute zero. To obtain the fitting parameters, the storage tests are carried out at several temperatures, possibly around T_{max} to shorten the testing time. Equation (91) is then extrapolated to predict the failure time at, say, room temperature.

SX0640 SIV is mitigated in aluminum interconnects in several ways. First, adding a few percent of copper into aluminum reduces the diffusion rate by nearly two orders of magnitude (bib5 Ames *et al.*, 1970). Second, materials of negligible diffusion rates, such as W and TiN, are used as shunts (Figure 38), so that a void in the aluminum line does not open the circuit, but just increases the electrical resistance somewhat (bib48 Howard *et al.*, 1978). Third, a short aluminum line cannot grow a large void, because the volume of material to be relaxed is small (bib32 Filippi *et al.*, 1995). These measures were all originally developed to mitigate electromigration voiding.

SX0645 The interest in SIV resurged during the later 1990s since copper lines entered the interconnect structure. Voids have been observed in electron beam evaporated copper lines, and found to be sensitive to the texture (bib66 Keller *et al.*, 1997). On-chip copper lines are electroplated, and have small initial grains. If the lines are not properly annealed before encapsulation, later annealing will cause grain growth, densify copper, and induce voids (bib47 Hommel *et al.*, 2001; bib96 Ogawa *et al.*, 2002). In aluminum interconnects, voids grow in the lines, but not in the tungsten vias. By contrast, in copper interconnects, vias themselves are made of copper, and are susceptible to voiding (Figure 40). Furthermore, compared to aluminum, copper has large yield strength and a high degree of elastic anisotropy. Stress concentration arises at the junction of the copper grain boundary and SiN top layer; voids have been observed even in blanket copper films (bib109 Shaw *et al.*, 2001; AU:5 bib107 Sekiguchi, 2001).

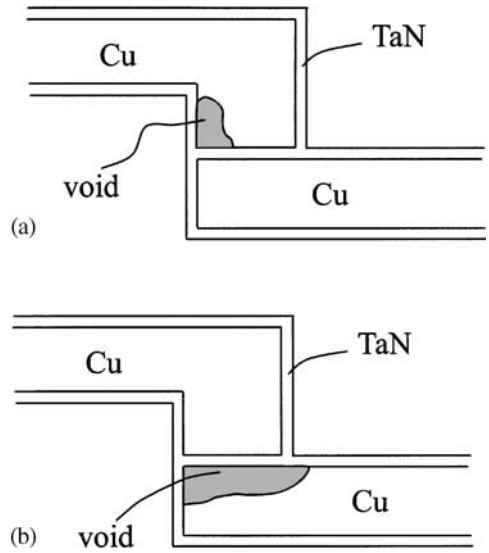

Figure 40 In the copper interconnect structure, vias are also made of copper, and are susceptible to stress-induced voiding.

8.7.5.2 An Analysis of Stress-Induced Voiding

SX0650 Despite efforts in for nearly two decades (1980s and 1990s), there is no single model that accounts for all aspects of SIV. Complicated factors (e.g., grain structures, flaws, interfaces, and atomic transport mechanisms) play roles. Detailed information of such factors is incompletely known, and will probably never be precisely controlled in fabrication. At this point, it seems desirable to consider the physics of the phenomenon semi-quantitatively. In this spirit, the following sub-models are given in outline.

(i) Saturated Void Volume (SVV)

SX0655 An encapsulated metal line is stress free at a high temperature T_0, and is cooled to the storage test temperature T. The total number of atoms in the line is constant at all time. Because atomic transport does not change the volume of the metal, the thermal misfit strain is accommodated by a combination of void space and elastic deformation. When the stress in the line completely relaxes, the thermal expansion misfit is fully accommodated by the void space. The saturated void volume (SVV) is

$$V_{sv} = 3\Delta\alpha(T_0 - T)\,V, \tag{92}$$

where V is the volume of the metal line, and $\Delta\alpha$ is the effective thermal expansion mismatch strain. If a metal line were embedded in silicon, $\Delta\alpha = \alpha_m - \alpha_{Si}$, where α_m and α_{Si} are the thermal expansion coefficients of the metal and silicon, respectively ($\alpha_m = 24 \times 10^{-6}\,K^{-1}$ for aluminum and $17 \times 10^{-6}\,K^{-1}$ for copper). In an interconnect structure, however, $\Delta\alpha$ depends on all materials in the structure. For the silica-based interconnect structure, because the metals have much larger thermal expansion coefficients than the surrounding materials (silica, silicon, silicon nitride, and tantalum), the thermal expansion mismatch is insensitive to which exact value is used for these other materials; we

will use $\Delta\alpha = \alpha_m - 4 \times 10^{-6}\,K^{-1}$ in the following estimates. A representative stress-free temperature is 400°C, and a representative storage test temperature is 200°C. Taking these values, one finds that $V_{sv}/V = 1.2\%$ for aluminum, and $V_{sv}/V = 0.78\%$ for copper. For a line of size $1\,\mu m \times 1\,\mu m \times 10\,\mu m$, the saturated void, if it is a single spherical one, has radius 306 nm for aluminum, and 265 nm for copper. The interconnect structure with low-k dielectrics will be discussed in Section 8.7.5.6.

SX0660 Many voids may nucleate along the metal line, each growing to relax stress in its vicinity. Once the stress completely relaxes, the sum of the volumes of all the voids remains constant as the line is held at the constant temperature. Equation (92) gives this sum. The actual void volume can be larger or smaller than the SVV. When a line is cooled to a low temperature for a short time, the tensile stress partially relaxes, so that the total void volume is smaller than the SVV. If the line is then brought to a high temperature, for some time the metal is under compression, and the void volume is larger than the SVV. In case of a copper line, we assume that the electroplated copper has been annealed to allow densification prior to encapsulation, so that only thermal expansion mismatch contributes to void volume.

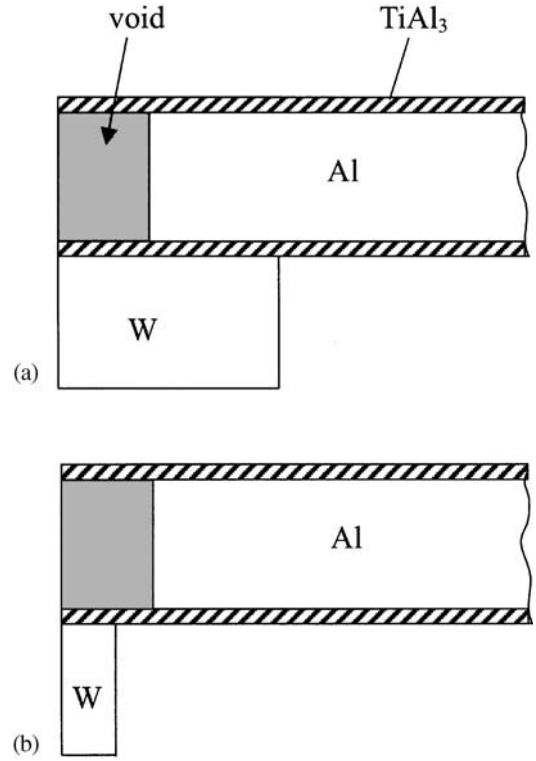

Figure 41 (a) Void length smaller than tungsten stud diameter and (b) void length larger than tungsten stud diameter.

(ii) Resistance Increase

SX0665 A line fails when the voids significantly increase the resistance of the line. The resistance change does not uniquely relate to the void volume. Small, isolated voids do not cause as much resistance increase as a single large void that depletes a segment of the metal line. Even when only one void is left near a via, the resistance change depends on geometry. Figure 41 compares two identical voids, the only difference being the size of the tungsten studs relative to the void. Evidently, the resistance increases in Figure 41(a) is smaller than that in Figure 41(b).

SX0670 When the void length exceeds several times the linewidth, the resistance increase can be estimated from the void length. Let ρ be the resistivity of the interconnect, L its length, and A its cross-sectional area. The resistance of a void-free interconnect is $R = \rho L/A$, ignoring the conductance due to the aluminide shunt layers. Let ρ_1 and A_1 be the resistivity and the cross-sectional area of the aluminide layers. When a void of length L_1 appears in the line, current flows in the aluminide layers, and the resistance increases by $\Delta R = \rho_1 L_1/A_1$, where the resistance of aluminum of length L_1 is neglected. Consequently, the relative resistance increase is

$$\frac{\Delta R}{R} = \frac{\rho_1 L_1/A_1}{\rho L/A}. \tag{93}$$

Everything else being equal, the thicker the shunt layers, the smaller the resistance change. Taking $\rho_1/\rho = 10$, $A_1/A = 0.1$, and $L_1/L = 1.0\%$, one finds that $\Delta R/R = 100\%$.

(iii) Hydrostatic Tension in Encapsulated Metal Line

SX0675 The stress field in the metal line is complicated in general, with tensor components and nonuniformity along the line. To grow a large void, atoms must diffuse in the line over a length much larger than the linewidth. On such a timescale, creep should have relaxed each point in the line to a hydrostatic state (bib68 Korhonen *et al.*, 1991). That is, over a sufficient long timescale, at an elevated temperature, a crystal behaves like a liquid. The hydrostatic stress in the metal line prior to voiding can be calculated as follows. Figure 42 illustrates separately the metal line and the dielectric. In the metal line, the stress state has components of an equal magnitude σ in all directions. The stress causes the metal to

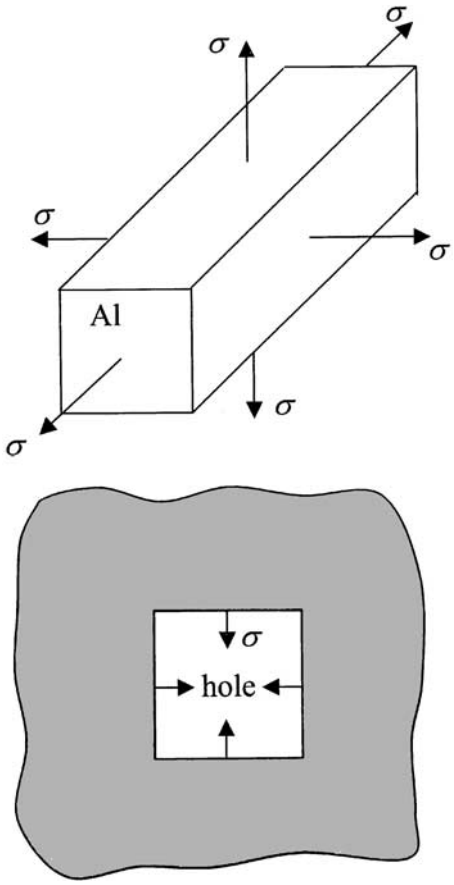

Figure 42 Consider separately the metal line as a cylinder and the dielectric as a solid with a hole.

expand with the volumetric elastic strain σ/B_m, where B_m is the bulk modulus of the metal. When the metal is modeled as an isotropic material, the bulk modulus relates to Young's modulus E_m and Poisson's ratio ν_m as $B_m = E_m/3(1-2\nu_m)$. For a metal of cubic crystalline symmetry, the bulk modulus relates to its crystalline elastic constants as $B_m = (C_{11}+2C_{12})/3$. For aluminum, $C_{11} = 108\,\text{GPa}$, $C_{12} = 62\,\text{GPa}$, $C_{44} = 28\,\text{GPa}$, giving $B_m = 77\,\text{GPa}$. For Copper, $C_{11} = 168\,\text{GPa}$, $C_{12} = 121\,\text{GPa}$, $C_{44} = 75\,\text{GPa}$, giving $B_m = 136\,\text{GPa}$.

SX0680 Regard the encapsulation as an elastic solid with a hole subject to a normal traction of magnitude σ. The dielectric is in a state of plane-strain deformation. The traction causes the cross-sectional area of the hole to reduce by $\int u_n \, ds$, where u_n is the normal component of the elastic displacement at the hole surface. Let A be the cross-sectional area of the hole. Linearity of the elastic field requires that

$$\frac{1}{A}\int u_n \, ds = -\frac{\sigma}{\mu_{\text{eff}}}. \tag{94}$$

This equation defines an effective modulus μ_{eff}. This effective modulus depends on the shape of the hole, as well as the elastic constants of the dielectric, the barrier, and the silicon substrate. The effective modulus can be readily calculated using the finite element method (Section 8.7.5.6). If the cross-section is a long rectangle, rather than a square, the system is more compliant, leading to a small μ_{eff}. In the idealized case, when the hole has a circular cross-section, and the dielectric is infinite, the stress field in the dielectric is known analytically, and we find that the effective modulus is $\mu_{\text{eff}} = E_d/2(1+\nu_d)$, coincident with the shear modulus of the dielectric.

Let θ be the volumetric strain caused, e.g., by SX0685 the mismatch in thermal expansion coefficients, or densification, or atomic diffusion. This volumetric strain is accommodated by the difference in the volume change of the interconnect line and that of the dielectric hole. Combining the two contributions, one relates the hydrostatic stress in the metal, σ, to the volumetric mismatch strain between the metal and the encapsulation, θ, namely,

$$\sigma = B\theta, \tag{95}$$

with the effective modulus B given by

$$\frac{1}{B} = \frac{1}{B_m} + \frac{1}{\mu_{\text{eff}}}. \tag{96}$$

If the cross-section is a long rectangle, the effective modus is small, leading to a low hydrostatic stress. In the limiting case when the interconnect is a blanket film, the hydrostatic stress vanishes in this liquid-like model. For an interconnect of a square cross-section, taking $\mu_{\text{eff}} = 30\,\text{GPa}$ for silica, the effective modulus is $B = 22\,\text{GPa}$ for aluminum/silica structure, and $B = 24\,\text{GPa}$ for copper/silica structure. The mismatch strain is mainly accommodated by the elastic deformation of the dielectric, so that the effective moduli of the two structures are similar, despite the nearly factor 2 difference in the bulk moduli of aluminum and copper. The effective modulus reduces if the cross-section is a long rectangle. Assume that the volumetric strain is entirely due to the thermal expansion mismatch between the metal and the dielectric, $\theta = 3\Delta\alpha(T_0 - T)$. For the temperature drop $T_0 - T = 200\,\text{K}$, the hydrostatic stress is $\sigma = 260\,\text{MPa}$ in aluminum line, and $\sigma = 187\,\text{MPa}$ in copper line. Some authors have treated the dielectric as a rigid material, and taken the bulk modulus of the metal, B_m, as the effective modulus. This would significantly overestimate the effective modulus ($B_m/B = 3.5$ for aluminum and $B_m/B = 5.7$ for copper).

(iv) Void Initiation

SX0690 Next consider a void-like flaw in a metal subject to a hydrostatic stress. The void can change its size by relocating atoms from the void surface into the metal far away from the void. In doing so, the void increases its surface area, and the remote stress does work. The former increases the free energy, but the latter decreases it. Will the void shrink or enlarge? For the time being, we assume that the void volume changes slightly, so that the number of atoms transported into the line is so small that the stress σ does not change. Take the solid without the void but under the same applied stress as the ground state, at which the system has zero free energy. The current state has a void of radius a. Let γ be the surface energy per unit area. In creating the void, a surface of area $4\pi a^2$ is exposed, raising the free energy of the system by $\gamma 4\pi a^2$. At the same time, atoms occupying the volume $4\pi a^3/3$ relocate, allowing the remote stress to do work $\sigma(4\pi a^3/3)$. Thus, the free energy of the system, relative to that of solid with no void, is

$$F(a) = 4\pi a^2\gamma - \tfrac{4}{3}\pi a^3\sigma. \tag{97}$$

Figure 43 sketches the free energy as a function of the void radius. When $a=0$, $F=0$, which is the ground state. When the void is small, the surface energy dominates, and the void shrinks to reduce the free energy. When the void is large, the stress dominates, and the void enlarges to reduce the free energy. The two behaviors are separated at a critical void radius a^*, at which the free energy maximizes. The critical void radius is given by $a^* = 2\gamma/\sigma$. Taking representative values, $\gamma = 1\ \mathrm{J\,m^{-2}}$ and $\sigma = 200\,\mathrm{MPa}$, we find that the critical radius is $a^* = 10\,\mathrm{nm}$. If the pre-existing flaw size a is known, the flaw can grow if the stress exceeds the value

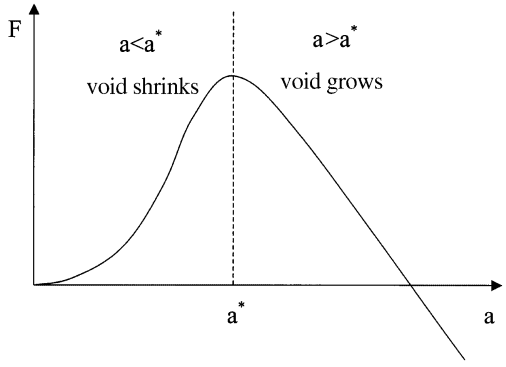

Figure 43 The free energy as a function of void radius.

$$\sigma_{\mathrm{void}} = 2\gamma/a. \tag{98}$$

The use of this condition will be critiqued in Section 8.7.6.3.

(v) Void Growth and Stress Relaxation

Because the volumetric strain due to thermal expansion mismatch is on the order of 10^{-2}, SX0695 for a void to grow to a size to sever the line, a long length of the metal has to be relaxed. The long-range diffusion samples the averages of various quantities, and is a much more robust process than void initiation. bib69 Korhonen *et al.* (1993) formulated a model to study atomic diffusion in an encapsulated metal line. To study mass transport over a length exceeding several times the linewidth, one can assume that the stress state is hydrostatic, varying along the line and with time. Let the x-axis coincide with the line. The stress in the line is a function of position and time, $\sigma(x,t)$. The nonuniformity of the stress motivates atoms to diffuse to the region of large tension. When an atom is removed from a stress-free solid, and then added to another solid under hydrostatic tension σ, the free energy reduces by $\Omega\sigma$, where Ω is the volume per atom in the metal. Consequently, the driving force to relocate atoms in the metal line is

$$f = \Omega\frac{\partial\sigma}{\partial x}. \tag{99}$$

Let J be the atomic flux, i.e., the number of atoms crossing per unit area per unit time. Write the Einstein relation as

$$J = \frac{Df}{\Omega kT}. \tag{100}$$

The diffusivity D is taken to be the average along the aluminum line. The flux divergence gives rise to the volumetric strain per unit time, $\partial\theta/\partial t = \Omega\partial J/\partial x$. Recall that the mismatch volumetric strain relates to the stress by $\sigma = B\theta$. . Consequently, the stress rate is proportional to the flux divergence:

$$\frac{\partial\sigma}{\partial t} = B\Omega\frac{\partial J}{\partial x}. \tag{101}$$

A combination of the above equations gives SX0700

$$\frac{\partial\sigma}{\partial t} = \frac{DB\Omega}{kT}\frac{\partial^2\sigma}{\partial x^2}. \tag{102}$$

This partial differential equation, together with suitable initial and boundary conditions, governs the evolving pressure distribution, $\sigma(x,t)$.

Solutions of practical interest can be found in (bib69 Korhonen *et al.*, 1993).

SX0705 With reference to Figure 38, assume that the flaw is already large enough so that the stress near the flaw is zero. Equation (102) is identical to the usual diffusion equation, with the diffusivity-like quantity $DB\Omega/kT$. The solution to this initial-boundary value problem is well known. The time for a void to relax a segment of interconnect of length l scales as

$$t_l \sim \frac{l^2 kT}{DB\Omega}. \tag{103}$$

The void fails a line by increasing the resistance of the line to a designated value. Assume that void of length L_1 corresponds to the failure. To grow a void of length L_1, the segment of the metal line needed to be relaxed is about $l = L_1/3(\alpha_m - \alpha_d)(T_0 - T)$. Inserting into (103), we obtain the lifetime

$$t_{\text{life}} \propto \frac{1}{B[(\alpha_m - \alpha_d)(T_0 - T)]^2} \exp\left(\frac{Q}{kT}\right). \tag{104}$$

This expression looks similar to (91). As noted before, the effective modulus B depends on the cross-section shape and the dielectric type. Other things being the same, a structure with a smaller B will lead to a longer lifetime.

8.7.5.3 Nonhydrostatic Stress State in Encapsulated Metal Line

SX0710 The presence of the yield strength causes a nonhydrostatic stress state in the metal line, and also increases the magnitude of all stress components. According to (98), a higher stress can activate a smaller flaw to grow into a void. The stresses in encapsulated elastic plastic metal lines have been studied by using finite element methods (bib64 Jones and Basehore, 1987; bib38 Greenebaum *et al.*, 1991; bib37 Gouldstone *et al.*, 1998).

SX0715 To gain insight into this phenomenon, we give an analytical solution for an idealized model, in which a long metal line of cylindrical cross-section, radius a, is encapsulated in an infinite dielectric (Figure 44). The dielectric is elastic, with Young's modulus E_d, Poisson's ratio ν_d, and thermal expansion coefficient α_d. The corresponding properties for the metal are E_m, ν_m, and α_m. Now consider the metal and the dielectric separately as a cylinder and an infinite solid with a cylindrical hole. The metal is under a uniform, triaxial stress field, with a longitudinal component σ_L and two transverse components of equal magnitude σ_T. The transverse stress σ_T also acts on the hole surface in the dielectric. The dielectric is taken

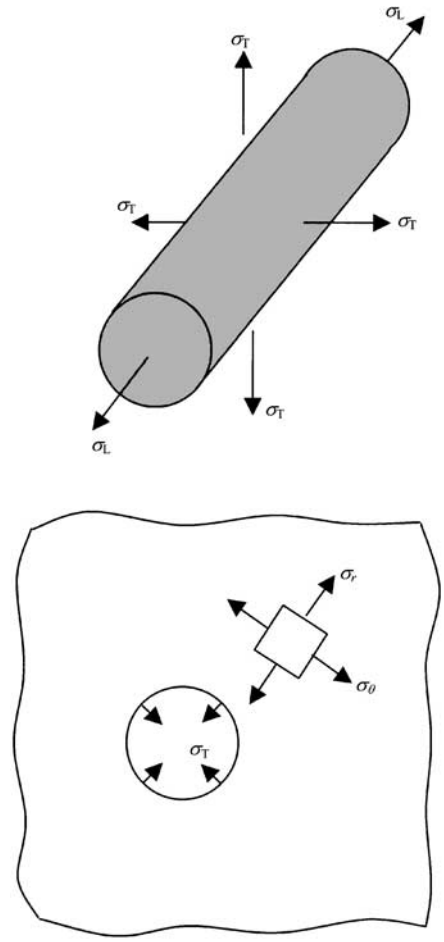

Figure 44 The metal is under a triaxial stress state, with the transverse stress different from the longitudinal stress. The dielectric is subject to a radial stress at the surface.

to be infinite, and the longitudinal stress in the dielectric is zero. Inside the dielectric, the stress field decays away from the hole. According to the Lame solution, the radial stress σ_r and the hoop stress σ_θ in an infinite elastic solid subject to a stress on a hole surface are given by (bib127 Timoshenko and Goodier, 1970)

$$\sigma_r(r) = \sigma_T(a/r)^2, \qquad \sigma_\theta(r) = -\sigma_T(a/r)^2, \tag{105}$$

where r is the radial distance. Consequently, the stress field in the composite is determined once σ_L and σ_T are determined.

Next consider the strains. When the temperature changes by ΔT, the stresses change by $\Delta\sigma_T$ and $\Delta\sigma_L$. The change in the longitudinal strain in the dielectric is caused by thermal expansion: SX0716

$$\Delta\varepsilon_L^d = \alpha_d \Delta T. \tag{106}$$

On the hole surface, the radial and the hoop

stresses in the dielectric are $\sigma_r = \sigma_T$ and $\sigma_\theta = -\sigma_T$. The change in the hoop strain is the sum of that caused by thermal expansion and that caused by the stresses:

$$\Delta\varepsilon_\theta^d = \alpha_d \Delta T - \frac{1+\nu_d}{E_d}\Delta\sigma_T. \quad (107)$$

When we consider the strains in the metal, the analysis will depend on whether the metal has yielded. First assume that the metal is elastic. The changes in the strains in the metal are

$$\Delta\varepsilon_L^m = \alpha_m \Delta T + \frac{1}{E_m}\Delta\sigma_L - \frac{2\nu_m}{E_m}\Delta\sigma_T, \quad (108)$$

$$\Delta\varepsilon_\theta^m = \alpha_m \Delta T - \frac{\nu_m}{E_m}\Delta\sigma_L + \frac{(1-\nu_m)}{E_m}\Delta\sigma_T. \quad (109)$$

Because the metal and the dielectric are well bonded, so that the strains across the interface are compatible: $\Delta\varepsilon_L^d = \Delta\varepsilon_L^m$ and $\Delta\varepsilon_\theta^d = \Delta\varepsilon_\theta^m$. Solving two coupled linear algebraic equations, we obtain that

$$\Delta\sigma_T = -\frac{(1+\nu_m)(\alpha_m - \alpha_d)\Delta T}{(1+\nu_m)(1-2\nu_m)/E_m + (1+\nu_d)/E_d}, \quad (110)$$

$$\Delta\sigma_L = -E_m(\alpha_m - \alpha_d)\Delta T + 2\nu_m \Delta\sigma_T. \quad (111)$$

When the metal and the dielectric have similar elastic constants, the stresses become

$$\Delta\sigma_T = -\frac{E}{2(1-\nu)}(\alpha_m - \alpha_d)\,\Delta T, \quad (112)$$

$$\Delta\sigma_L = -\frac{E}{1-\nu}(\alpha_m - \alpha_d)\,\Delta T. \quad (113)$$

SX0720 So far we have assumed that the metal is elastic. For representative values, $E_m = 10^{11}$ Pa, $\alpha_m - \alpha_d = 20 \times 10^{-6}\,K^{-1}$, and $\Delta T = 500$ K, the stress is about 1 GPa, which exceeds typical yield strength of metals. We next allow the metal to yield plastically. Recall that the metal is under a triaxial stress state $(\sigma_L, \sigma_T, \sigma_T)$. It is an empirical fact that superimposing a hydrostatic stress does not affect the plastic deformation of a metal. Imagine that we superimpose a hydrostatic state $(-\sigma_T, -\sigma_T, -\sigma_T)$ to the metal, so that the metal is under a uniaxial stress state $(\sigma_L - \sigma_T, 0, 0)$. We assume that metal is nonhardening, and the yield strength Y is independent of the temperature. One can readily modify the model to allow the yield strength to vary the temperature and strain, or even include the effect of creep. The metal and the dielectric are perfectly bonded. Consequently, the metal yield when the difference in the longitudinal and the transverse stress reaches the yield strength:

$$|\sigma_L - \sigma_T| = Y. \quad (114)$$

SX0725 After yielding, when the temperature changes, the two stresses can still change, provided they change by the same amount, $\Delta\sigma_L = \Delta\sigma_T$. Let the plastic strain in the longitudinal direction be ε^p. Because plastic deformation conserves volume, the plastic strains in either of the two transverse directions must be $-\varepsilon^p/2$. When the temperature changes by ΔT, after yielding, the strains in the metal change by

$$\Delta\varepsilon_L^m = \alpha_m \Delta T + \Delta\varepsilon^p + \frac{1-2\nu_m}{E_m}\Delta\sigma_T, \quad (115)$$

$$\Delta\varepsilon_\theta^m = \alpha_m \Delta T - \frac{1}{2}\Delta\varepsilon^p + \frac{1-2\nu_m}{E_m}\Delta\sigma_T. \quad (116)$$

The metal and the dielectric are bonded, so that $\Delta\varepsilon_L^d = \Delta\varepsilon_L^m$ and $\Delta\varepsilon_\theta^d = \Delta\varepsilon_\theta^m$. Solving for the transverse stress, we obtain that

$$\Delta\sigma_T = -\frac{3(\alpha_m - \alpha_d)\Delta T}{3(1-2\nu_m)/E_m + 2(1+\nu_d)/E_d}. \quad (117)$$

Note that this expression can be written as $\Delta\sigma_T = -3B(\alpha_m - \alpha_d)\Delta T$, with the effective elastic modulus given by (96).

SX0730 Figure 45 sketches the stress buildup as the temperature drops from the stress-free temperature T_0. When the temperature is above a certain level, T_e, the metal is elastic, and the stresses increase according to (110) and (111). The temperature T_e is determined by inserting the stresses (110) and (111) into the yield condition (114), giving

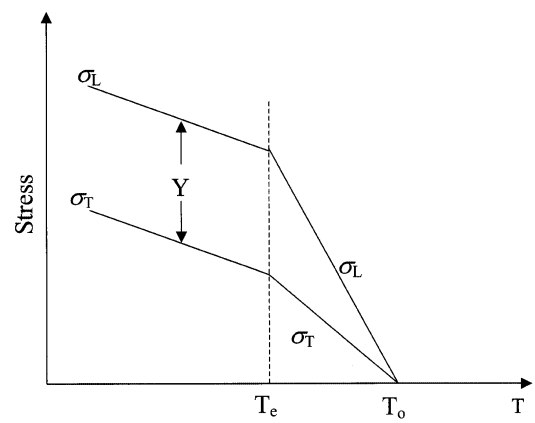

Figure 45 The stresses build up as the temperature drops.

$$\frac{E_m(\alpha_m - \alpha_d)(T_0 - T_e)}{Y} = 1 + \frac{E_d(1+\nu_m)(1-2\nu_m)}{E_m(1+\nu_d)}. \tag{118}$$

At T_e, the transverse stress is

$$\sigma_T(T_e) = \frac{E_d(1+\nu_m)}{E_m(1+\nu_d)}Y, \tag{119}$$

and the longitudinal stress is at a level Y above the transverse stress. As the temperature drops below T_e, the stresses continue to build up, now with a different slope, given by (117).

SX0735 Figure 46 sketches the longitudinal stress as a function of temperature, assuming the metal to be elastic, or liquid-like, or elastic–plastic. At a given temperature below T_0, the elastic metal acquires a high stress, and the liquid-like metal acquires a low stress. The stress in the elastic–plastic metal falls between the two limits. Because we assume that the yield strength Y is a constant, the two lines for the plastic and liquid-like metals are parallel. The longitudinal stress in the elastic–plastic metal line at temperature T is

$$\sigma_L(T) = 3B(\alpha_m - \alpha_d)(T_0 - T) + \left[1 + \frac{E_d(1+\nu_m)}{E_m(1+\nu_d)}\right]Y. \tag{120}$$

The first term is the hydrostatic tension in a liquid-like metal. The second term is due to the presence of the yield strength. A representative value of the yield strength at 200°C is 150 MPa, which contributes significantly to the stress in the metal line.

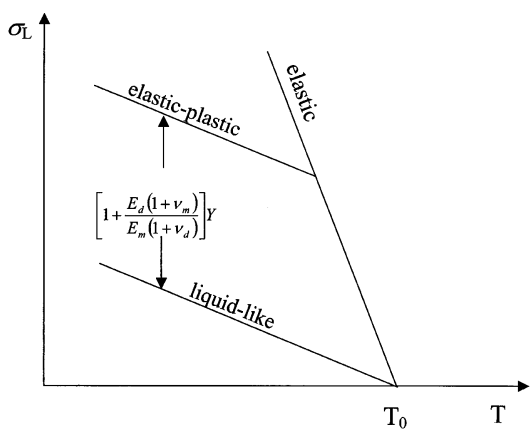

Figure 46 Compare stress in three cases: elastic metal, liquid-like metal, and elastic–plastic metal.

8.7.5.4 Voiding in Blanket Copper Film

bib109 Shaw *et al.* (2001) and bib107 Sekiguchi *et al.* (2001) have observed voids in blanket copper films. In the experiment of Shaw *et al.*, sketched in Figure 47, the copper film was plated on SiO_2 dielectric, and capped with a SiN layer. An annealing at 400°C closed all the voids, and left the copper film under compression. The film was then rapidly cooled and held at 200°C for 2 h; voids grew at the copper/nitride interface. SX0740

Recall that SIV has been widely reported for encapsulated narrow aluminum lines, but not for blanket aluminum films. As illustrated in Figure 48(a), in a blanket metal film, creep can also relieve the biaxial stress by dislocation motion and atomic diffusion. Consequently, voiding (Figure 48(b)) must be regarded as a stress-relieving process in competition with creep. For a void to initiate from a small flaw, the stress must be high enough to compete with the surface energy. The wafer curvature measurements have indicated that the stress in copper is typically higher than in aluminum, due mainly to the larger yield strength in copper films (bib9 Baker *et al.*, 2001; bib110 Shen *et al.*, 1998). Furthermore, the elastic stiffness for copper is more anisotropic than aluminum. For a crystal of cubic symmetry, a SX0745

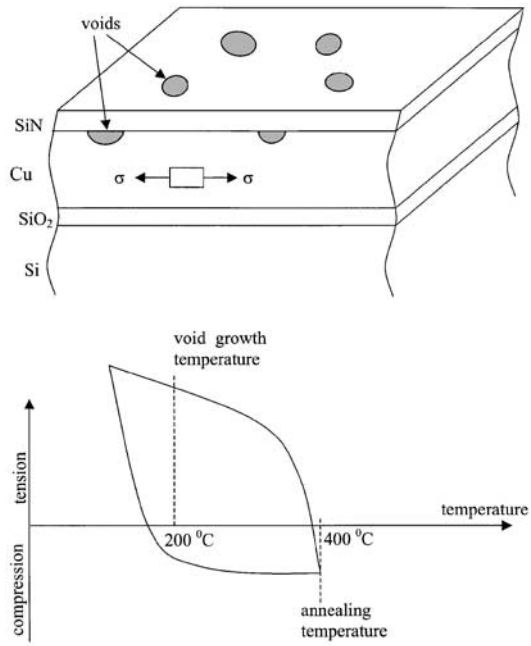

Figure 47 When a blanket copper film under tension is held at an elevated temperature, voids grow on the copper/nitride interface to relax the stress in the copper film. Also sketched is the stress in the copper film as the temperature cycles.

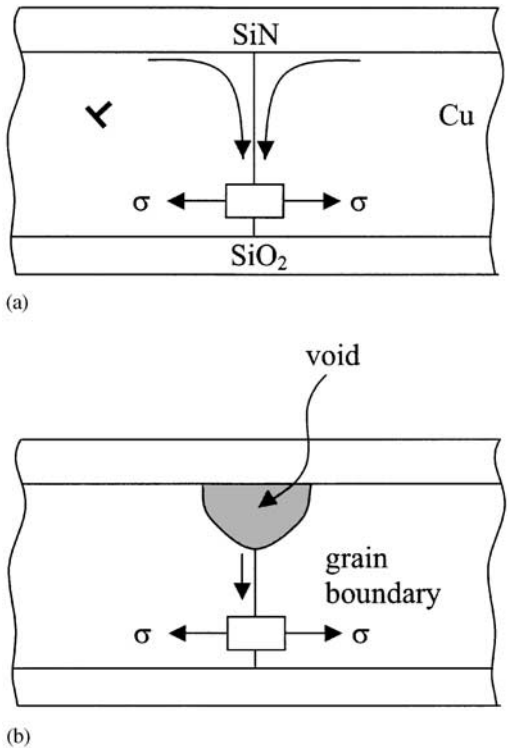

Figure 48 Two processes to relieve stress in copper film: (a) creep and (b) voiding.

single number characterizes the degree of elastic anisotropy:

$$\xi = \frac{C_{12} + 2C_{44}}{C_{11}}. \qquad (121)$$

For an isotropic elastic solid, $\xi = 1$. Using the elastic constants listed in Section 8.7.5.2, one finds that $\xi = 1.1$ for aluminum, and $\xi = 1.6$ for copper. Finite element calculation has shown that the stress is high at the intersection of copper grain boundary and SiN cap layer (X. H. Liu, IBM, private communication).

AU:6
SX0750

For the void to grow in size, atoms must diffuse from the void surface and plate on copper grain boundaries. The observation of voiding implies that creep is a less effective process to relieve the stress. This may be understood by comparing Figures 48(a) and (b). Assume that dislocations motions are constrained in the small volume. To relieve the stress in the copper film, both creep and voiding require atoms to diffuse on the copper grain boundaries. In addition, creep requires that atoms diffuse on the copper/silica or copper/nitride interface, but voiding requires that atoms diffuse on the void surface. If the interface diffusion is slower than the surface diffusion, and if the grain boundary diffusion is not too much faster than the interface diffusion, then voiding will be a more effective means to relieve stress than creep. After a long enough time, allowing atoms to diffuse on the interfaces, voids should disappear, driven by the surface energy, much like in powder sintering. Models of grain boundary diffusion in elastic solids (bib126 Thouless *et al.*, 1996; bib35 Gao *et al.*, 1999) can be adapted to model this phenomenon.

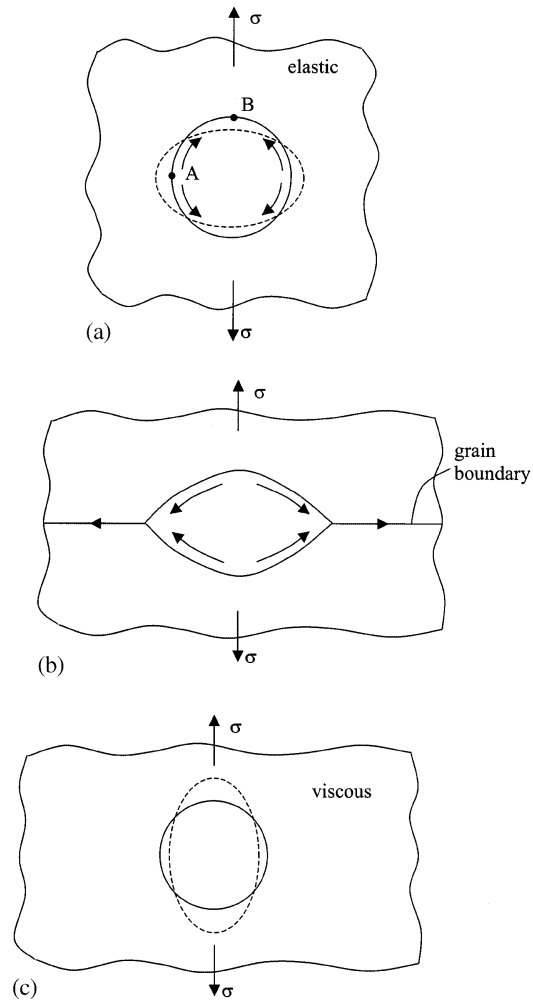

Figure 49 A void changes its shape (a) in an elastic solid, (b) on a grain boundary, and (c) in a viscous solid.

8.7.5.5 Slit-like Voids

As illustrated in Figure 37, voids in an interconnect can have different shapes. A slit-like void significantly increases electric resistance with a small amount of mass transport, and therefore may be responsible for earlier failure. Models of void shapes are briefly considered here. Figure 49(a) illustrates a void of radius a in a crystal under remote stress σ.

SX0755

For simplicity, we will only consider the uniaxial stress state. Assume that atomic transport inside the solid is much slower than on the void surface, so that the void can change shape as atoms relocate on its surface, and the solid is elastic. The surface energy favors a rounded void, but the elastic energy favors an elongated void. The stress at point A is higher than that at B, motivating atoms to diffuse on the surface. The relative importance of the elastic and the surface energy variations is expressed as a dimensionless number (bib116 Sun *et al.*, 1994):

$$\Lambda = \frac{\sigma^2 a}{E\gamma}. \tag{122}$$

Under no stress, the void has a rounded shape maintained by the surface energy. When the crystal is under stress, two behaviors are expected. If the stress is small (Λ small), the void reaches an equilibrium shape close to an ellipse. If the stress is large (Λ larger), the void can never reach equilibrium; noses emerge and sharpen into crack tips. The critical value occurs at $\Lambda_c \approx 1$. Taking $\sigma = 1\,\text{GPa}$, $a = 100\,\text{nm}$, $E = 70\,\text{GPa}$, and $\gamma = 1\,\text{J m}^{-2}$, we find from (122) that $\Lambda = 1.4$. The mechanism operates only under very large stress.

SX0760 To place this mechanism into perspective, recall other mass transport mechanisms by which a void evolves. At elevated temperatures, surface tension and stress may relocate mass by diffusion on a surface and a grain boundary, and by diffusion and creep in a crystal lattice. First consider diffusion on surfaces and boundaries (Figure 49(b)). A void on a grain boundary normal to an applied tensile stress grows as atoms diffuse from the pore surface into the grain boundary (bib22 Chuang *et al.*, 1979). When atoms diffuse faster on the grain boundary than on the void surface, the void cannot maintain the shape of spherical caps, and will become slit-like. Inserting one atom to the grain boundary, the tensile stress does work an amount given by $\Omega\sigma$. The elastic energy variation per atom relocation scales with $\Omega\sigma^2/Y$. When atoms are mobile on the grain boundary, and the grains can drift relative to each other to accommodate the space, the elastic energy variation is much smaller than the work done by the stress associated with the insertion of atoms, $\Omega\sigma^2/Y \ll \Omega\sigma$. The effect of elasticity of the grains is negligible: the models assume rigid grains. However, when the grain boundary is absent, or atoms are immobile on the grain boundary, the tensile stress cannot do work, $\Omega\sigma$, and the elastic energy variation may become important.

SX0765 Next consider a single crystal under a uniaxial tension. A void in the crystal may change shape for several reasons. Elastic distortion causes small changes; large changes require mass transport. As illustrated in Figure 49(c), if the crystal creeps rapidly, the void elongates in the longitudinal direction (e.g., bib18 Budiansky *et al.*, 1982). By contrast, if atoms diffuse rapidly on the void surface and the crystal is elastic, the void elongates in the transverse direction.

8.7.5.6 The Effects of Low-k Dielectrics and Barriers

SX0770 A low-k dielectric often has a small elastic modulus and a large thermal expansion coefficient. For example, SiLK has Young's modulus 2.45 GPa and thermal expansion coefficient $66 \times 10^{-6}\,\text{K}^{-1}$ (bib88 Martin *et al.*, 2000). Will the metal line be under compression on cooling from the fabrication temperature? How small are the effective modulus B and the magnitude of the stress? Does the thin barrier layer between the metal and the dielectric play any role? Because different dielectrics will be used in coming years, it is important to have a convenient method to answer the above questions quantitatively (bib84 Ma *et al.*, 1995; bib42 Hau-Riege and Thompson, 2000).

SX0775 Figure 50 illustrates the cross-section of several long metal lines embedded in a dielectric. In calculation, one can set the thermal expansion coefficient of every material by its own value minus α_{Si}. Because the Si substrate is bulky, the structure is under a state of plane strain deformation. The adjacent lines provide stiffness to each other. One can take a unit cell containing a single metal line, and prescribe zero displacement on the cell walls. Similar to Figure 47, remove the metal line from the structure, and leave behind a composite

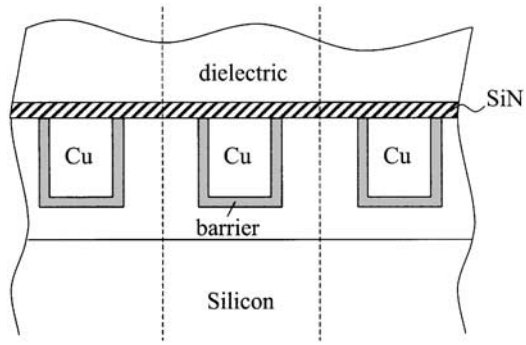

Figure 50 An interconnect structure on a silicon substrate, showing the metal lines, the barriers, and the dielectric.

structure of silicon, the dielectric, and the barrier layer. Apply a uniform normal traction σ on the hole surface, and a temperature change ΔT. The structure is linear elastic, so that the change in the area of the cross-section is linear in the temperature change and the applied stress. Write

$$\frac{1}{A}\int u_n \, \mathrm{d}s = 2\alpha_{\mathrm{eff}} \, \Delta T - \frac{\sigma}{\mu_{\mathrm{eff}}}. \qquad (123)$$

The two coefficients α_{eff} and μ_{eff} can be computed by solving the elasticity boundary value problem. The effective modulus B is still given by (96). The effective thermal expansion mismatch is

$$3\Delta\alpha = 3(\alpha_{\mathrm{m}} - \alpha_{\mathrm{Si}}) - 2\alpha_{\mathrm{eff}}. \qquad (124)$$

When the metal has no voids and is under a hydrostatic stress, the stress is given by $\sigma = 3B\Delta\alpha(T_0 - T)$. When the metal grows voids, and the stress in the metal is fully relieved, the SVV is given by $V_{\mathrm{sv}} = 3\Delta\alpha(T_0 - T)V$. When the dielectric and the barrier have thermal expansion coefficient similar to silicon, $\alpha_{\mathrm{eff}} = 0$, and (124) recovers (92). When the dielectric has a large thermal expansion coefficient, and the barrier is negligibly thin, α_{eff} will dominate (124). On cooling, the metal is under compression.

SX0780 The boundary value problem such as that in Figure 50 is easily solved by using the finite element method. To appreciate the trend, consider an idealized structure similar to that in Figure 44. The metal line has a circular cross-section of radius a, surrounded by a barrier of thickness h_{b}, which in turn is surrounded by an infinite dielectric. This problem can be solved analytically. The effective modulus μ_{eff} relates to the shear modulus of the dielectric and the barrier:

$$\mu_{\mathrm{eff}} = \mu_{\mathrm{d}} + \mu_{\mathrm{b}} h_{\mathrm{b}}/a, \qquad (125)$$

The effective thermal expansion coefficient is

$$\alpha_{\mathrm{eff}} = \frac{\dfrac{\mu_{\mathrm{d}} a}{\mu_{\mathrm{b}} h_{\mathrm{b}}}(1+\nu_{\mathrm{d}})(\alpha_{\mathrm{d}} - \alpha_{\mathrm{Si}}) + (1+\nu_{\mathrm{b}})(\alpha_{\mathrm{b}} - \alpha_{\mathrm{Si}})}{\dfrac{\mu_{\mathrm{d}} a}{\mu_{\mathrm{b}} h_{\mathrm{b}}} + 1}. \qquad (126)$$

When $(\mu_{\mathrm{d}}/\mu_{\mathrm{b}})(a/h_{\mathrm{b}}) \gg 1$, the dielectric prevails: $\mu_{\mathrm{eff}} = \mu_{\mathrm{d}}$ and $\alpha_{\mathrm{eff}} = (1+\nu_{\mathrm{d}})(\alpha_{\mathrm{d}} - \alpha_{\mathrm{Si}})$. When $(\mu_{\mathrm{d}}/\mu_{\mathrm{b}})(a/h_{\mathrm{b}}) \ll 1$, the barrier prevails: $\mu_{\mathrm{eff}} = \mu_{\mathrm{b}} h_{\mathrm{b}}/a$ and $\alpha_{\mathrm{eff}} = (1+\nu_{\mathrm{b}})(\alpha_{\mathrm{b}} - \alpha_{\mathrm{Si}})$. A representative set of magnitudes are $\mu_{\mathrm{d}}/\mu_{\mathrm{b}} = 0.01$, $a/h_{\mathrm{b}} = 10$, $(\mu_{\mathrm{d}}/\mu_{\mathrm{b}})(a/h_{\mathrm{b}}) = 0.1$. When the barrier prevails, the saturation void volume is comparable to that in copper/silica structure. Taking $\mu_{\mathrm{b}} = 60\,\mathrm{GPa}$ and $a/h_{\mathrm{b}} = 10$, we obtain that $\mu_{\mathrm{eff}} = 6.0\,\mathrm{GPa}$. For copper interconnect, the barrier provides the effective modulus $B = 5.7\,\mathrm{GPa}$. Even with a dielectric of negligible stiffness, the barrier itself can provide a significant constraint. This fact has important implications for electromigration resistance, as described in the next section.

8.7.6 ELECTROMIGRATION

In service, an interconnect line carries an SX0785 intense electric current. The current motivates metal atoms to diffuse in the direction of electron flow. The process, known as electromigration, has been the most menacing and persistent threat to interconnect reliability. Before this threat was recognized, electromigration had been one of the curious cross-field transport phenomena, studied for its own sake (e.g., bib59 Huntington and Grone, 1961). The evolution of the electromigration research since the 1970s has been intertwined with that of the interconnect structure; see successive reviews coming out of the IBM T. J. Watson Research Center (bib27 d'Heurle and Rosenberg, 1973; bib26 d'Heurle and Ho, 1978; bib46 Ho and Kwok, 1989; bib51 Hu *et al.*, 1995; bib104 Rosenberg *et al.*, 2000).

Since the early 1990s, as the mechanical SX0790 effect on electromigration is better formulated (bib69 Korhonen *et al.*, 1993), mechanics has become an integral part of the electromigration research. Stress both originates from, and affects, electromigration. There is no fundamental difference between the stress induced by thermal expansion mismatch and that induced by electromigration. Stress may open voids in the metal and break the encapsulation (bib21 Chiras and Clarke, 2000). Low-k dielectrics also have low stiffness, which significantly influences electromigration (Lee *et al.*, 2001; AU:7 bib42 Hau-Riege and Thompson, 2000). As miniaturization continues, the diffusion time will be shorter. At least some of the interconnects will have to be designed to be immortal, on the basis of a stable state, rather than a transient process (bib117 Suo, 1998; bib6 Andleigh *et al.*, 1999).

This section focuses on issues specific to the SX0795 reliability of encapsulated interconnect lines. As of early 2000s, the design of the interconnect structure is in a state of flux. Materials, architectures, and processes will change. Models and experiments based on first principles are particularly valuable in guiding future development. This section draws on the previous ones. In Sections 8.1.7.2 and 8.1.7.3 we consider cracking and debonding caused by

electromigration. Section 8.7.5 considers voiding caused by electromigration. Section 8.7.5.6 is particularly relevant when we consider the effects of low-k dielectrics. Even though Section 8.7.4, which is on ratcheting, dose not come in directly, the conscientious reader will soon feel the pains shared by the two widely used accelerated tests: thermal cycling and electromigration. Similarity will also be found in the models of the two phenomena.

8.7.6.1 Electromigration in Encapsulated Metal Line

SX0800 Figure 51 illustrates an aluminum line encapsulated in a silica dielectric. The tungsten vias link aluminum lines between different levels. The titanium aluminide layers shunt the electric current where voids deplete a segment of aluminum. Figure 52 sketches the stress distribution along the metal line, assuming no voids. As the test temperature, the thermal expansion mismatch induces a triaxial tension in the aluminum line, as discussed in Section 8.7.5. At time $t = 0$, subject the line to a direct electric current. Electrons enter the aluminum line from one tungsten via (cathode), and leave from another (anode). The electron flow causes aluminum atoms to diffuse toward the anode. The atomic transport builds up tension near the cathode, and compression near the anode. The stress gradient promotes atoms to diffuse back to the cathode. After sometime, the interconnect reaches a steady state: the backflow balances the electromigration, and net atomic transport stops. The interconnect will last provided aluminum does not grow voids at cathode, or extrude at the anode.

Next consider the case that the interconnect SX0805 grows voids. Figure 53 summarizes the main observations. Thermal expansion misfit causes a tensile stress in aluminum. Each void grows and relaxes the stress in its vicinity (Figure 53(a)). After the line is subject to an electric current (Figure 53(b)), the voids exhibit extraordinarily complex dynamics: they disappear, re-form, drift, change shape, coalesce, and break up (bib87 Marieb *et al.*, 1995). A particular behavior has captured much attention. A void sometimes takes the shape of a slit, lying inside a single grain, severing the metal line (bib105 Sanchez *et al.*, 1992; bib103 Rose, 1992). bib7 Arzt *et al.* (1994) reported that a void is round initially; it moves, grows, and

Figure 51 A schematic of an interconnect, embedded in a silicon dioxide matrix, on a silicon substrate.

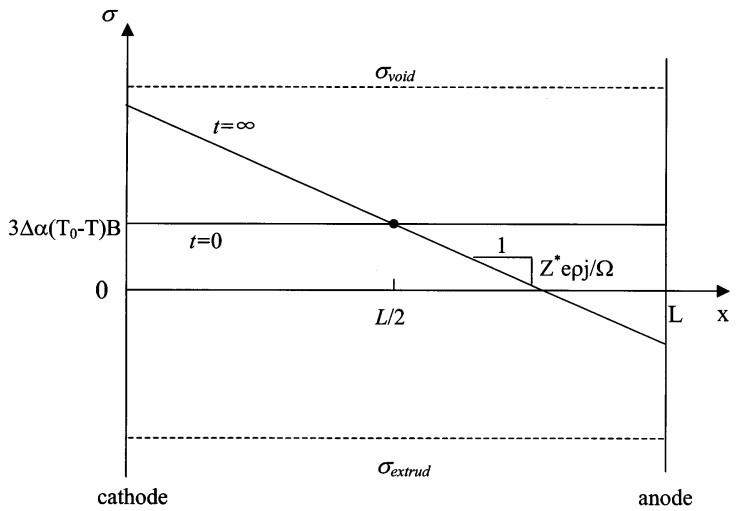

Figure 52 Schematic of the stress field $\sigma(x, t)$ in an encapsulated metal line, assuming no voids.

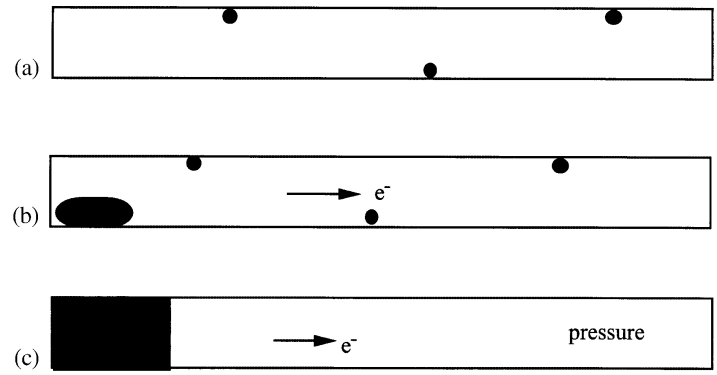

Figure 53 (a) Upon cooling from the processing temperature, voids form to partially relaxed thermal stress. (b) Subject to a current, atoms diffuse toward the anode, and a void grows at the cathode end. (c) The line reaches the stable state, with a single void left at the cathode end, a linear pressure distribution in the rest of the line, and no further mass diffusion.

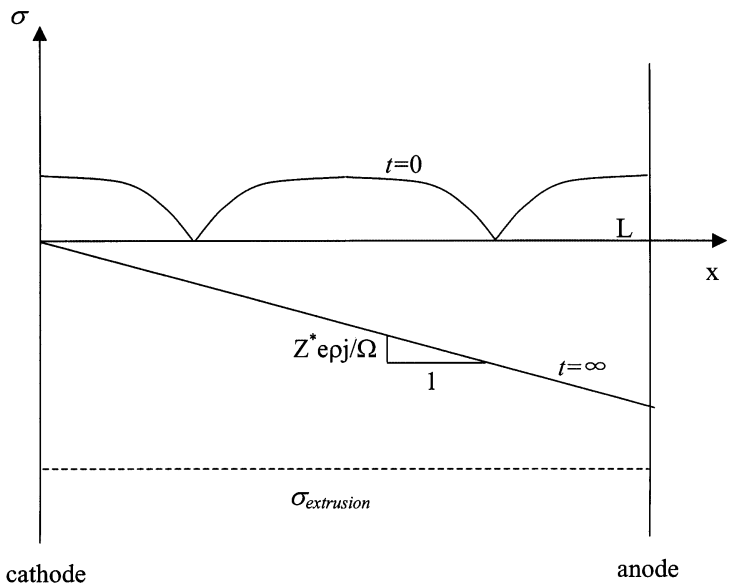

Figure 54 Schematic of the stress field $\sigma(x, t)$ in an encapsulated metal line, assuming that voids grow and move in the line.

then changes shape to become a slit. The void dynamics have been simulated (e.g., bib136 Wang *et al.*, 1996; bib70 Kraft *et al.*, 1997; bib142 Zhang *et al.*, 1999).

SX0810 Despite the commotion in the transient, the end state is simple (bib32 bib33 Filippi *et al.*, 1995, 2002). After a sufficiently long time, the metal line reaches a steady state (Figure 53(c)). Only a single void remains near the cathode; voids in the middle of the line have now been filled or swept into the cathode void. The total number of aluminum atoms is constant in the line. As the void at the cathode grows, atoms diffuse into the rest of the line, inducing a linear distribution of pressure (Figure 54). The pressure gradient balances the electron wind. The metal line behaves like a column of a liquid in the gravitational field. The electron wind playing the role of gravity.

Imagine several identical lines, each carrying SX0815 a different current. Figure 55 illustrates the resistance change as a function of time. The resistance increases as the void enlarges. Two long-term trends are expected: the resistance either saturates or runs away. Evidently, the larger the current, the higher the saturation resistance. For a line carrying a large current, a large pressure gradient is needed to stop mass diffusion. The high pressure in the metal near the anode, in turn, may cause cracking or debonding in the encapsulation materials (bib21 Chiras and Clarke, 2000; bib75 Lee

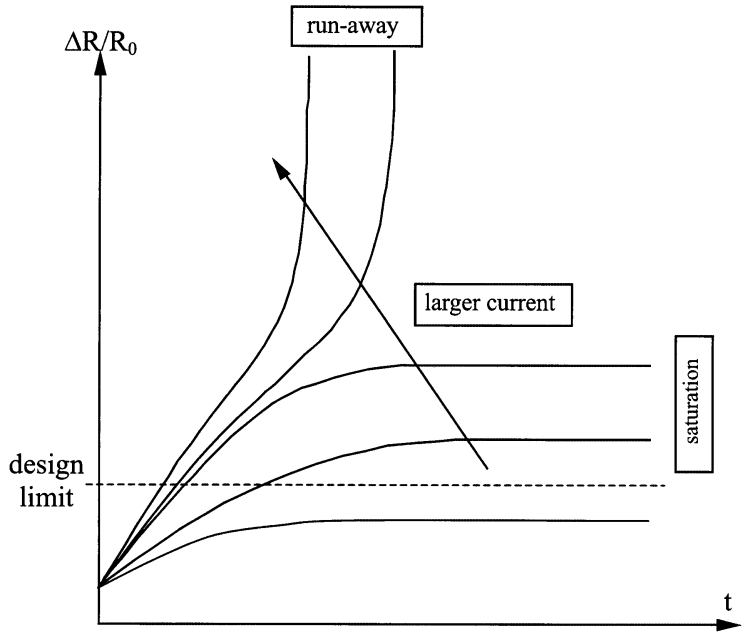

Figure 55 Resistance increases as a function of time. Under a small current, the resistance saturates. Under a large current, the resistance runs away.

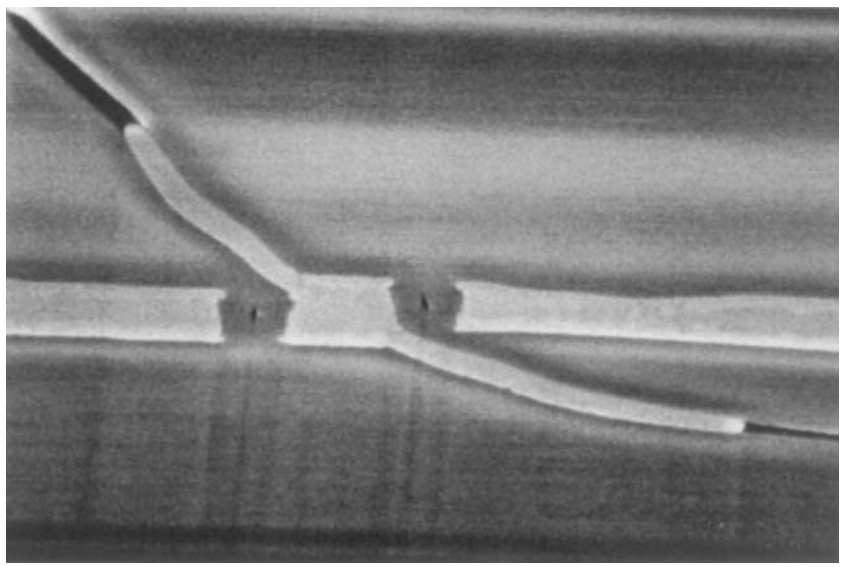

Figure 56 The aluminum line in the middle carries an electrical current in the direction perpendicular to the paper. The pressure in the aluminum line causes the silicon dioxide to crack, and aluminum to extrude (courtesy of W. K. Meyer).

et al., 2002). Afterwards, the metal extrudes and the cathode void grows further, so that the resistance increases indefinitely. Figures 56 and 57 show two examples of extrusion. The interconnect is immortal if a circuit tolerates a variable resistance in an interconnect up to its saturation level.

8.7.6.2 Basic Electromigration Characteristics

(i) Electron Wind

When a direct electric current flows in a metal, the moving electrons impart momentum to metal atoms. The electron wind force per atom, f_e, is proportional to the electric current

SX0820

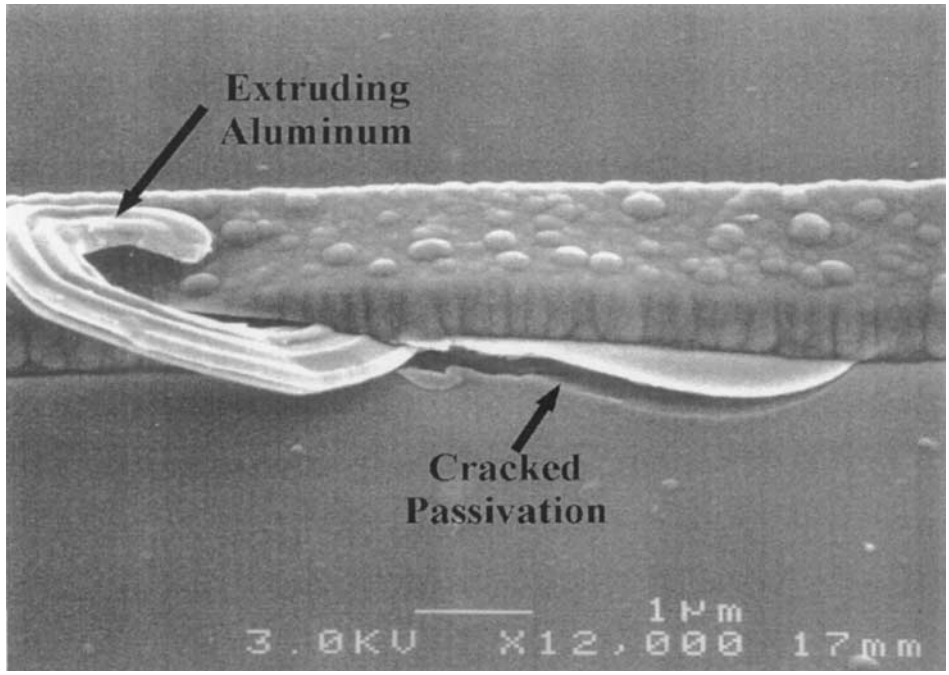

Figure 57 Extrusion from an encapsulated aluminum line (courtesy of S. Chiras and D. R. Clarke).

density j. Write (bib59 Huntington and Grone, 1961)

$$f_e = Z^* e\rho j, \tag{127}$$

where e is the electronic charge, and ρ the resistivity of the metal. Recall that ρj is the electric field in the metal line, and $e\rho j$ has the dimension of force. The dimensionless number Z^* is known as the effective charge number. The sign convention makes $Z^* < 0$, because the electron wind force is in the direction of the electron flow, opposite to that of the electric current density j.

SX0825 The electron wind force is small. When an atom moves by an atomic distance b, the work done by the force, $f_e b$, is much below the average thermal energy kT. Taking representative values $b = 10^{-10}$ m, $Z^* = -2$, $\rho = 3 \times 10^{-8}\,\Omega$m, $j = 10^{10}\,\mathrm{Am}^{-2}$, we find that $f_e b = 5 \times 10^{-8}$ eV. The average thermal energy is $kT = 0.04$ eV at 500 K. Recall that the energy barrier for atomic motion in metals is on the order of 1 eV. Consequently, the electron wind causes metal atoms to diffuse. The atomic flux is linearly proportional to the electron wind force.

(ii) Atomic Diffusion

SX0830 Einstein's equation relates the atomic flux J (i.e., the number of atoms crossing unit area per unit time) to the electron wind force:

$$J = \frac{DZ^* e\rho j}{\Omega kT}, \tag{128}$$

where $D = D_0 \exp(-Q/kT)$ is the diffusion coefficient, Q is the activation energy, and Ω is the volume per atom in the metal. The equation is analogous to Equation (100) for diffusion motivated by the stress gradient.

In a metal line, atoms may diffuse along SX0835 several paths: the bulk crystal, the grain boundaries, the interface between the metal and the encapsulation, and the interface between the metal and the native oxide. Figure 58(a) sketches the cross-section of a wide metal line, width w, and thickness h. The metal line has columnar grains of diameter d. The effective Z^*D, which enters (128) to give the total atomic flux, results from all three kinds of paths (bib52 Hu *et al.*, 1999):

$$Z^* D = Z^*_B D_B + Z^*_G D_G \delta_G \frac{1}{d}\left(1 - \frac{d}{w}\right) + 2Z^*_I D_I \delta_I \left(\frac{1}{w} + \frac{1}{h}\right), \tag{129}$$

where the subscripts B, G, and I signify the bulk, the grain boundary, and the interface; δ_G and δ_I are the width of the grain boundary and the interface, respectively. The melting temperatures of aluminum and copper are 933 K and 1358 K, respectively. The temperatures at which electromigration is of concern are below 500 K. For fine metal lines, bulk diffusion is

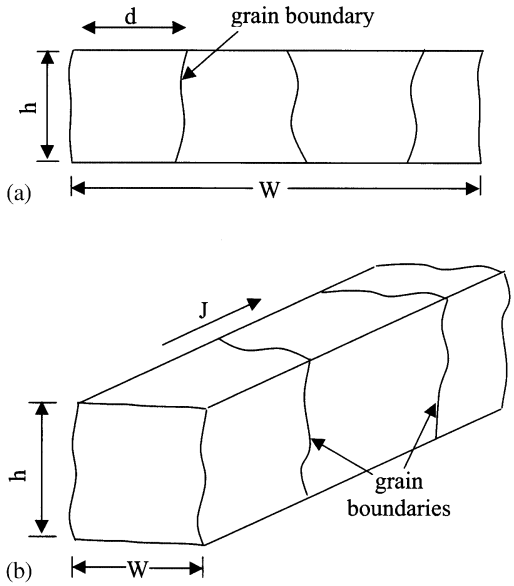

Figure 58 (a) The cross-section of a wide metal line. (b) A narrow line with a bamboo grain structure.

negligible. When a metal line is narrow, the grains form a bamboo structure, with all the grain boundaries perpendicular to the flux direction (Figure 58(b)). For such a bamboo line, the grain boundaries do not contribute to the mass transport; the only remaining diffusion path is the interfaces. As miniaturization continues, a large fraction of atoms will be on the interfaces, so that the effective diffusivity will increase (Equation (129)).

(iii) Median Time-to-Failure

SX0840 The most widely used method to characterize electromigration is to measure the median time-to-failure (MTF). Subject a batch of lines to a known current density and temperature. The lines grow voids. When a void severs a line, the current stops and the line fails. Due to the statistical nature of void formation, failure times scatter even for a batch of carefully processed lines. The MTF is taken as the time at which 50% of the lines have failed. In the interconnect structure with shunt layers, voids never stop the current. A line is taken to have failed when the resistance increases by, say, 20%.

SX0845 MTF measurements provide a convenient way to evaluate effects of various parameters on electromigration. For example, it has been shown that Al lines containing a few percent of Cu last about 80 times longer than pure Al lines (bib5 Ames *et al.*, 1970), that intermetallic shunts greatly increase electromigration resistance (bib48 Howard *et al.*, 1978), that narrow Al lines of bamboo grain structures last longer than polycrystalline wide Al films (bib129 Vaidya *et al.*, 1980), and that Cu lines last longer than Al lines (bib104 Rosenberg *et al.*, 2000).

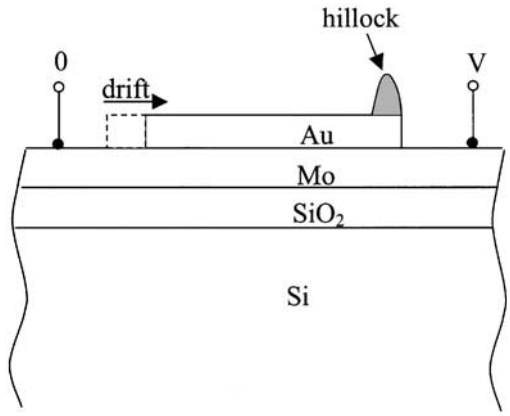

Figure 59 Schematic of the edge drift experiment.

To fail lines within a time suitable for SX0850 laboratory measurements, one has to accelerate the test by using temperatures and electric current densities higher than those used in service. The MFT can be measured for several temperatures and current densities. The results are fit to an empirical relation (bib13 Black, 1969):

$$\mathrm{MFT} = Aj^{-n}\exp\left(\frac{Q}{kT}\right), \qquad (130)$$

where A, n, and Q are fitting parameters. The exponent n typically ranges between 1 and 2. The activation energy Q determined in this way is consistent with that determined by other methods.

The use of MFT to project service lifetime SX0855 raises at least two objections. First, the values of MFT are measured under accelerated conditions. Any conclusion drawn by extrapolation to the service condition is suspect. Second, the interconnect structure has little redundancy. The whole structure fails by the earliest failure of a small number of lines. Valid measurements of the low-percentage-failure tail of the time-to-failure curve involve large numbers of samples (bib34 Gall *et al.*, 2001).

(iv) Line Edge Drift

Another useful experiment involves line edge SX0860 drift. In their original experiment, bib15 Blech and Kinsbron (1975) deposited a gold film on a molybdenum film, which in turn was deposited on an oxide-covered silicon wafer (Figure 59). Molybdenum served as the electrodes. Because

molybdenum has much higher resistance than gold, in the molybdenum/gold bilayer, the electric current mainly flew in gold. Gold atoms diffused in the direction of the electron flow. The edge of the gold film at the cathode drifted, and atoms piled up at anode edge. The edge of the gold film drifted at a constant velocity at a given current and temperature.

SX0865 The drift velocity v relates to the atomic flux as $v = \Omega J$. Using (128), one expresses the drift velocity as

$$v = \frac{DZ^* e\rho j}{kT}. \tag{131}$$

Rewrite the above equation as

$$\ln\left(\frac{vT}{j}\right) = \ln\left(\frac{D_0 Z^* e\rho}{k}\right) - \frac{Q}{kT}. \tag{132}$$

It is convenient to plot the experimentally measured $\ln(vT/j)$ as a function of $1/T$. The data points often fall on a straight line. The slope of the line determines the activation energy Q, and the intercept determines the product D_0Z^*. An additional independent experiment is needed to separate D_0 and Z^*. We will discuss such experiments later.

SX0870 Compared to the MTF measurements, the drift velocity measurements require the observation of the edge displacement. In return, the drift velocity measurements provide the values of D_0Z^*. Furthermore, the drift velocity does not have the large statistical scatter associated with void formation. In principle, a single sample can be used to measure the drift velocities at various temperatures. Such measurements are sufficient to determine Q and D_0Z^*.

SX0875 The drift experiment has been used to determine the dominant diffusion paths for aluminum (bib53 Hu *et al.*, 1993) and copper (bib52 Hu *et al.*, 1999; bib81 Liniger *et al.*, 2002). It has been used to study alloying effects in copper lines (bib76 Lee *et al.*, 1995). The drift experiment led bib14 Blech (1976) himself to discover a quantitative mechanical effect on electromigration. This landmark discovery has since become a guiding light in the interconnect structure design and electromigration research. The remainder of the section describes this discovery and its consequences.

8.7.6.3 Balancing Electron Wind with Stress Gradient

SX0880 On measuring the drift velocity in an aluminum line, bib14 Blech (1976) found that the line edge drifted only when the current density was above a threshold value. He tested lines between 30 μm and 150 μm long. The threshold current density was inversely proportional to the line length. The product of the line length L and the threshold current density j_c was a constant, $j_cL = 1.26 \times 10^5$ A m^{-1}. The j_cL product increased when the aluminum lines were encapsulated in SiN. Blech attributed the observations to the pressure buildup near the anode. The pressure buildup in aluminum was evident as it sometimes cracked the overlying SiN. The pressure also caused a long aluminum extrusion through a hole etched in the SiN near the anode.

SX0885 Blech used aluminum lines 25 μm wide and 0.46 μm thick, with columnar grains. Such wide films could develop biaxial stresses, but not triaxial stresses. Atoms left the cathode region, where tension arose. Atoms arrived in the anode region, where compression built up. At a point in the line, atoms diffuse along the grain boundaries to equalize the two in-plane stress components. The in-plane stresses could not be readily relaxed because diffusion on the aluminum–oxide interfaces is negligible. The stress gradient drove atoms to diffuse from the anode (in compression) to cathode (in tension). The direction was opposite to the electron wind. When the stress gradient balanced the electron wind, net atomic diffusion stopped. Incidentally, bib15 Blech and Kinsbron (1975) did not report any threshold current density for gold lines. Presumably, diffusion on gold surface was so fast that the gold film could not build up significant stresses during the electromigration experiment.

SX0890 Denote the equal biaxial stress by σ, which is a function of the position x along the line and time t. An atom in the metal line is subject to both the electron wind and the stress gradient. The net force is the sum of (99) and (127), namely,

$$f = Z^* e\rho j + \Omega \frac{\partial \sigma}{\partial x}. \tag{133}$$

The evolution of the stress field $\sigma(x, t)$ will be discussed later. We now focus on the steady state. After a sufficiently long time, the net atomic diffusion stops, and the net driving force vanishes, $f = 0$. From (133), the line reaches the steady state when the stress in the line has a constant slope, so that the stress needed to balance the electron wind force is

$$\Omega \Delta\sigma = Z^* e\rho j L, \tag{134}$$

where $\Delta\sigma$ is the stress difference between the two ends of the line. For a very small current, the steady stress $\Delta\sigma$ is small. Wide aluminum lines have finite yield strength, which has been determined by the wafer curvature measurements (bib95 Nix, 1989). The lines drift when

the stresses at both ends exceed the yield strength. Take $\Omega = 1.66 \times 10^{-29}\,\mathrm{m}^3$, $Z^* = -2$, $\rho = 3 \times 10^{-8}\,\Omega\mathrm{m}$, $\Delta\sigma = 10^8\,\mathrm{Pa}$, and we find that $j_c L = 1.73 \times 10^5\,\mathrm{Am}^{-1}$.

SX0895 The mechanical constraint effect on electromigration lifetime had been reported before Blech's work. For example, bib1 Ainslie *et al.* (1972) developed Equation (134) to estimate the stress needed to stop electromigration. These authors used a value $Z^* = -60$ in their estimate, and found an extremely large stress, which could not be sustained by the encapsulation. They abandoned this interpretation, and instead tried to explain the mechanical effect in terms of the effect of stress on diffusivity. The Blech experiment eliminated any diffusivity-related interpretation, because diffusion stopped when the current was below the threshold. Indeed, once the threshold current is measured, together with the yield strength measured by the wafer curvature method, Equation (134) determines the value of Z^*, without being convoluted with the diffusivity.

8.7.6.4 No-Voiding Condition for Encapsulated Line

SX0900 We now return to Figure 52 for a quantitative discussion. On cooling from the stress-free temperature T_0 to a temperature T, the metal line and the encapsulation have a mismatch volumetric strain $3\Delta\alpha(T_0 - T)$. When the structure is held at T for a sufficiently long time, the line will evolve into one of the two equilibrium states: either a uniform hydrostatic stress state $\sigma = 3\Delta\alpha(T_0 - T)B$ with no voids, or a stress-free state with a saturated void volume, $\mathrm{SVV} = 3\Delta\alpha(T_0 - T)V$. Here V is the volume of the metal line. Section 8.7.5.6 prescribes ways to calculate the effective thermal expansion coefficient mismatch $\Delta\alpha$ and elastic modulus B. The evolution is facilitated by atomic transport. At a finite time, the metal line is in a transient state. The stress state is nonhydrostatic and nonuniform. Voids and unrelaxed metal coexist.

SX0905 Of the two equilibrium states, the hydrostatic state is metastable, but the state with SVV is stable. Consider the hydrostatic state first. In Figure 52, this hydrostatic stress field is labeled as $t = 0$. Section 8.7.5.2 prescribes a critical stress for void initiation, $\sigma_{\mathrm{void}} = 2\gamma/a$, where a is the radius of the pre-existing flaw size, and γ the surface energy. The condition can be modified for flaws on interfaces, or junctions between the grain boundaries and the interfaces. It is assumed that the annealing will close all voids provided the uniform hydrostatic stress is below the critical stress, $\sigma < \sigma_{\mathrm{void}}$. For a copper/low-$k$ structure, taking $\Delta\alpha = 13 \times 10^{-6}\,\mathrm{K}^{-1}$, $T_0 - T = 200\,\mathrm{K}$, $B = 6 \times 10^9\,\mathrm{Pa}$, $\gamma = 1\,\mathrm{Jm}^{-2}$ and $a = 5\,\mathrm{nm}$, we find that the hydrostatic stress is $\sigma = 0.47 \times 10^8\,\mathrm{Pa}$, and the critical stress is $\sigma_{\mathrm{void}} = 4 \times 10^8\,\mathrm{Pa}$. This comparison seems to suggest that the compliant dielectrics reduce B, making the stress-induced voiding less likely.

The above void initiation condition is overly SX0910 simplistic, and is risky. It assumes an artificial scenario: the metal reaches the hydrostatic state first, and then the flaws start to question themselves whether to enlarge or shrink. In reality, during annealing, the elastic anisotropy between metal grains, as well as the elastic inhomogeneity between the metal and the encapsulation, can momentarily cause very high stresses at various junctions. If atomic transport is slow in relaxing the metal into the hydrostatic state, the high stresses may cause the flaws to grow. The situation is worse than voiding in blanket films discussed in Section 8.7.5.4. A stress-free and void-free blanket film is the stable equilibrium state. By contrast, in an encapsulated metal line, the uniform hydrostatic state is only metastable; the voids, once initiated, will grow until the entire line is stress free. Experiments of bib41 Hau-Riege (2001) showed that voids formed in copper lines even at very small electric current.

With caution, we pursue this risky model SX0915 further, asking whether a superimposed electric current will initiate voiding. After the electric current is applied, the metal line evolves to a steady state, in which the stress is linearly distributed. The number of atoms is conserved in the metal line. If no voids form, atoms lost in the cathode region relocate to the anode region. By symmetry, the middle of the line neither loses nor gains atoms, and remains to have the stress, $\sigma(L/2,\, t) = 3\Delta\alpha(T_0 - T)B$, at all time. The steady stress state as $t \to \infty$ in the line is

$$\sigma(x, \infty) = 3\Delta\alpha(T_0 - T)B - \frac{Z^* e\rho j}{\Omega}\left(x - \frac{L}{2}\right). \quad (136)$$

In Figure 52, this steady state stress field is labeled as $t = \infty$.

We assume that voids do not initiate if the SX0920 steady stress at the cathode is below the critical stress, $\sigma(0, \infty) < \sigma_{\mathrm{void}}$, namely,

$$3\Delta\alpha(T_0 - T)B + \frac{Z^* e\rho}{2\Omega} jL < \sigma_{\mathrm{void}}. \quad (137)$$

Figure 60 sketches this condition on the plane spanned by the temperature T and the product jL. On this plane, Equation (137) is the straight line. Below the straight line, the current density is low and the temperature is high, so voids will

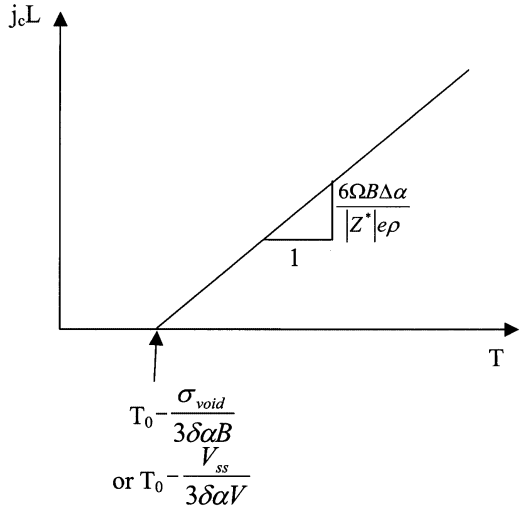

Figure 60 The product j_cL as a function of temperature.

not form. Above the straight line, the void will form.

8.7.6.5 Saturated Void Volume (SVV)

SX0925 A conservative model assumes that the voids grow in the metal line (Figure 53). Figure 54 sketches the stress evolution in such a metal line. Before the line carries the electric current, voids may already grow in the line due to thermal stresses. This stress distribution is labeled as $t=0$ in Figure 54. After the line carries the electric field for sometime, all the voids along the line disappear, and a single void is left in the cathode edge. The void relieves the stress at the cathode, $\sigma(0, t)=0$; the capillary pressure is negligible. The stress at the anode becomes compressive. When the stress gradient balances the electron wind, the stress is linearly distributed along the line:

$$\sigma(x, \infty) = -Z^*e\rho jx/\Omega, \qquad (138)$$

This stress distribution is labeled as $t=\infty$ in Figure 54. The steady stress field is unaffected by the temperature, to the extent that the temperature dependence of the material constants in (138) are negligible. In contrast to the void-free steady state (136), the steady state with a cathode void is stable. No further change will occur in the line until the current density or the temperature changes.

SX0930 The void at the cathode end reaches the saturated volume. The thermal expansion mismatch contributes $3\Delta\alpha(T_0-T)V$ to the SVV. The steady stress field σ contributes $A\int_0^L(\sigma/B)\,dx$ to the SVV, where A is the cross-sectional area of the metal line. Adding the two contributions, the SVV is (bib69 Korhonen *et al.*, 1993; bib117 Suo, 1998)

$$\frac{V_{sv}}{V} = 3\Delta\alpha(T_0 - T) + \frac{Z^*e\rho}{2\Omega B}jL. \qquad (139)$$

The SVV increases when the temperature decreases and the current density increases. The void volume affects the resistance increase, as discussed in Section 8.7.5.2. Failure can be set to the condition that V_{sv}/V reaches a critical value.

On the plane spanned by T and jL, Equation SX0935 (139) appear the same as that shown on Figure 60, but with the intercept replaced by $T_0-(V_{sv}/V)/(3\Delta\alpha)$. The slope of the line is proportional to B. Everything else being equal, j_cL increases with B. In Section 8.7.5.6, we estimated that when the encapsulation changes form Ta/silica to Ta/SiLK, the effective modulus drops by about a factor of 4. Lee *et al.* (2002) have found that $j_cL = 3.7\,\mathrm{A\,m^{-1}}$ and $1.2\times10^5\,\mathrm{A\,m^{-1}}$ for the two kinds structures, respectively.

When the temperature drops, the thermal SX0940 stress increases, and the critical current density decreases. The slope of the straight line in Figure 60 is $6\Omega B\Delta\alpha/|Z^*e\rho|$. An estimate gives the value of this slope to be $2\times10^3\,\mathrm{A\,m^{-1}\,K^{-1}}$. That is, decreasing the temperature by 100 K, one expects a decrease of the j_cL product by $2\times10^5\,\mathrm{A\,m^{-1}}$. This decrease may be of practical concern, because j_cL is measured at an elevated temperature in an accelerated test, and is often reported without qualification. I am unaware of any experimental support for this trend. Incidentally, in bib14 Blech's (1976) drift experiment, j_cL *increased* as the temperature dropped from 500 K to 200 K. He used wide aluminum lines. The high values of j_cL at low temperatures should be due to the corresponding high yield strength.

In writing (139), we have ignored the volume SX0945 change due to the chemical reaction between aluminum and titanium. Any volume *expansion* associated with such a reaction would reduce the saturation void volume. Similarly, encapsulation materials leading to a small or even negative $\Delta\alpha$ will reduce the SVV.

The copper interconnect structures in use SX0950 have very thin barrier layers. They are ineffective as shunts: the resistance abruptly increases when a void at the cathode grows across the via (bib41 Hau-Riege, 2001; bib135 Wang and Filippi, 2001). A more appropriate failure criterion should be the void volume V_{sv} itself, rather than the volumetric strain V_{sv}/V, reaching a critical value. Neglecting the thermal strain in (139), one finds that $V_{sv}\propto jL^2/B$. bib41 Hau-Riege (2001) has suggested that jL^2/B, instead of jL, be used as a figure of merit. The

void-at-via problem can be mitigated by methods to generate a void off the via, at a location uncritical to the interconnect (bib50 Hu *et al.*, 2001). Of course, it remains an option to provide a low-resistance shunt to the interconnect structure.

8.7.6.6 Experimental Determination of Z^*, $\Delta\alpha(T - T_0)$, B, and D

SX0955 No reliable method exists to compute Z^* from first principles; the parameter is measured experimentally. There has been progress in computing diffusivity D form first principles; however, interconnects have multiple diffusion paths, and computations involving interfaces and grain boundaries are unreliable. Although one can compute $\Delta\alpha$ and B as described in Section 8.7.5.6, it is desirable to measure such important parameters experimentally, especially when input material parameters needed for computation are unreliable. As discussed above, the drift experiment with unpassivated lines gives the product Z^*D. Additional independent experiments are needed to separate them, and to determine B and $\Delta\alpha$.

SX0960 Void in encapsulated metal lines can be observed *in situ* using high-voltage scanning electron microscopy (bib87 Marieb *et al.*, 1995). When the void at the cathode is large enough, its growth can be observed as the displacement of line edge at the cathode, similar to the original bib15 Blech–Kinsbron (1975) drift velocity experiment. Figure 61 plots the SVV as a function of the jL product, as predicted by Equation (139). If the saturation void volume is measured experimentally at several current densities, the slope of the line in Figure 61 determines the ratio Z^*/B, and the intercept gives $3\Delta\alpha(T_0 - T)$.

SX0965 Figure 62 sketches the void volume as a function of time. After the line attains the steady state, one can stop the electric current. The stress gradient in the line will drive atoms to diffuse back, and the void will shrink. The same line can be tested at various current densities and temperatures. Similar to the stress relaxation described in Section 8.7.5.2, the process of approaching steady state is governed by a diffusion equation. Both the electron wind and the pressure gradient drive the atomic flux:

$$J = \frac{D}{\Omega kT}\left(Z^* e\rho j + \Omega \frac{\partial \sigma}{\partial x}\right). \qquad (140)$$

The diffusivity is taken to be an average in the aluminum line. Inserting (140) into (101) leads to the diffusion equation (102) for the stress field $\sigma(x, t)$. The solution to this classical initial-boundary value problem takes the form

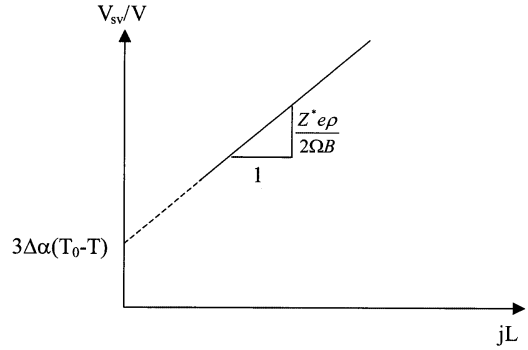

Figure 61 The normalized saturation void volume as a function of the jL product.

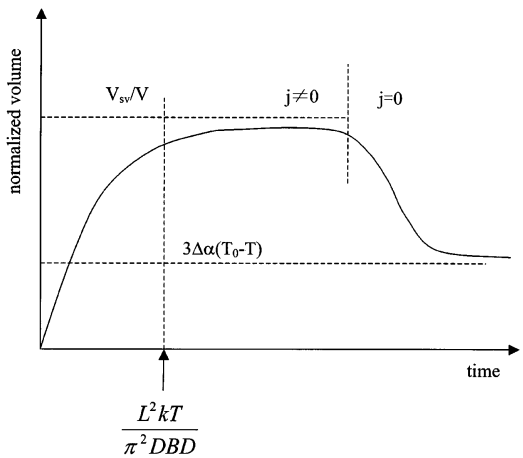

Figure 62 The normalized void volume, as a function of time, first approaches the saturation under a current, and then relaxes to the thermal misfit volume after the current is stopped.

of an infinite series, the slowest decaying term being proportional to $\exp(-t/\tau)$, with

$$\tau = \frac{L^2 kT}{\pi^2 DB\Omega}. \qquad (141)$$

Note that the timescale is independent of the current density. A large current density transports mass at a high rate, but also needs to transport more mass to reach the steady state. An experimental measurement of the relaxation time determines the product DB. In combination with the Z^*/B measured by the saturation volume, and Z^*D by the edge drift of a line with encapsulation of negligible stiffness, one can separate the three parameters Z^*, D, and B.

SX0970 The number Z^* can also be determined, on the basis of the steady stress distribution (138), by measuring the stress in the metal line using synchrotron-based X-ray microdiffraction (bib134 Wang *et al.*, 1998), or by measuring

the fringe stress field in silicon using Raman spectroscopy (bib84 Ma *et al.*, 1995).

8.7.6.7 No-Extrusion Condition for Encapsulated Line

SX0975 In the steady state with SVV, the compressive stress in the metal line at the anode is

$$\sigma_A = -Z^* e \rho j L/\Omega. \tag{142}$$

Using $L = 100\,\mu m$, $j = 1.0 \times 10^{10}\,A m^{-2}$, $Z^* = 2$, $e = 1.6 \times 10^{-19}\,C$, $\rho = 3 \times 10^{8}\,\Omega m$, and $\Omega = 1.66 \times 10^{-29}\,m^3$, one finds that the steady-state compressive stress at the anode is $\sigma_A = -600\,MPa$. The large stress may cause cracking or debonding of the encapsulation. For example, bib32 Filippi *et al.* (1995) tested 100 μm aluminum lines under various current densities, and reported that aluminum did not extrude under $0.56 \times 10^{10}\,A\,m^{-2}$, but did under $1.0 \times 10^{10}\,A\,m^{-2}$.

SX0980 Section 8.7.2.2 has outlined the application of fracture mechanics to structures of small feature size. The fabrication process controls the geometry all the way to the feature size, so that crack-like flaws must be smaller than the feature size. Use the linewidth, w, as a representative size scale, the no-extrusion condition is stated as (bib117 Suo, 1998)

$$\beta \frac{\sigma_A^2 w}{E} < \Gamma, \tag{143}$$

Here Γ is the fracture energy of the encapsulation material or the interface, E the Young's modulus of the material, and β a dimensionless parameter depending on ratios of various elastic moduli and lengths that describe the anode. The values of β can be calculated by solving the elasticity boundary value problems containing cracks. Taking representative values such as $\beta = 0.25$, $\Gamma = 4\,J m^{-2}$, $E = 70\,GPa$, and $w = 0.5\,\mu m$, one finds from (2) that the encapsulation can sustain anode pressure up to $|\sigma_A| = 1.5\,GPa$.

SX0985 In the above, thermal stresses in the passivation have been ignored. Upon cooling from the processing temperature, a large compressive hoop stress arises in the oxide, resulting from the thermal expansion misfits between the aluminum and the oxide, and between the silicon substrate and the oxide. When an electric current is supplied, the volume of aluminum near the anode increases, which first compensates its thermal contraction, and then goes beyond. Consequently, in the stable state, the stress in the oxide is due to the pressure in the aluminum, and the thermal misfit between the oxide and the silicon substrate. The latter is negligible.

SX0990 Two other circumstances should be mentioned in this connection. Some dielectrics may develop large intrinsic stresses at the deposition temperature. They are unrelated to the volume change of aluminum, and persist under temperature change and current. A second circumstance involves a line tested under a current up to the stable state, and then brought to a higher temperature. Instantaneously, the thermal expansion misfit between aluminum and oxide adds more tensile stress in the insulator. In such cases, the additional stresses must be included in the no-extrusion condition.

SX0995 Compliant low-k dielectrics present a new challenge. As a first approximation, we model the Ta barrier as a cylindrical pressure vessel of radius a and thickness h_b, and neglect the dielectric. The hoop stress in the barrier σ_θ relates to the internal pressure σ_A as $\sigma_\theta = |\sigma_A| a / h_b$. Assume that crack-like flaw size is on the order of the barrier thickness h_b. The no-extrusion condition may be written as

$$\beta \frac{\sigma_A^2 a^2}{E h_b} < \Gamma. \tag{144}$$

SX1000 The above estimates are intended to illustrate a basic modeling approach. Because the structural details at line ends are complicated, accurate calculation is difficult. A more reliable method is to carry out experiments with known current density, and use the electromigration generated stress to test the condition for extrusion (bib21 Chiras and Clarke, 2000).

8.7.6.8 The Immortal Interconnect

SX1005 Provided a circuit tolerates a variable resistance in an interconnect up to its saturation level, the interconnect is immortal (bib117 Suo, 1998; bib6 Andleigh *et al.*, 1999). The interconnect evolves into a stable state to adapt to the newly established temperature and current. The immortality gives a simple perspective on reliability. One can focus on the stable state itself, rather than the transient process to reach it. The perspective plays down the roles of the timescale, the rate processes, and the microstructure of the metal. No longer need the microstructure be optimized for slow mass transport or low void nucleation rate. No longer need the MTF be measured, for the lifetime is infinite. No longer need a magic alloy be sought to slow down diffusion rate, for the diffusivity is irrelevant. In short, the reliability is warranted by energetics, rather

than kinetics. Having thermodynamics on our side, the design is much more robust.

SX1010 The use of the stable state is limited in two ways: the metal may extrude at the anode, or the saturation resistance may be prohibitively large. For a short line, the saturation void volume is small compared to the via size, giving rise to a small change in resistance. Consequently, the stable state finds ready applications in short lines. The saturation void volume increases when the effective modulus B is small (Equation (139)). The interconnect structure with low-k dielectrics and thin barriers no doubt require attention. The copper interconnect structures in use have very thin barrier layers. They are ineffective as shunts: the resistance abruptly increases when a void at the cathode grows across the via. An immortal interconnect would require low-resistance shunts.

SX1015 As miniaturization continues, larger fraction of atoms will be on the metal/encapsulation interface. The effective diffusivity will be larger (Equation (129)), and the diffusion time shorter. The day may arrive when some of the interconnects must be *designed* to be immortal. Investigation into ways to limit the resistance increase and to prevent metal extrusion will prepare us for such a day.

ACKNOWLEDGMENTS

SX1016 The work of my group in this area has been supported over the years by the National Science Foundation, Office of Navel Research, Defense Advanced Research Projects Agency, New Jersey Science and Technology Commission, Institute for Materials Research and Engineering, and Intel Corporation. Dr. Z. Y. Huang has kindly helped me prepare the figures.

REFERENCES

bib1 N. G. Ainslie, F. M. d'Heurle and O. C. Wells, 1972, Coating, mechanical constraints, and pressure effects on electromigration. *Appl. Phys. Lett.*, **20**, 173–174.

bib2 P. Alpern, V. Wicher and R. Tilgner, 1994, A simple test chip to assess chip and package design in the case of plastic assembling. *IEEE Trans. Compon. Pack. Manuf. Technol. A*, **17**, 583–589 (correction in 1995, **18**, 862–863).

bib3 J. M. Ambrico and M. R. Begley, 2002, The role of initial flaw size and plasticity in adjacent layers in channeling crack growth in thin films, submitted.

AU:8

bib4 J. M. Ambrico, E. E. Jones and M. R. Begley, 2002, Cracking in thin multi-layers with finite width and periodic architectures. *Int. J. Solids Struct.*, **39**, 1443–1462.

bib5 I. Ames, F. d'Heurle and R. Horstmann, 1970, Reduction of electromigration in aluminum films by copper doping. *IBM J. Res. Develop.*, **14**, 461–463.

bib6 V. K. Andleigh, V. T. Srikar, Y. J. Park and C. V. Thompson, 1999, Mechanism maps for electromigration-induced failure of metal and alloy interconnects. *J. Appl. Phys.*, **86**, 6737–6745.

bib7 E. Arzt, O. Kraft, W. D. Nix and J. E. Sanchez, 1994, Electromigration failure by shape change of voids in bamboo lines. *J. Appl. Phys.*, **76**, 1563–1571.

bib8 A. Bagchi, G. E. Lucus, Z. Suo and A. G. Evans, 1994, A new procedure for measuring the decohesion energy for thin ductile films on substrate. *J. Mater. Res.*, **9**, 1734–1741.

bib9 S. P. Baker, A. Kretschmann and E. Arzt, 2001, Thermomechanical behavior of different texture components in Cu thin films. *Acta Mater.*, **49**, 2145–2160.

bib10 M. R. Begley and A. G. Evans, 2001, Progressive cracking of a multilayer system upon thermal cycling. *J. Appl. Mech.*, **68**, 513–520.

bib11 J. L. Beuth, 1992, Cracking of thin bonded films in residual tension. *Int. J. Solids Struct.*, **29**, 1657–1675.

bib12 J. L. Beuth and N. W. Klingbeil, 1996, Cracking of thin films bonded to elastic–plastic substrates. *J. Mech. Phys. Solids*, **44**, 1411–1428.

bib13 J. R. Black, 1969, Electromigration—a brief survey and some recent results. *IEEE Trans. Electron Devices*, **ED-16**, 338–347.

bib14 I. A. Blech, 1976, Electromigration in thin aluminum films on titanium nitride. *J. Appl. Phys.*, **47**, 1203–1208.

bib15 I. A. Blech and E. Kinsbron, 1975, Electromigration in thin gold films on molybdenum surfaces. *Thin Solid Films*, **25**, 327–334.

bib16 I. A. Blech and E. S. Meieran, 1967, Direct transmission electron microscope observation of electrotransport in aluminum thin films. *Appl. Phys. Lett.*, **11**, 263–265.

bib17 J. Bree, 1967, Elastic–plastic behaviour of thin tubes subjected to internal pressure and intermittent high-heat fluxes with application to fast-nuclear-reactor fuel elements. *J. Strain Analysis*, **2**, 226–238.

bib18 B. Budiansky, J. W. Hutchinson and S. Slutsky, 1982, Void growth and collapse in viscous solids. In: "Mechanics of Solids, The Rodney Hill 60th Anniversary Volume," eds. H. G. Hopkins and J. Sewell, Pergamon Press, Oxford, pp. 13–45.

bib19 H. C. Cao and A. G. Evans, 1989, An experimental study of the fracture resistance of bimaterial interface. *Mech. Mater.*, **7**, 295–305.

bib20 P. G. Charalambides, J. Lund, A. G. Evans and R. M. McMeeking, 1989, A test specimen for determining the fracture resistance of bimaterial interfaces. *J. Appl. Mech.*, **56**, 77–82.

bib21 S. Chiras and D. R. Clarke, 2000, Dielectric cracking produced by electromigration in microelectronic interconnects. *J. Appl. Phys.*, **88**, 6302–6312.

bib22 T.-J. Chuang, K. I. Kagawa, J. R. Rice and L. B. Sills, 1979, Non-equilibrium models for diffusive cavitation of grain interfaces. *Acta Metall.*, **27**, 265–284.

bib23 R. F. Cook and E. G. Liniger, 1999, Stress-corrosion cracking of low-dielectric-constant spin-on-glass thin films. *J. Electochem. Soc.*, **146**, 4439–4448.

bib24 J. Curry, G. Fitzgibbon, Y. Guan, R. Muollo, G. Nelson and A. Thomas, 1984, New failure mechanisms in sputtered aluminum–silicon films. In: "22nd Ann. Proc. IEEE Int. Reliability Phys. Symp.," pp. 6–8.

AU:9

bib25 R. H. Dauskardt, M. Lane, Q. Ma and N. Krishna, 1998, Adhesion and debonding of multi-layer thin film structures. *Eng. Fract. Mech.*, **61**, 141–162.

bib26 F. M. d'Heurle and P. S. Ho, 1978, Electromigration in thin films. In: "Thin Films: Interdiffusion and Reactions," eds. J. Poate, K. N. Tu and J. Mayer, Wiley, New York, pp. 243–303.

bib27 F. M. d'Heurle and R. Rosenberg, 1973, Electromigration in thin films. In: "Physics of Thin Films," eds. G. Hass, M. Francombe and R. Hoffman, Academic Press, New York, vol. 7, pp. 257–310.

bib28 D. R. Edwards, K. G. Heinen, S. K. Groothuis and J. E. Martinez, 1987, Shear-stress evaluation of plastic packages. *IEEE Trans. Compon. Hybrids Manuf. Technol.*, **12**, 618–627.

bib29 F. Erdogan and G. C. Sih, 1963, On the crack extension in plates under plane loading and transverse shear. *J. Basic Eng., Trans. ASME*, **85**, 519–527.

bib30 A. G. Evans, M. D. Drory and M. S. Hu, 1988, The cracking and decohesion of thin films. *J. Mater. Res.*, **3**, 1043–1049.

bib31 A. G. Evans and J. W. Hutchinson, 1995, The thermomechanical integrity of thin films and multilayers. *Acta Metall. Mater.*, **43**, 2507–2530.

bib32 R. G. Filippi, G. A. Biery and R. A. Wachnik, 1995, The electromigration short-length effect in Ti–AlCu–Ti metallization with tungsten studs. *J. Appl. Phys.*, **78**, 3756–3768.

bib33 R. G. Filippi, R. A. Wachnik, C.-P. Eng, D. Chidambarrao, P.-C. Wang, J. F. White, M. A. Korhonen, T. M. Shaw, R. Rosenberg and T. D. Sullivan, 2002, The effect of current density, stripe length, stripe width, and temperature on resistance saturation during electromigration testing. *J. Appl. Phys.*, **91**, 5787–5795.

bib34 M. Gall, C. Capasso, D. Jawaranl, R. Hemandez, H. Kawasaki and P. S. Ho, 2001, Statistical analysis of early failures in electromigration. *J. Appl. Phys.*, **90**, 732–740.

bib35 H. Gao, L. Zhang, W. D. Nix, C. V. Thompson and E. Arzt, 1999, Crack-like grain-boundary diffusion wedges in thin metal films. *Acta Mater.*, **47**, 2865–2878.

bib36 S. A. Gee, M. R. Johnson and K. L. Chen, 1995, A test chip design for detecting thin-film cracking in integrated-circuits. *IEEE Trans. Compon. Pack. Manuf. Technol. B*, **18**, 478–484.

bib37 A. Gouldstone, Y. L. Shen, S. Suresh and C. V. Thompson, 1998, Evolution of stresses in passivated and unpassivated metal interconnects. *J. Mater. Res.*, **13**, 1956–1966.

bib38 B. Greenebaum, A. I. Sauter, P. A. Flinn and W. D. Nix, 1991, Stress in metal lines under passivation—comparison of experiment with finite-element calculations. *Appl. Phys. Lett.*, **58**, 1845–1847.

bib39 C. K. Gurumurthy, J. Jiao, L. G. Norris, C.-Y. Hui and E. J. Kramer, 1998, A thermo-mechanical approach for fatigue testing of polymer bimaterial interfaces. *ASME Trans. J. Electron. Packag.*, **120**, 372–378.

bib40 J. B. Han, 2001, Flip-chip BGA design to avert die cracking. *J. Electron. Packag.*, **123**, 58–63.

bib41 S. P. Hau-Riege, 2001, Immortality of Cu damascene interconnects. In: ''6th International Workshop on Stress-induced Phenomena in Metallization,'' eds. S. P. Baker, M. A. Korhonen, E. Arzt and P. S. Ho, Am. Inst. Phys., pp. 21–32.

bib42 S. P. Hau-Riege and C. V. Thompson, 2000, The effects of the mechanical properties of the confinement material on electromigration in metallic interconnects. **15**, 1797–1802.

bib43 M. Y. He, A. G. Evans and J. W. Hutchinson, 2000, The ratcheting of compressed thermally grown thin films on ductile substrates. *Acta Mater.*, **48**, 2593–2601.

bib44 R. Hill, 1950, ''The Mathematical Theory of Plasticity,'' Clarendon Press, Oxford.

bib45 K. Hinode, I. Asano, T. Ishiba and Y. Homma, 1990, A study on stress-induced migration in aluminum metallization based on direct stress measurements. *J. Vac. Sci. Technol.*, **B8**, 495–498.

bib46 P. S. Ho and T. Kwok, 1989, Electromigration in metals. *Rep. Progr. Phys.*, **52**, 301–347.

bib47 M. Hommel, A. H. Fischer, A. v. Glasow and A. E. Zitzelsberger, 2001, Stress-induced voiding in aluminum and copper interconnects. In: ''6th International Workshop on Stress-induced Phenomena in Metallization,'' eds. S. P. Baker, M. A. Korhonen, E. Arzt and P. S. Ho, Am. Inst. Phys., pp. 157–168.

J. K. Howard, J. F. White and P. S. Ho, 1978, Intermetallic compounds of Al and transitions metals: effect of electromigration in 1−2-μm-wide lines. *J. Appl. Phys.*, **49**, 4083–4093.

bib48

bib49 K. J. Hsia, Z. Suo and W. Yang, 1994, Cleavage due to dislocation confinement in layered materials. *J. Mech. Phys. Solids*, **42**, 877–896.

bib50 C.-K. Hu, L. Gignac, S. G. Malhotra and R. Rosenberg, 2001, Mechanisms for very long electromigration lifetime in dual-damascene Cu interconnections. *Appl. Phys. Lett.*, **78**, 904–906.

bib51 C.-K. Hu, K. P. Rodbell, T. D. Sullivan, K. Y. Lee and D. P. Bouldin, 1995, Electromigration and stress-induced voiding in fine Al and Al-alloy thin-film lines. *IBM J. Res. Develop.*, **39**, 465–497.

bib52 C.-K. Hu, R. Rosenberg and K. Y. Lee, 1999, Electromigration path in Cu thin-film lines. *Appl. Phys. Lett.*, **74**, 2945–2947.

bib53 C.-K. Hu, M. B. Small and P. S. Ho, 1993, Electromigration in Al(Cu) two-level structures: effect of Cu and kinetics of damage formation. *J. Appl. Phys.*, **74**, 969–978.

bib54 M. S. Hu and A. G. Evans, 1989, The cracking and decohesion of thin films on ductile substrates. *Acta Metall.*, **37**, 917–925.

bib55 M. Huang, Z. Suo and Q. Ma, 2001, Metal film crawling in interconnect structures caused by cyclic temperatures. *Acta Mater.*, **49**, 3039–3049.

bib56 M. Huang, Z. Suo and Q. Ma, 2002, Ratcheting induced cracks in thin film structures. *J. Mech. Phys. Solids*, **50**, 1079–1098.

bib57 M. Huang, Z. Suo, Q. Ma and H. Fujimoto, 2000, Thin film cracking and ratcheting caused by temperature cycling. *J. Mater. Res.*, **15**, 1239–1242.

bib58 R. Huang, J. H. Prévost, Z. Y. Huang and Z. Suo, 2003, Channel-cracking of thin films with the extended finite element method, submitted.

AU:14

bib59 H. B. Huntington and A. R. Grone, 1961, Current-induced marker motion in gold wires. *J. Phys. Chem. Solids*, **20**, 76–87.

bib60 J. W. Hutchinson and A. G. Evans, 2000, Mechanics of materials: top-down approaches to fracture. *Acta Mater.*, **48**, 125–135.

bib61 J. W. Hutchinson and Z. Suo, 1991, Mixed-mode cracking in layered materials. *Adv. Appl. Mech.*, **29**, 63–191.

bib62 M. Isagawa, Y. Iwasaki and T. Sutoh, 1980, Deformation of Al metallization in plastic encapsulated semiconductor devices caused by thermal shock. In: ''Proc. Int. Reliability Phys. Symp.,'' pp. 171–177.

AU:15

bib63 S. Jansson and F. A. Leckie, 1992, Mechanical-behavior of a continuous fiber-reinforced aluminum matrix composite subjected to transverse and thermal loading. *J. Mech. Phys. Solids*, **40**, 593–612.

bib64 R. E. Jones and M. L. Basehore, 1987, Stress analysis of encapsulated fine-line aluminum interconnect. *Appl. Phys. Lett.*, **50**, 725–727.

bib65 A. M. Karlsson and A. G. Evans, 2001, A numerical model for the cyclic instability of thermally grown oxides in thermal barrier systems. *Acta Mater.*, **49**, 1793–1804.

bib66 R. R. Keller, J. A. Nucci and D. P. Field, 1997, Local textures and grain boundaries in voided copper interconnects. *J. Electron. Mater.*, **26**, 996–1001.

bib67 S.-Y. Kook and R. H. Dauskardt, 2002, Moisture-assisted subcritical debonding of a polymer/metal interface. *J. Appl. Phys.*, **91**, 1293–1303.

bib68 M. A. Korhonen, R. D. Black and C.-Y. Li, 1991, Stress relaxation of passivated aluminum line metalizations on silicon substrate. *J. Appl. Phys.*, **69**, 1748–1755.

bib69 M. A. Korhonen, P. Borgesen, K. N. Tu and C.-Y. Li, 1993, Microstructure based statistical model of electromigration damage in confined line metallizations in the presence of thermally induced stresses. *J. Appl. Phys.*, **73**, 3790–5004.

bib70 O. Kraft and E. Arzt, 1997, Electromigration mechanisms in conductor lines: void shape changes and slit-like failure. *Acta Mater.*, **45**, 1599–1611.

bib71 M. Lane, R. H. Dauskardt, A. Vainchtein and H. Gao, 2000, Plasticity contributions to interface adhesion in thin film interconnect structures. *J. Mater. Res.*, **15**, AU:16 2758–2769.

bib72 M. Lane, R. H. Dauskardt, N. Krishna and I. Hashim, 2000, Adhesion and reliability of copper interconnects with Ta and TaN barrier layers. *J. Mater. Res.*, **15**, 203–211.

bib73 J. Lau, C. P. Wong, J. L. Prince and W. Nakayama, 1998, "Electronic Packaging, Design, Materials, Process, and Reliability," McGraw-Hill, New York.

bib74 B. Lawn, 1993, "Fracture of Brittle Solids," Cambridge University Press, Cambridge.

bib75 K.-D. Lee, X. Lu, E. T. Ogawa, H. Matsuhashi and P. S. Ho, 2002, Electromigration study of Cu/low k dual-damascene interconnects. In: "40th Ann. Proc. IEEE Int. AU:17 Reliability Phys. Symp.," pp. 322–326.

bib76 K. L. Lee, C.-K. Hu and K. N. Tu, 1995, *In situ* scanning electron microscope comparison studies on electromigration of Cu and Cu(Sn) alloys for advanced chip interconnects. *J. Appl. Phys.*, **78**, 4428–4437.

bib77 F. Z. Li, C. F. Shih and A. Needleman, 1985, A comparison of methods for calculating energy release rates. *Eng. Fract. Mech.*, **21**, 405–421.

bib78 J. Liang, R. Huang, J. H. Prévost and Z. Suo, 2002a, Concomitant thin film cracking and underlayer creep, AU:18 *Exp. Mech.*, submitted.

bib79 J. Liang, R. Huang, J. H. Prévost and Z. Suo, 2002b, Evolving crack patterns in thin films with the extended AU:18 finite element method, *Int. J. Solids Struct.*, submitted.

bib80 K. M. Liechti and Y. S. Chai, 1991, Biaxial loading experiments for determining interfacial fracture-toughness. *J. Appl. Mech.*, **58**, 680–687.

bib81 E. Liniger, L. Gignac, C.-K. Hu and S. Kaldor, 2002, *In situ* study of void growth kinetics in electroplated Cu lines. *J. Appl. Phys.*, **92**, 1803–1810.

bib82 X. H. Liu, Z. Suo, Q. Ma and H. Fujimoto, 2000, Cracking and debonding in integrated circuit structures. *Eng. Fract. Mech.*, **66**, 387–402.

bib83 T. C. Lu, J. Yang, Z. Suo, A. G. Evans, R. Hecht and R. Mehrabian, 1991, Matrix cracking in intermetallic composites caused by thermal expansion mismatch. *Acta Metall. Mater.*, **39**, 1883–1890.

bib84 Q. Ma, S. Chiras, D. R. Clarke and Z. Suo, 1995, High resolution determination of the stress in individual interconnect lines and the variation due to electromigration. *J. Appl. Phys.*, **78**, 1614–1622.

bib85 Q. Ma, J. Xie, S. Chao, S. El-Mansy, R. McFadden and H. Fujimoto, 1998, Channel cracking technique for toughness measurement of brittle dielectric thin films on silicon substrates. *Mater. Res. Soc. Symp. Proc.*, **516**, 331–336.

bib86 S. X. Mao and A. G. Evans, 1997, The influence of blunting on crack growth at oxide/metal interfaces. *Acta Mater.*, **45**, 4263–4270.

bib87 T. Marieb, P. Flinn, J. C. Bravman, D. Gardner and M. Madden, 1995, Observations of electromigration induced void nucleation and growth in polycrystalline and near-bamboo passivated Al lines. *J. Appl. Phys.*, **78**, 1026–1032.

bib88 S. J. Martin, J. P. Godschalx, M. E. Mills, E. O. Shaffer and P. H. Townsend, 2000, Development of a low-dielectric-constant polymer for the fabrication of integrated circuit interconnect. *Adv. Mater.*, **12**, 1769–1778.

bib89 P. P. L. Matos, R. M. McMeeking, P. G. Charalambides and M. D. Drory, 1989, A method for calculating stress intensities in bimaterial fracture. *Int. J. Fract.*, **40**, 235–AU:19 254.

bib90 J. W. McPherson and C. F. Dunn, 1987, A model for stress-induced notching and voiding in very large-scale integrated Al–Si (1%) metalization. *J. Vac. Sci. Techol.*, **B5**, 1321–1325.

bib91 S. Michaelides and S. K. Sitaraman, 1999, Die cracking and reliable die design for flip-chip assemblies. *IEEE Trans. Adv. Packag.*, **22**(4), 602–613.

bib92 N. Moes, J. Dolbow and T. Belytschko, 1999, A finite element method for crack growth without remeshing. *Int. J. Numerical Methods in Eng.*, **46**, 131–150.

bib93 M. Morgen, E. T. Ryan, J.-H. Zhao, C. Hu, T. Cho and P. S. Ho, 1999, Low dielectric constant materials for advanced interconnects. *JOM*, 37–40. AU:20

bib94 A. Needleman and E. Van der Giessen, 2001, Discrete dislocation and continuum descriptions of plastic flow. *Mater. Sci. Eng.*, **A309**, 1–13.

bib95 W. D. Nix, 1989, Mechanical-properties of thin-films. *Metall. Trans.*, **20A**, 2217–2245.

bib96 E. T. Ogawa, J. W. McPherson, J. A. Rosal, K. J. Dickerson, T.-C. Chiu, L. Y. Tsung, M. K. Jain, T. D. Bonifield, J. C. Ondrusek and W. R. McKee, 2002, Stress-induced voiding under vias connected to wide Cu metal leads. Proceedings of 2002 IEEE International Reliability Physics Symposium. AU:21

bib97 T. S. Oh, R. M. Cannon and R. O. Ritchie, 1987, Subcritical crack-growth along ceramic-metal interfaces. *J. Am. Ceram. Soc.*, **70**, C352–C355.

bib98 H. Okabayashi, 1993, Stress-induced void formation in metallization for integrated circuits. *Mater. Sci. Eng.*, **R11**, 191–241.

bib99 T. R. Reid, 1984, "The Chip," Simon & Shuster, New York.

bib100 I. E. Reimanis, B. J. Dalgleish and A. G. Evans, 1991, The fracture-resistance of a model metal ceramic interface. *Acta Metall. Mater.*, **39**, 3133–3141.

bib101 J. R. Rice, 1988, Elastic fracture mechanics concepts for interfacial cracks. *J. Appl. Mech.*, **55**, 98–103.

bib102 J. E. Rim, F. Shi, D.-I. Lee, F. Ohta and R. H. Dauskardt, 2002, Adhesion and debonding of low-k carbon-doped oxide films in multi-layer thin film structures. *J. Mater. Res.*, submitted. AU:22

bib103 J. H. Rose, 1992, Fatal electromigration voids in narrow aluminum–copper interconnect. *Appl. Phys. Lett.*, **61**, 2170–2172.

bib104 R. Rosenberg, D. C. Edelstein, C.-K. Hu and K. P. Rodbell, 2000, Copper metallization for high performance silicon technology. *Ann. Rev. Mater.*, **30**, 229–262.

bib105 J. E. Sanchez, L. T. McKnelly and J. W. Morris, 1992, Slit morphology of electromigration induced open circuit failures in fine line conductors. *J. Appl. Phys.*, **72**, 3201–3203.

bib106 A. I. Sauter and W. D. Nix, 1992, A study of stress-driven diffusive growth of voids in encapsulated interconnect lines. *J. Mater. Res.*, **7**, 1133–1143.

bib107 A. Sekiguchi, J. Koike, S. Kamiya, M. Saka and K. Maruyama, 2001, Void formation by thermal stress concentration at twin interfaces in Cu thin films. *Appl. Phys. Lett.*, **79**, 1264–1266.

bib108 E. O. Shaffer, F. J. Mcgarry and L. Hoang, 1996, Designing reliable polymer coatings. *Polym. Eng. Sci.*, **36**, 2375–2381.

bib109 T. M. Shaw, L. Gignac, X.-H. Liu, R. R. Rosenberg, E. Levine, P. Mclaughlin, P.-C. Wang, S. Greco and G. Biery, 2001, Stress voiding in wide copper lines. In: "6th International Workshop on Stress-induced Phenomena in Metallization," eds. S. P. Baker, M. A. Korhonen, E. Arzt and P. S. Ho, Am. Inst., Phys., pp. 177–183. AU:23

bib110 Y. L. Shen, S. Suresh, M. Y. He, A. Bagchi, O. Kienzle, M. Ruhle and A. G. Evans, 1998, Stress evolution in passivated thin films of Cu on silica substrates. *J. Mater. Res.*, **13**, 1928–1937.

bib111 C. F. Shih, R. J. Asaro and N. P. O'Dowd, 1991, Elastic–plastic analysis of cracks on bimaterial interfaces: 3. Large-scale yielding. *J. Appl. Mech.*, **58**, 450–463.

bib112 J. M. Snodgrass, D. Pantelidis, M. L. Jenkins, J. C. Bravman and R. H. Dauskardt, 2002, Subcritical debonding of polymer/silica interfaces under monotonic
AU:24 and cyclic fatigue loading. *J. Mater. Res.*, submitted.
bib113 E. Suhir, 2002, Accelerated life testing (ALT) in microelectronics and photonics: its role, attributes, challenges, pitfalls, and interaction with qualification tests. *J. Electron. Packag.*, **124**, 281–291.
bib114 T. D. Sullivan, 1996, Stress-induced voiding in microelectron metallization: void growth models and refinements. *Ann. Rev. Mater. Sci.*, **26**, 333–364.
bib115 S. Suresh, 1998, "Fatigue of Materials," 2nd edn, Cambridge University Press, Cambridge.
bib116 B. Sun, Z. Suo and A. G. Evans, 1994, Emergence of crack by mass transport in elastic crystals stressed at high temperatures. *J. Mech. Phys. Solids*, **42**, 1653–1677.
bib117 Z. Suo, 1998, Stable state of interconnect under temperature change and electric current. *Acta Mater.*, **46**, 3725–3732.
bib118 Z. Suo and J. He, 2002, Unpublished research.
bib119 Z. Suo and J. W. Hutchinson, 1989, Sandwich specimens for measuring interface crack toughness. *Mater. Sci. Eng.*, **A107**, 135–143.
bib120 Z. Suo and J. W. Hutchinson, 1990, Interface crack between two elastic layers. *Int. J. Fract.*, **43**, 1–18.
bib121 Z. Suo, C. F. Shih and A. G. Varias, 1993, A theory for cleavage cracking in the presence of plastic flow. *Acta Metall. Mater.*, **41**, 1551–1557.
bib122 H. Tada, P. C. Paris and G. R. Irwin, 1985, "The Stress Analysis of Cracks Handbook," Del Research, St. Louis, MO.
bib123 R. E. Thomas, 1985, Stress-induced deformation of aluminum metallization in plastic molded semiconductor-devices. *IEEE Trans. Compon. Hybrids Manuf. Technol.*, **8**, 427–434.
bib124 M. D. Thouless, 1991, Cracking and delamination of coatings. *J. Vac. Sci. Technol.*, **A9**, 2510–2515.
bib125 M. D. Thouless, A. G. Evans, M. F. Ashby and J. W. Hutchinson, 1987, The edge cracking and spalling of brittle plates. *Acta Metall.*, **35**, 1333–1341.
bib126 M. D. Thouless, H. H. Yu, Z. J. Zhao and W. Yang, 1996, Damage nucleation during electromigration along an isolated interface in an elastic medium. *J. Mech. Phys. Solids*, **44**, 371–387.
bib127 S. P. Timoshenko and J. N. Goodier, 1970, "Theory of
AU:25 Elasticity," McGraw-Hill.
bib128 T. Turner and K. Wendel, 1985, The influence of stress on aluminum conductor life. In: "23rd Ann. Proc. IEEE Int. Reliability Phys. Symp.," pp. 142–147.
AU:26
bib129 S. Vaidya, T. T. Sheng and A. K. Sinha, 1980, Linewidth dependence of electromigration in evaporated Al-0.5%Cu. *Appl. Phys. Lett.*, **36**, 464–466.
bib130 A. G. Varias, Z. Suo and C. F. Shih, 1991, Ductile failure of a constrained metal foil. *J. Mech. Phys. Solids*, **39**, 963–986.
bib131 R. P. Vinci and S. P. Baker (eds.), 2002, Mechanical Properties in Small Dimensions. *MRS Bull.*, **27**, 12–53.
bib132 A. A. Volinsky, N. R. Moody and W. W. Gerberich, 2002, Interfacial toughness measurements for thin films on substrates. *Acta Mater.*, **50**, 441–466.
bib133 J. S. Wang and Z. Suo, 1990, Experimental determination of interfacial toughness curves using Brazil-nut-sandwiches. *Acta Metall.*, **38**, 1279–1290.
bib134 P.-C. Wang, G. S. Cargill, I. C. Noyan and C.-K. Hu, 1998, Electromigration-induced stress in aluminum conductor lines measured by x-ray microdiffraction. *Appl. Phys. Lett.*, **72**, 1296–1298.
bib135 P.-C. Wang and R. G. Filippi, 2001, Electromigration threshold in copper interconnects. *Appl. Phys. Lett.*, **78**, 3598–3600.
bib136 W. Wang, Z. Suo and T.-H. Hao, 1996, A simulation of electromigration-induced transgranular slits. *J. Appl. Phys.*, **79**, 2394–2403.
bib137 X. Yan and R. K. Agarwal, 1998, Two test specimens for determining the interfacial fracture toughness in flip-chip assemblies. *ASME Trans. J. Electron. Packag*, **120**, 150–155.
bib138 T. Ye, Z. Suo and A. G. Evans, 1992, Thin film cracking and the roles of substrate and interface. *Int. J. Solids Struct.*, **29**, 2639–2648.
bib139 H. H. Yu, M. Y. He and J. W. Hutchinson, 2001, Edge effects in thin film delamination. *Acta Mater.*, **49**, 93–107.
bib140 J. Yue, W. Funsten and R. Tayler, 1985, Stress induced voids in aluminum interconnects during IC processing. In: "23rd Ann. Proc. IEEE Int. Reliability Phys. Symp.," pp. 126–134.
AU:27
bib141 Z. C. Xia and J. W. Hutchinson, 2000, Crack patterns in this films. *J. Mech. Phys. Solids*, **48**, 1107–1131.
bib142 Y. W. Zhang, A. F. Bower, L. Xia and C. F. Shih, 1999, Three dimensional finite element analysis of the evolution of voids and thin films by strain and electromigration induced surface diffusion. *J. Mech. Phys. Solids*, **47**, 173–199.

Comprehensive Structural Integrity
ISBN (set): 0-08 0437494
Volume 8; (ISBN: 0-080441513); pp. 1–61